Advancing microwave radar retrievals of snow depth on sea ice

Toward full characterisation of the snow and sea-ice layers

Dissertation submitted by

Arttu Jutila

in partial fulfilment of the requirements
for the degree of

Doctor of Natural Sciences (Dr. rer. nat.)

to

Faculty 1
Physics and Electrical Engineering
University of Bremen

Submission: 21 September 2021
Colloquium: 16 March 2022

Universität Bremen

ALFRED-WEGENER-INSTITUT
HELMHOLTZ-ZENTRUM FÜR POLAR- UND MEERESFORSCHUNG

1. Reviewer: Prof. Dr. Christian Haas
Alfred Wegener Institute, Helmholtz Centre for Polar and Marine Research, Bremerhaven
University of Bremen

2. Reviewer: Prof. Dr. Olaf Eisen
Alfred Wegener Institute, Helmholtz Centre for Polar and Marine Research, Bremerhaven
University of Bremen

This dissertation was written at the Sea Ice Physics section of the Alfred Wegener Institute, Helmholtz Centre for Polar and Marine Research, Bremerhaven.

"A future snow radar system with a smaller footprint may be needed to address the challenge of the air–snow interface [- -]."

— Section 7.2.2. Sea ice in MacGregor et al. (2021)

Abstract

Snow is a key factor in the sea-ice and Earth's climate systems that modifies the physical, climatic, and biogeochemical processes taking place. One of its most important impacts is in regulating sea-ice growth and melt. Despite its importance, little is known about the spatial and temporal distribution of snow depth on sea ice on the regional to global scales. Snow is tightly coupled to the highly dynamic sea-ice and atmospheric conditions and it is, therefore, very heterogeneous and constantly evolving both in space and in time. As a spatially and temporally representative, global, year-round product of snow depth observations on sea ice does not exist to this date, applications often have to rely on climatological values that do not necessarily hold true in the rapidly warming global climate. The unknown properties directly translate into the uncertainty of the result.

This dissertation takes on the ambitious goal of working toward full characterisation of the snow and sea-ice layers. To achieve that, the focus is on advancing microwave radar retrievals of snow depth on sea ice. Enhanced snow depth observations will enable improving other measurements of sea-ice related parameters, most importantly sea-ice thickness, and in joint analysis of coincident sea-ice measurements estimating sea-ice bulk density becomes possible.

In the first step, field experiments with ground-based C and K band pulse radars are carried out to investigate microwave penetration into the snow cover. The results show the K band microwaves expectedly reflect from the snow surface while the C band microwaves penetrate closer to the snow-sea-ice interface potentially enabling dual-frequency snow depth retrieval in less than half of the studied cases and only on first-year ice.

In the second step, radar measurements of snow depth on sea ice are upscaled by using an airborne radar in the western Arctic Ocean in 2017–2019. A high-sensitivity, ultrawideband, frequency-modulated continuous-wave (FMCW) radar is integrated to the instrument configuration of the Alfred Wegener Institute's (AWI) IceBird sea-ice campaigns. Snow depth retrievals with a custom algorithm based on signal peakiness from the radar measurements at a low altitude of 200 ft show good consistency against high altitude measurements at 1500 ft, which are comparable to previous acquisitions. At the nominal low altitude of the IceBird surveys, the small, two-metre radar footprint increases the spatial resolution and reduces the effect of off-nadir targets. Validation against ground measurements reveal a subcentimetre mean bias, which is below the sensor resolution. As the main result of this step, the AWI IceBird surveys are now capable of discriminating between the snow and sea-ice layers.

In the third step, the full AWI IceBird sensor configuration, including airborne laser, radar, and electromagnetic induction sounding instruments, is exploited by collocating the coincident thickness and freeboard measurements and tracking the locations of air–snow, snow–sea-ice, and sea-ice–water interfaces for more than 3000 km along survey paths over different sea-ice types. Assuming values for snow and sea-water densities and that the sea-ice cover is in isostatic equilibrium, it is possible to derive sea-ice bulk density. The results show that the ice-type averaged densities for first-year and multi-year ice are higher than and do not differ as much as widely used values from previous studies. This highlights the demand of algorithms to adapt to changing sea-ice density in satellite altimetry retrievals of sea-ice thickness. Finally, a negative-exponential parametrisation of sea-ice bulk density is derived using sea-ice freeboard as the predictor variable for future applications.

In conclusion, this dissertation takes important advancing steps in characterising the snow and sea-ice layers. Previously, the airborne AWI IceBird surveys carried out in late-winter were only able to measure the combined thickness of the snow and sea-ice layers but now, after successful integration of the FMCW radar and in combination with the airborne laser scanner measurements, it is possible to track the locations of all three interfaces bounding the snow–sea-ice system. Such airborne multi-instrument measurements of snow depth, sea-ice thickness, and freeboard are important data sets in their own right to complement the scarce observations of sea-ice related parameters in remote areas of the polar regions, but a joint analysis allows deriving further key parameters like sea-ice density. The results of this dissertation can be applied to improve retrievals of geophysical sea-ice parameters from the soon 30-year long satellite altimetry data record, which in turn will contribute to enhance monitoring the climate-sensitive sea-ice cover and modelling future projections of the changing global climate.

Tiivistelmä

Lumi on keskeinen tekijä merijää- ja maapallon ilmastojärjestelmissä, sillä se muuttaa fysikaalisia, ilmastollisia ja biogeokemiallisia prosesseja ja ennen kaikkea säätelee merijään kasvua ja sulamista. Merkityksestään huolimatta lumen määrän alueellisesta ja ajallisesta jakautumisesta merijäällä tiedetään vain vähän. Lumi on tiiviisti sidoksissa erittäin dynaamisiin merijää- ja ilmakehäolosuhteisiin, ja siksi se on hyvin heterogeeninen ja muuttuu jatkuvasti sekä paikassa että ajassa. Koska toistaiseksi ei ole olemassa alueellisesti ja ajallisesti edustavaa, maailmanlaajuista, ympärivuotista tuotetta merijään lumensyvyyshavainnoista, sovelluksissa joudutaan usein turvautumaan klimatologisiin arvoihin, jotka eivät välttämättä pidä paikkaansa nopeasti lämpenevässä globaalissa ilmastossa. Tuntemattomat ominaisuudet heijastuvat suoraan tuloksen epävarmuuteen.

Tämän väitöskirjan kunnianhimoisena tavoitteena on pyrkiä lumi- ja merijääkerrosten täydelliseen karakterisointiin. Sen saavuttamiseksi keskitytään lumen syvyyden mikroaaltotutkahavaintojen edistämiseen merijäällä. Paremmat lumensyvyyshavainnot mahdollistavat muiden merijäähän liittyvien parametrien mittausten parantamisen, tärkeimpänä merijään paksuus, ja samanaikaisten merijäämittausten yhteisanalyysissä merijään tiheyden arvioiminen tulee mahdolliseksi.

Ensimmäisessä vaiheessa tehdään kenttäkokeita maanpäällisillä C- ja K-taajuuskaistan pulssitutkilla ja tutkitaan mikroaaltojen tunkeutumista lumipeitteeseen. Tulokset osoittavat, että K-kaistan mikroaallot heijastuvat odotetusti lumen pinnasta, kun taas C-kaistan mikroaallot tunkeutuvat lähemmäs lumen ja jään rajapintaa mahdollistaen lumensyvyyden määrittämisen alle puolessa tutkituista tapauksista ja vain yksivuotisella jäällä.

Toisessa vaiheessa merijään lumensyvyyden tutkamittaukset tuodaan isompaan mittakaavaan käyttämällä lentokoneeseen asennettua tutkaa Pohjoisen jäämeren länsiosissa vuosina 2017–2019. Korkeaherkkyyksinen, ultralaajakaistainen taajuusmoduloitu kantoaaltotutka (engl. frequency-modulated continuous-wave, FMCW) integroidaan Alfred Wegener -instituutin (AWI) IceBird-merijääkampanjoiden laitekokoonpanoon. Lumensyvyyden määritys räätälöidyllä algoritmilla, joka perustuu tutkamittausten signaalihuippuihin, osoittaa hyvää johdonmukaisuutta, kun verrataan matalalla 200 jalan korkeudessa ja 1500 jalan korkeudessa tehtyjä mittauksia, joista jälkimmäiset ovat vertailukelpoisia aiempien mittausten kanssa. IceBird-tutkimusten matalalla nimelliskorkeudella tutkan valaisema pinta-ala on pieni, halkaisijaltaan kaksimetrinen, mikä parantaa spatiaalista resoluutiota ja vähentää nadiirin ulkopuolella olevien kohteiden vaikutusta. Validointi maamittauksiin verrattuna paljastaa alle senttimetrin keskimääräisen vinouman, mikä on alle sensorin resoluu-

tion. Tämän vaiheen tärkein tulos on AWI IceBird -mittausten kyky erottaa lumi- ja merijääkerrokset toisistaan.

Kolmannessa vaiheessa hyödynnetään koko AWI IceBird -mittalaitekokoonpanoa, joka sisältää laser-, tutka- ja sähkömagneettisen induktioluotausmittalaitteen. Samanaikaiset mittaukset lumi- ja merijääkerrosten paksuuksista sekä lumi- ja merijääpinnan korkeudesta vedenpinnan yläpuolella mahdollistavat ilman ja lumen, lumen ja merijään sekä merijään ja veden rajapintojen seuraamisen yhteensä yli 3000 km pitkillä tutkimuslinjoilla sisältäen eri merijäätyyppejä. Olettaen, että lumen ja meriveden tiheydet tiedetään ja että merijääpeite on isostaattisessa tasapainossa, voidaan laskea merijään tiheys. Tulokset osoittavat, että yksivuotisen ja monivuotisen jään keskimääräiset tiheydet ovat suurempia kuin aiemmissa tutkimuksissa yleisesti käytetyt arvot eivätkä poikkea toisistaan yhtä paljon. Tämä tulos korostaa, että satelliittialtimetriaan perustuvien merijään paksuutta arvioivien algoritmien tulee mukautua muuttuvaan merijään tiheyteen. Lopuksi johdetaan tulevia sovelluksia varten merijään tiheydelle negatiivis-eksponentiaalinen parametrisointi, jossa käytetään ennustemuuttujana merijään pinnan korkeutta vedenpinnan yläpuolella.

Yhteenvetona todetaan, että tässä väitöskirjassa otetaan tärkeitä edistysaskeleita lumi- ja merijääkerrosten kuvaamisessa. Aikaisemmin lopputalvisin tehdyillä AWI IceBird -lentomittauksilla pystyttiin mittaamaan vain lumen ja merijään kokonaispaksuutta, mutta nyt FMCW-tutkan onnistuneen integroinnin jälkeen ja yhdessä laserskannerin mittausten kanssa on mahdollista mitata lumi–merijää-järjestelmän kaikkien kolmen rajapinnan sijainnit. Tällaiset lumensyvyyden, merijään paksuuden sekä merijään ja lumen pinnan korkeuden samanaikaiset mittaukset useilla eri mittalaitteilla ovat jo itsessään tärkeää tietoa, jotka täydentävät merijäähän liittyvien parametrien harvoja havaintoja napa-alueiden syrjäisillä alueilla, mutta niiden yhteinen analyysi mahdollistaa myös muiden keskeisten parametrien, kuten merijään tiheyden, laskemisen. Tämän väitöskirjan tuloksia voidaan soveltaa parantamaan geofysikaalisia merijääparametreja koko pian 30-vuotisesta satelliittialtimetria-aineistosta, mikä puolestaan auttaa parantamaan ilmaston kannalta herkän merijääpeitteen seurantaa ja mallintamaan maailmanlaajuisen ilmaston muuttumista koskevia ennusteita.

Contents

Chapter 1

Introduction

This dissertation considers snow on the Arctic sea ice. While there are aspects applicable also in the southern hemisphere and to snow on land, there are also contrasting key differences, some of which are mentioned here in an exemplary manner.

This chapter gives a short introduction to snow as a key component for the sea-ice and Earth's climate systems as an overall motivation. The chapter concludes with a description of the scope and structure of this dissertation.

1.1 Role of snow on sea ice

There is ample and ever-increasing evidence that sea ice plays a crucial role in the Earth's climate system (e.g., Barber et al., 2017; Stroeve and Notz, 2018). Sea ice acts as a physical barrier and an insulator between the warm ocean and the cold atmosphere in the polar regions restricting heat, momentum, and moisture exchange. However, little is known about an integral component right in the centre of the multi-part interaction system that includes sea ice, ocean, and atmosphere — that key factor is snow. It has the best reflective and insulative properties of any natural material on Earth and as a layer on top of the sea ice it can be seen as an extra blanket that brings upon additional insulation. Moreover, snow adds a layer of complexity to the system by further modifying the physical processes taking place and regulating, among other things, sea-ice growth and melt (Webster et al., 2018).

Sea ice and snow on top of it cover large areas of the polar oceans with a distinctive annual cycle. Since the start of the satellite observations in October 1978, the record has shown that at least about 5 % of Earth's ocean surface is frozen at any given time (Stroeve and Notz, 2018). In the Arctic, the maximum areal extent of sea ice is $14–16\times10^6$ km^2 and occurs in March (Fig. 1.1, left). The minimum extent takes place in September (Fig. 1.1, right) and shows a strong negative trend in time. In the beginning of the observational period, the minimum extent was approximately 8×10^6 km^2 but more recently only $4–5\times10^6$ km^2 with a record low of 3.4×10^6 km^2 in 2012 (Parkinson and Comiso, 2013). In fact, sea-ice extent and thickness are declining in all seasons but the strongest in summer leading to some regions having experienced a total summer sea-ice loss (Stroeve and Notz, 2018). Naturally, snow on

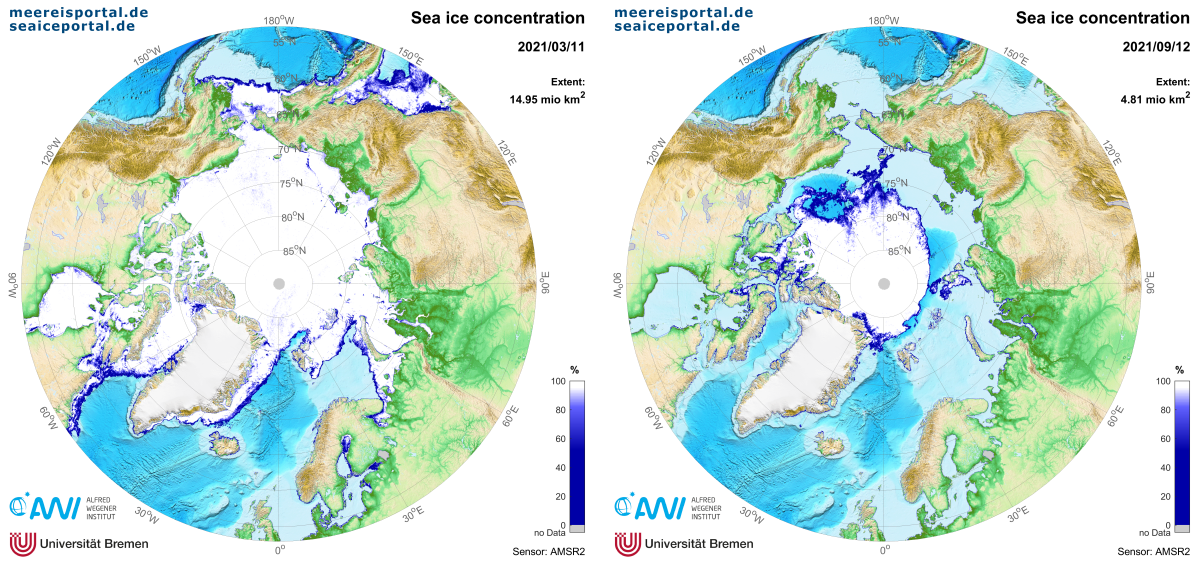

Figure 1.1. Concentration of Arctic sea ice at its recent maximum extent on 11 March 2021 (left) and minimum extent on 12 September 2021 (right). Sea-ice concentration data were obtained from https://www.meereisportal.de (Spreen et al., 2008; Grosfeld et al., 2015).

sea ice follows the annual cycle to a certain degree. In short, snowfall is intercepted by the extending sea-ice cover during the growth season and precipitation from frequent cyclones quickly accumulates a snow pack in autumn. In summer, the snow cover on the Arctic sea ice can melt completely exposing the underlying sea ice for surface melt (Webster et al., 2018).

Figure 1.2 shows a schematic of the Arctic snow–sea-ice system through its annual cycle. A snow cover starts to form on sea ice if three conditions are met. First, air temperature needs to be low enough that the falling precipitation is at least partly solid, for instance, snow, hail, or sleet. The second requirement is the precipitation itself. While majority of the snow cover is accumulated in autumn, cyclone activity and precipitation rate are reduced toward midwinter and further away from the ice edge as the moisture-providing open ocean freezes over (Sturm and Massom, 2017). In the central Arctic, far from the open ocean, precipitation rate is fairly small at less than 1 mm d^{-1} (Barrett et al., 2020). Third, a sea-ice cover must exist and it has to be thick enough to be able to carry the mass of the snow. For this simple reason multi-year ice (MYI, ice that has survived at least two full melt season) and second-year ice (SYI, ice that has survived one full melt season) usually have thicker snow cover than first-year ice (FYI, ice that has not survived a full melt season) (Sturm and Massom, 2017).

Snow loading controls the hydrostatic balance, especially in the autumn, when sea ice is still relatively thin (Fig. 1.2). The weight of the overlying snow can push the snow–ice interface below the sea level. In this case, sea-ice freeboard, defined as the height of the sea-ice surface above the water level, becomes negative. If sea ice cannot bear the overlying snow mass, surface flooding may occur (Sturm and Massom, 2017). This is common in the Antarctic where the sea-ice cover is mostly seasonal, and therefore also thinner on average, and generally covered by thick snow (Massom et al., 2001). However, in the future it may occur

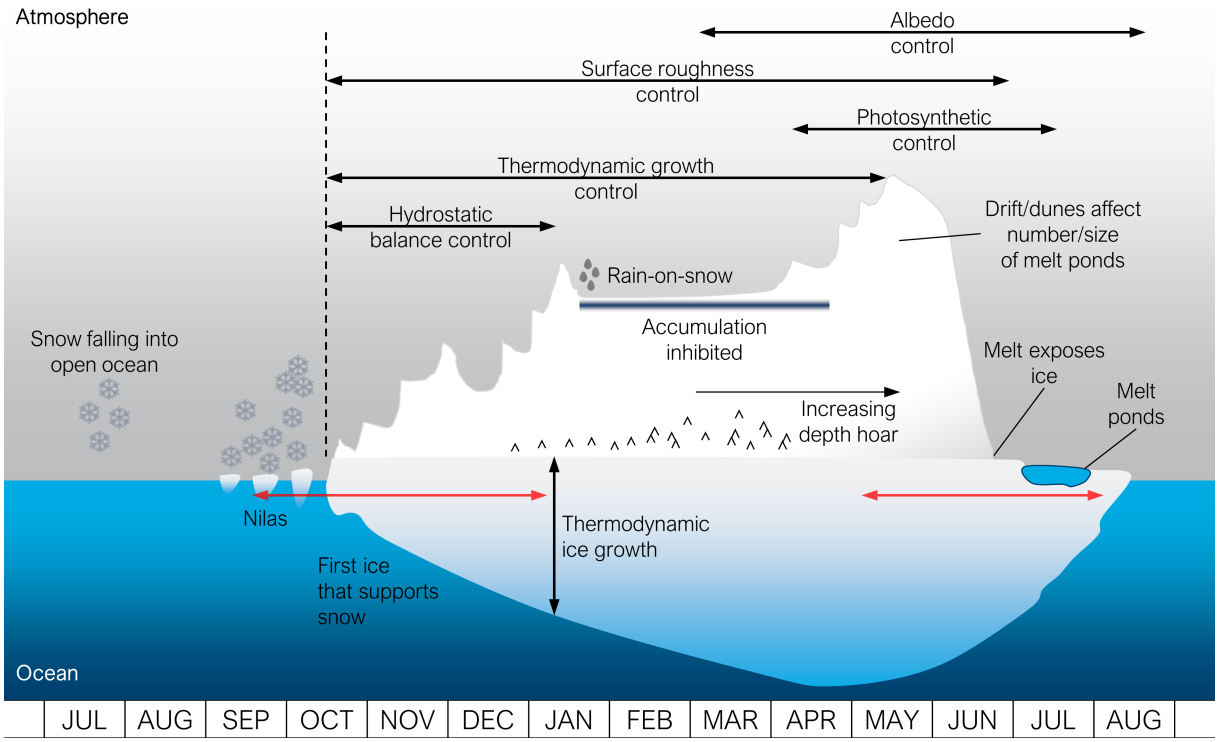

Figure 1.2. Schematic of the Arctic snow and sea-ice system evolution during its annual cycle. The red arrows indicate periods of dynamic snow–ice interaction when snow controls sea ice the most. Snow depth and sea-ice thickness are not drawn to scale. Figure is adapted from Sturm and Massom (2017).

more often also in the Arctic where sea ice is getting younger and thinner due to the warming climate, in combination with frequent precipitation events especially in the Atlantic sector (Merkouriadi et al., 2017). When snow flooded by saline sea water refreezes, it forms snow ice and contributes directly to the sea-ice mass balance.

One of the main impacts snow has on sea ice is its control over the thermodynamic sea-ice growth. Pure snow consists of solid ice, air, and liquid water when snow is wet. It is the large air content that makes snow an excellent insulator (or poor conductor), even up to 10 times better than sea ice. According to Sturm et al. (1997), the thermal conductivity of snow ranges between 0.08 and 0.4 W m^{-1} K^{-1} depending on the snow type, while for ice the value is typically 2 W m^{-1} K^{-1}. They also found that thermal conductivity is related to snow density with a second-degree polynomial function. The low thermal conductivity reduces the conductive heat flux through the sea ice and thus, snow retards thermodynamic ice growth in autumn and winter (Fig. 1.2).

Over the course of winter, the snow cover builds up from precipitation events that form layers on top of each other depicting the atmospheric conditions of that time (Fig. 1.2). New snow with a typical density of just 50 kg m^{-3} quickly starts to undergo a transformation due to wind-induced, gravitational, thermal, or melt-freeze effects called metamorphism. Strong winds, often coinciding with precipitation events, constantly erode, redistribute, deposit, and pack snow into a large range of surface features both in shape and in size. In general,

Figure 1.3. Aerial overviews of typical snow-covered sea ice in the Arctic in different seasons. (Left) Before melt, snow depth is highly variable as multitude of snow features cover the sea-ice surface. (Right) During melt, turquoise melt ponds appear between snow drifts. Photo credit: Alfred Wegener Institute / Michael Gutsche (left) and Steffen Graupner (right) (CC-BY 4.0)

snow tends to get trapped where the sea-ice surface is rough, e.g., at pressure ridges and deposited on lee sides of them (Fig. 1.3, left). This way snow smooths out the ice features and controls the surface roughness. Redistribution by wind into open leads can also cause net loss of snow. Wind and the weight of overlying layers make the snow more compact and can increase its density to up to 500 kg m^{-3} in hard wind slab layers. Even higher densities of up to about 700 kg m^{-3} are encountered in icy layers, i.e., superimposed ice, that result from freezing conditions after liquid water has been introduced to the snow pack by rain-on-snow or melting. This effectively locks snow in place and inhibits erosion while on the snow surface it can also inhibit further accumulation as snow is easily blown away from a smooth surface by wind. The thermal effects can be split into two types: temperature gradient (also known as constructive or kinetic growth) and equitemperature (destructive) metamorphism. The former takes place under strong gradients in temperature (greater than approximately 25 °C m^{-1}) and water vapour in the snow pack and produces fast-growing, faceted grains with sharp edges resulting in poorly bonded and low-density snow, whereas the latter occurs under a weak temperature gradient producing fine, rounded grains. How a snow layer and its properties, such as density and grain size, evolve in time depends on the sequence of these metamorphic processes controlled by the atmospheric conditions (Sturm and Massom, 2017; Webster et al., 2018).

While snow delays the growth of sea ice, it also slows down the melt in spring and summer (Fig. 1.2). The insulative property of snow again dampens the heat flux but this time from the warm atmosphere to the sea ice. In addition, as the solar radiation increases toward the Arctic summer, snow's ability to reflect shortwave radiation, i.e., albedo, limits the shortwave energy input by absorption. Dry snow can reflect up to 85 % of the incoming solar radiation which is significantly more compared to melting snow (about 70 %), bare sea ice (about 60 %), melt ponds (about 40 %), and open ocean (7 %) (Perovich, 2017). The remaining part is absorbed by snow and sea ice or even transmitted through to ocean warming

them up. When snow melts, it releases fresh water and creates melt ponds that form between snow drifts (Fig. 1.3, right). When the melt ponds drain, the fresh water reduces the salinity of the upper ocean and thus, affects the stratification (Sturm and Massom, 2017).

The importance of snow overlying sea ice is highlighted in a climatic mechanism called the surface albedo feedback (Wendisch et al., 2017; Webster et al., 2018). The warm air near the surface accelerates the melting of snow and sea ice exposing darker surfaces, such as bare ice, melt ponds, and eventually open ocean, that absorb more of the incoming solar radiation. That in turn results in more melt, retreating sea-ice cover, and warming of the upper ocean that increases the energy flux to the atmosphere warming the near-surface air even further. Meanwhile, snow accumulation is reduced as it falls into open ocean due to delayed sea-ice formation in autumn and consequently, the thinner snow cover melts away earlier in the spring leading to increased sea-ice melt. This is a positive feedback mechanism and its increasing effects are reflected in the rising global surface temperatures. In the Arctic region, the warming effect is amplified: the monthly zonal mean surface temperature anomalies are much stronger than in the lower latitudes and reaching up to 10 °C in the summer months (Fig. 1.4). The Arctic Monitoring and Assessment Program (AMAP, 2021) reported in their recent update that the increase in the annual mean surface temperature in the Arctic is three times higher than the global average. The year 2020 reached the highest annual mean surface air temperature anomaly for the terrestrial Arctic (> 60°N), 2.1 °C above the 1981–2010 average, since at least 1900 (Druckenmiller et al., 2021).

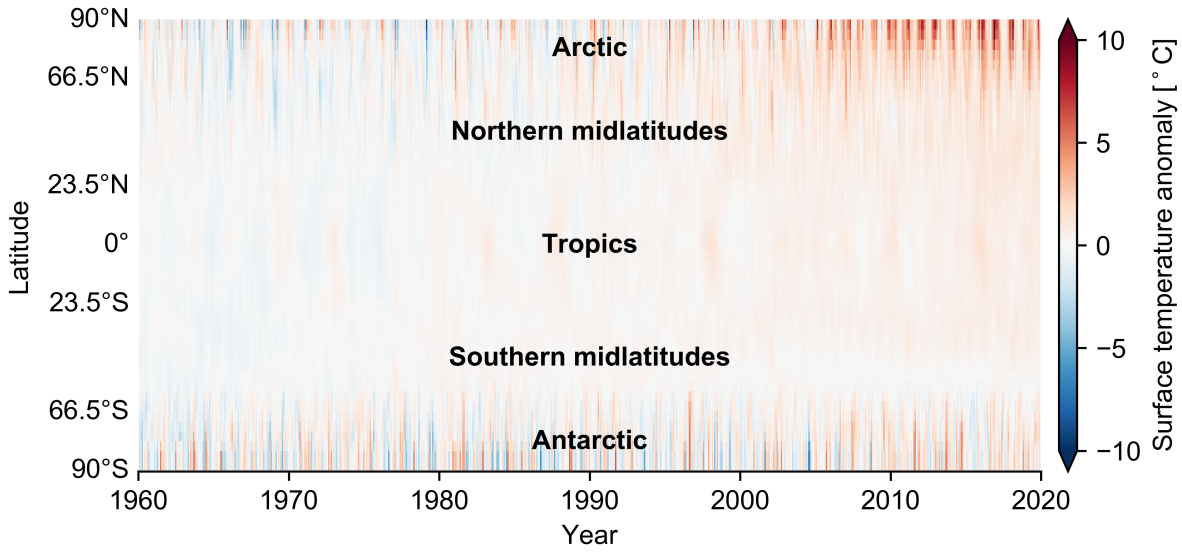

Figure 1.4. Monthly zonal mean surface temperature anomalies in 1960–2020 calculated from the climatological normal standard reference period 1961–1990 (Lenssen et al., 2019; GISTEMP Team, 2021). The positive anomalies (red colour) in the Arctic region have been increasing especially in the summer months in the last few decades. Figure is produced by adapting the code from the blog post "The Arctic Stripes" by Damien Ringeisen distributed under the GPLv3 and CC-BY 4.0 licences (Ringeisen, 2021).

Snow has also fundamental influence on ecology and biogeochemistry in the Arctic sea-ice environment. Due to its high reflectivity, snow affects the partitioning of solar radiation. It regulates the photosynthetically active radiation (PAR) transmitted into ice and underlying ocean maintaining a suitable habitat for microorganisms, such as algae (e.g,. Lange et al., 2019), while reducing the amount of harmful ultraviolet (UV) radiation (Perovich, 2006). For the most notable Arctic animals, the ringed seal and polar bear, snow offers protection to give birth and nurse their offspring (Laidre and Regehr, 2017). In direct interaction with the atmosphere, snow captures any atmospheric deposition, e.g., dust and soot, that can be transported over long distances in the atmosphere or originate from increased Arctic shipping, and lead to a decreased surface albedo (Sturm and Massom, 2017).

1.1.1 Snow depth

"Snow depth on sea ice is essentially unmeasured,
limiting mass balance estimates and ice thickness retrievals."
— Section 3.7 Key Knowledge Gaps and Uncertainties in Meredith et al. (2019)

Despite the importance of snow to the sea-ice and climate systems described in Section 1.1, we know relatively little about the spatiotemporal distribution of snow depth on sea ice on the regional to global scales. Sturm and Massom (2017) list the following contributing factors (CF):

- **CF1.** the Arctic sea-ice cover is vast and remote;
- **CF2.** snow exhibits high seasonal, interannual, and spatial variability;
- **CF3.** it is difficult to sample snow in very thick ice regions; and
- **CF4.** it remains challenging to observe snow depth on sea ice by the means of satellite remote sensing.

Snow on sea ice is tightly coupled to the highly dynamic sea-ice and atmospheric conditions and it is, therefore, very heterogeneous and constantly evolving both in space and in time (CF2). As a result and further described by Webster et al. (2018),

"there are no 'average climate properties of snow' ".

Combined to CF1, the annual maximum extent of snow-covered sea ice in the order of 10^6 km^2, conducting representative, Arctic-wide, in situ measurements of snow depth would be an enormous logistical challenge. Furthermore, the conditions in the Arctic can be extremely harsh, especially in winter, for any observer. Traversing on foot over deformed sea ice, such as pressure ridges, is challenging (CF3). Even vessels specially built for icebreaking tend to avoid such thick ice that often also trap a lot of snow that in turn increases the friction against a ship's hull (Canadian Coast Guard, 2012), leading to undersampling of thick snow in standard shipborne visual observations of sea-ice conditions (e.g., Hutchings, 2018). Measuring snow depth on newly frozen, very thin ice is not safe on foot and therefore, there

is a possibility that both ends of the in situ snow depth distribution are biased. Satellite remote sensing offers the only practical solution to observe snow depth on sea ice across ice types and all seasons on the global scale. However, remote sensing of snow remains an active field of study as there are few sufficient opportunities to map snow depth on sea ice directly (CF4). Meanwhile, it has been proposed that airborne measurements could bridge the gap between the local and global scales (e.g., King et al., 2015).

The unknown amount of snow complicates various applications. For example, snow is the largest source of uncertainty in sea-ice thickness retrieval using the freeboard-to-thickness conversion from satellite altimetry data for thinner sea ice (Giles et al., 2007). Due to the absence of contemporary information of snow mass, the thickness and density of the snow layer have to be assumed. However, snow properties, such as depth, density, salinity, and wetness, affect the radar signal and its interpretation and may lead to erroneous detection of the snow–ice interface (e.g., Ricker et al., 2015; Nandan et al., 2017). In addition, representing snow and its presence accurately in climate models, which often include snow only in a simplified manner, is crucial for the correctness of surface energy fluxes. Even a thin layer of snow on sea ice can cause a 10-fold change in the surface albedo and reflect most of the incoming solar radiation back to the atmosphere. While model performance is continuously improved, they are not able to match the current declining rate of the Arctic sea ice (Barber et al., 2017). Nevertheless, the newest model projections suggest a practically ice-free Arctic summer before the year 2050 (SIMIP Community, 2020).

The current knowledge of snow on sea ice is based mostly on in situ data collected during numerous field campaigns, most notably the Soviet North Pole drifting stations in 1954–1991. Using these data, Warren et al. (1999) compiled a snow climatology that is currently the most widely used source for snow mass information. However, the stations were located exclusively on MYI. This introduces a bias as the Arctic is undergoing a transition toward a FYI-dominated sea-ice cover driven by the global warming (Stroeve and Notz, 2018). In the past decade, the science community has put considerable effort to overcome the sampling deficiency, for example, with dedicated field campaigns, point measurements from drifting autonomous measuring platforms, such as ice mass-balance buoys (IMBs) (Richter-Menge et al., 2006; Polashenski et al., 2011; Jackson et al., 2013; Planck et al., 2019) and snow buoys (Nicolaus et al., 2021), or extensive airborne campaign programs, such as NASA's Operation IceBridge (OIB) (MacGregor et al., 2021). However, due to limited spatiotemporal coverage, the current observations still are not enough to monitor the state of snow on sea ice at the high spatial and temporal resolution, therefore introducing a key knowledge gap and uncertainty (Webster et al., 2018).

In recent years, a number of new snow depth products have emerged in attempts to overcome the mismatch between the pre-1990s climatology and the shift toward younger Arctic sea ice. Shalina and Sandven (2018) complemented the climatology in Warren et al. (1999) with data from airborne Sever expeditions covering in particular FYI in the shelf seas of the Eurasian Russian Arctic in late-winter (March–May) 1959–1986. Several modelling approaches have utilised atmospheric reanalysis data to reconstruct snow on Arctic sea ice in

varying spatial and temporal resolutions (e.g., Blanchard-Wrigglesworth et al., 2018; Petty et al., 2018; Liston et al., 2020). However, their products depend heavily on the model representation of the processes driving snow evolution and the accuracy of the precipitation reanalysis data input (Webster et al., 2018). Snow depth has been derived using brightness temperatures from passive microwave satellites (e.g., Markus and Cavalieri, 1998; Comiso et al., 2003; Maaß et al., 2013; Rostosky et al., 2018; Braakmann-Folgmann and Donlon, 2019; Kilic et al., 2019) as well as using a dual-altimetric method combining freeboard information from two satellite altimeters with differing radar frequencies (Guerreiro et al., 2016; Lawrence et al., 2018) or using a combination of laser and radar altimetry, respectively (Kwok and Markus, 2018; Kwok et al., 2020). Nevertheless, satellite retrievals of snow depth are limited by, e.g., spatiotemporal coverage, spatial resolution and differences in footprint size, surface roughness, ice type, and availability of ground measurements for validation (Webster et al., 2018). These constraints can be reduced by near real-time dual-altimetry acquisitions, such as the resonance of the CryoSat-2 and ICESat-2 satellite orbits (CRYO2ICE) since July 2020, and future single-platform dual-frequency satellite missions like the Copernicus Polar Ice and Snow Topography Altimeter (CRISTAL) mission by the European Space Agency (ESA) (Kern et al., 2020) with a launch planned in 2027.

1.2 Scope and structure of this dissertation

There is currently a lack of snow depth measurements that are representative both in space and in time across their respective scales, partly due to the highly variable nature of snow. Where, when, and how does snow accumulate on sea ice and how does the depth distribution vary are questions that still cannot be fully answered with observations in a timely manner. This hampers the retrieval of key sea-ice parameters and directly increases their uncertainties.

In this dissertation, I study methods of radar remote sensing to enhance our knowledge of snow depth on sea ice and how such a method can be established on an airborne platform on which also other sea-ice parameters are simultaneously measured with multiple instruments. A single-platform, multi-sensor configuration ensures that the measurements are done of the same sea ice, at the same time, and under the same conditions. This way the measurements are greater than the sum of its parts and allow deriving further key parameters. The ultimate goal is to characterise the snow and sea-ice layers in full.

First, in **Chapter 2**, I give the theoretical background for radar remote sensing of snow on sea ice including the basic principles of this measurement method. I also introduce the key instruments used in this dissertation, such as an altimeter and a frequency-modulated continuous-wave (FMCW) radar.

In **Chapter 3**, I investigate how microwave radar signals of two different frequencies penetrate into snow on sea ice under the hypothesis that snow depth could be derived from the difference in their respective penetration depth. The assumption, that one frequency penetrates the snow pack fully or a fixed fraction of it, returning the location of the snow–ice

interface, and the other one does not, indicating the air–snow interface, sets the basis for the dual-frequency method. It has been previously applied to satellite altimetry data, where the penetration difference between Ku and Ka band radar frequencies or Ku band and laser are used. However, the assumption and the conditions, when it is valid, in addition to the characteristics of specific retrieval algorithms are under debate. Here, I analyse results from field experiments using on-ice radars in the C and K band frequencies aided by detailed surveys of snow stratigraphy. In addition, I explore if commercial, off-the-shelf radars and software are feasible for the purpose of snow depth retrieval.

I then move on to acquiring high-resolution snow depth measurements on a larger spatial scale by using a more sophisticated type of microwave radar, the FMCW radar, in **Chapter 4**. FMCW radars have been used in snow research for more than 40 years and on airborne platforms since the 2000s (Marshall and Koh, 2008), perhaps most notably on OIB to measure snow depth over sea ice and near-surface snow layering over glaciers in 2009–2020 (MacGregor et al., 2021). Throughout the duration of the OIB mission, the FMCW radar system was continuously developed further, and a system similar to the latest one was recently commissioned by the Alfred Wegener Institute (AWI). Since 2017, an ultrawideband, quadpolarised FMCW radar system has complemented the multi-sensor instrument suite on the AWI IceBird program dedicated for airborne sea-ice surveys. Compared to OIB, the IceBird surveys are carried out at lower altitude and in slower speed that are beneficial for snow depth retrieval in higher spatial resolution and with enhanced accuracy due to significantly reduced off-nadir radar returns and smaller radar footprint size with less mixed surface types. In addition, the unique combination of airborne radar, laser, and electromagnetic induction sounding instruments on IceBird is now capable to directly measure the thickness of the sea-ice layer whereas before the snow and sea-ice layers could not be discriminated. I enhance the integration of the radar system to the IceBird program by implementing a processing chain for deriving snow depth from the radar data including a new retrieval algorithm. By comparison to previous radar acquisitions, I evaluate the performance of the radar at the low altitude and demonstrate improvements associated with a decrease in radar footprint size.

In **Chapter 5**, I take advantage of the unique AWI IceBird multi-sensor configuration by combining the derived snow depth with the coincident total (i.e., sea-ice + snow) thickness and snow freeboard measurements collected during the campaigns in 2017 and 2019. By collocating the measurements, I produce profiles of sea-ice thickness and sea-ice freeboard as well as snow depth and snow freeboard along the survey tracks. Knowing the respective locations of the air–snow, snow–ice, and ice–water interfaces allows further characterisation of the sea-ice layer, namely its density, and thus, it opens a possibility for true mass balance observations. Sea-ice density is another key sea-ice parameter of which there are no contemporary measurements and usually its values must be assumed for applications. By assuming isostatic equilibrium and the densities of snow and sea water, I derive estimates of sea-ice bulk density for the first time from such an airborne data set. Additionally, I exploit the resulting extensive data set to find a parametrisation of sea-ice bulk density for future

applications, such as upscaling the sea-ice bulk density Arctic-wide using satellite remote sensing products and enhancing satellite altimetry retrievals of sea-ice thickness.

In summary, the key research objectives for this dissertation are:

O1. Test the theory and feasibility of retrieving snow depth using dual-frequency, off-the-shelf microwave radars.

O2. Incorporate an FMCW radar into the airborne AWI IceBird sea-ice sensor suite by establishing a processing chain for retrieving snow depth, evaluate the radar performance at the low altitude, and demonstrate associated improvements over previous acquisitions.

O3. Collocate the snow depth derived from the airborne radar with other coincident airborne sea-ice measurements to track the interfaces in the snow–sea-ice system and derive estimates of sea-ice bulk density.

O4. Find a parametrisation of sea-ice bulk density for future applications.

$\Downarrow$

Goal: Full characterisation of the snow and sea-ice layers.

Finally, in **Chapter 6**, I conclude the results of this dissertation and give an outlook for possible future work.

Remark. Chapters 4 and 5 present published peer-reviewed papers and preprints currently under review that were compiled with contributions from the mentioned co-authors. Both of them are included in an unaltered form which leads to minor variations in style, language, tenses, symbols, and abbreviations throughout this dissertation. Summaries of the contributions of the respective authors are given at the beginning of each of these chapters.

Chapter 2

Radar remote sensing of snow depth on sea ice

In situ measurement efforts are often insufficient to acquire representative measurements of snow depth on sea ice, or any other geophysical parameter for that matter, over large areas and long or repeated periods of time. These monitoring requirements can be achieved by the means of remote sensing, usually with sensors on airborne or satellite platforms. Measurements from similar ground-based sensors are often used to support and validate the interpretation of data from airborne and spaceborne remote sensing instruments. In general, remote sensing methods utilise electromagnetic radiation emitted, reflected, and scattered by the Earth's surface. Particularly, three electromagnetic spectral regions are exploited in Earth observation applications: optical, thermal infrared, and microwave spectra. Microwaves are relatively unaffected by atmospheric absorption and thus, they can be used regardless of cloudiness and sunlight (Shokr and Sinha, 2015). Microwave remote sensing instruments are divided into two categories: (1) passive, i.e., radiometers, and (2) active, i.e., radars. Whereas passive microwave sensors measure the naturally emitted thermal radiation, radars transmit their own microwave signal and measure the returned signal known as *backscatter*. Especially in this dissertation, a radar is an active microwave sensor that is used for the purpose of range measurements and thus, records the backscatter as a function of time, i.e., a *waveform*. A sensor recording only the total backscattered power is called a scatterometer. By interpreting the recorded microwave signals, it is possible to infer geophysical properties of the target (Lubin and Massom, 2006).

In active remote sensing, snow depth can be derived by using altimeters. They look straight down at nadir to maximise the amount of received backscatter and measure with great precision the power distribution of the returned radar (or laser) pulse and the time delay from the transmitted signal. The time delay is then converted to range distance between the sensor and the target surface using dedicated algorithms called retrackers, corrected for changes in the propagation speed of the signal in the ionosphere and troposphere, and further converted into surface elevation (Ulaby and Long, 2014; Quartly et al., 2019). In land applications, snow depth is the difference in surface elevation between the snow-covered and

snow-free periods albeit affected by vegetation (Tedesco et al., 2015). However, such a retrieval is different over sea ice, where the elevation of the underlying sea-ice surface changes over time as a result of sea-ice drift and varying sea-ice thickness and extent. The solution is to use sensors with different signal penetration depth, e.g., two differing radar frequencies, a combination of radar and laser, or a high-sensitivity microwave radar with high range resolution. The different dielectric properties of air, snow, and sea ice cause a different amount of the incident power being backscattered from the interfaces. If the dielectric constant of snow is known, the difference in propagation time can be converted into snow depth (Yan et al., 2017a).

This chapter summarises the theoretical background for microwave radar remote sensing. Section 2.1 describes the microwave properties relevant for this measurement method and Section 2.2 introduces how to measure snow depth on sea ice using different types of radars and their basic operating principles. For a more comprehensive review of microwave remote sensing and applications related to sea ice, I refer the reader to, e.g., Lubin and Massom (2006), Ulaby and Long (2014), and Shokr and Sinha (2015).

2.1 Theory

2.1.1 Electromagnetic wave

An electromagnetic (EM) wave can be depicted as a two-dimensional transverse wave, where its electric and magnetic components oscillate perpendicular to each other and to the direction of propagation. In free space (or vacuum), the wave propagates with the speed of light ($c = 2.998 \times 10^8$ m s^{-1}) that relates its frequency (f) to wavelength (λ) through $f = \frac{c}{\lambda}$. Microwaves are typically taken to cover a wavelength range from metres down to millimetres corresponding to a frequency range of 0.3–300 GHz (Table 2.1) (Ulaby and Long, 2014).

The EM wave can be further characterised by polarisation, of which the most common type is linear polarisation. If the electric field, consisting of two orthogonal components, is orientated parallel to the plane of incidence, the wave is vertically polarised (V). If the orientation is in the perpendicular plane, the wave is horizontally polarised (H). Radars transmit pulses in certain polarisation and receive the backscattered signal in the same or perpendicular polarisation, which results in four possible combinations: co-polarised VV and HH as well as cross-polarised VH and HV. Different polarisations can interact differently with the target offering additional information about it. Other possible polarisations are elliptical and circular polarisations that result from the electric field components being out-of-phase instead of in-phase (Shokr and Sinha, 2015).

Band designation	Frequency range	Wavelength range
HF	0.003–0.03 GHz	100–10 m
VHF	0.03–0.3 GHz	10–1 m
UHF	0.3–1 GHz	1–0.3 m
L	1–2 GHz	0.3–0.15 m
S	2–4 GHz	0.15–0.075 m
C	4–8 GHz	0.075–0.038 m
X	8–12 GHz	0.038–0.025 m
Ku	12–18 GHz	0.025–0.017 m
K	18–27 GHz	0.017–0.011 m
Ka	27–40 GHz	0.011–0.0075 m
V	40–75 GHz	0.0075–0.004 m
W	75–110 GHz	0.004–0.0027 m
mm	110–300 GHz	0.0027–0.001 m
THz	300–1000 GHz	0.001–0.0003 m

Table 2.1. Standard radar bands and their respective frequency and wavelength ranges according to IEEE (2020). Other standards and definitions exist. (V/U)HF stands for (very/ultra) high frequency.

2.1.2 Radar equation

For a monostatic radar system, which uses the same antenna for transmitting and receiving, the returned power from a point target is described with the radar equation

$$P_p^r = \overbrace{\frac{P_q^t G^2 \lambda^2}{(4\pi)^3 R^4}}^{1} \underbrace{\sigma_{pq}}_{2} \tag{2.1}$$

where P is power, G is the gain of the antenna, λ is wavelength, R is the range distance between the antenna and the target, and σ is the radar cross section of the target. The superscripts r and t refer to the receive and transmit signals and the subscripts p and q to their respective polarisations. In Eq. (2.1), the first term on the right-hand side represents the radar parameters and the second term describes how the target affects the radar signal. Extending from a point target to a distributed target, the radar cross section σ_{pq} is normalised over an area A illuminated in the radar beam to derive the backscatter cross section per unit area,

$$\sigma_{pq}^0 = \frac{\sigma_{pq}}{A}, \tag{2.2}$$

also known as the backscatter coefficient, "sigma nought", or radar reflectivity. In addition, Eq. (2.1) describes how the received power varies strongly with range by a factor of $\frac{1}{R^4}$, which quickly leads to small values of P_p^r and σ_{pq}^0 on the linear scale when the range increases.

Therefore, they are often expressed in decibel units (dB) using the logarithmic scale, e.g., (Ulaby and Long, 2014; Shokr and Sinha, 2015)

$$P^r_{p\,|\,\mathrm{dB}} = 10 \times \log_{10}\left(P^r_{p\,|\,\mathrm{linear}}\right). \tag{2.3}$$

2.1.3 Backscatter

The total backscattered power from a target is a combination of two processes related to a dielectric mismatch forcing the incident EM wave to deviate from a straight trajectory: surface scattering and volume scattering. Surface scattering occurs at an interface between two media with different dielectric properties. Volume scattering originates from discrete particles within a medium that otherwise has a homogeneous dielectric background. Assuming a dry snow cover overlying sea ice, the bulk medium can be described as ice crystals in an air background bounded by the air–snow and the snow–sea-ice interfaces. Following Ulaby and Long (2014), the total backscatter from snow on sea ice in general includes contributions from (Fig. 2.1):

1. surface scattering from the air–snow interface;
2. direct backscatter from the snow volume;
3. two-way attenuated backscatter from the snow–sea-ice interface and possible internal snow layers, such as ice lenses; and
4. indirect backscatter due to multiple interactions between the snow volume and any of the bounding or internal interfaces.

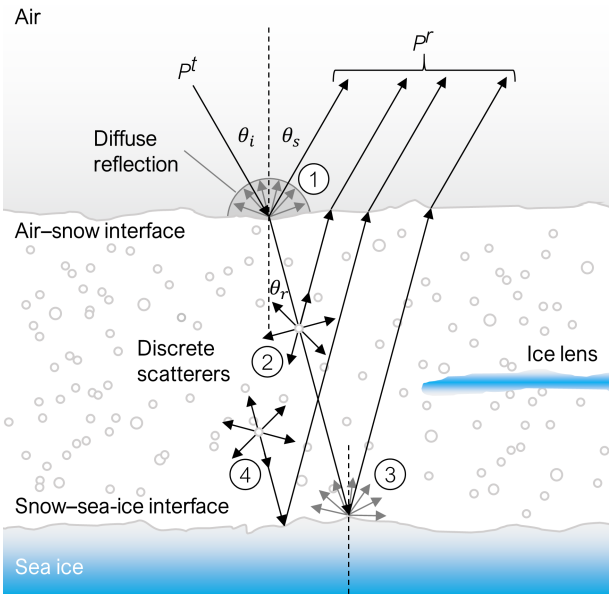

Figure 2.1. Simplified schematic on backscatter from snow on sea ice. P^t and P^r are the transmitted and received power, respectively. θ_i, θ_s, and θ_r are the angles of incidence, specular reflection, and refraction, respectively. The numbering corresponds to the list of scattering contributors in Section 2.1.3. The schematic illustrates a bistatic radar system at an oblique angle instead of a nadir-looking radar for better graphical clarity. Figure is adapted from Ulaby and Long (2014).

Onstott and Shuchman (2004) summarise that the target scattering characteristics are affected by four parameters, which in turn are dependent on the radar wavelength, polarisation, and incidence angle:

- the complex dielectric constant;
- the presence of dielectric discontinuities or discrete scatterers;
- the surface roughness; and
- the orientation of the snow and surface features relative to the radar.

Complex dielectric constant

The complex dielectric constant (ε^*), or the relative complex dielectric permittivity, describes the electrical properties of a material, therefore defining the scattering, reflection, attenuation, and EM wave propagation behaviour (Lubin and Massom, 2006). A dielectric material is non-conductive but its molecules may be displaced within molecular distances and reorient in response to an applied electric field causing dielectric polarisation[1]. It attempts to shift the positive and negative charges of the molecules in the direction of the applied electric field to induce an internal electric field. That in turn reduces the effect of the external electric field inside the dielectric material itself (Shokr and Sinha, 2015). ε^* is a complex number defined as

$$\varepsilon^* = \varepsilon_0 \left(\varepsilon' - i\varepsilon''\right) \tag{2.4}$$

where $\varepsilon_0 = 8.85 \times 10^{-12}$ F m^{-1} is the free-space dielectric constant, ε' is the relative dielectric constant or relative permittivity, $i = \sqrt{-1}$, and ε'' is the relative dielectric loss factor. The real part, ε', determines how much energy is scattered by the surface and the rest is penetrated in the material. The imaginary part ε'' describes the energy loss inside the material (Shokr and Sinha, 2015).

For a three-phase medium like snow, ε^* is a weighted dielectric mixture of air, ice, and water. When considering only dry snow and approximating air as free space ($\varepsilon'_{\text{air}} \approx 1$, $\varepsilon''_{\text{air}} \approx 0$), it is found that $\varepsilon''_{\text{ds}} \ll \varepsilon'_{\text{ds}}$ and that the relative dielectric constant is mainly a function of snow density (Lubin and Massom, 2006). Many different parametrisations exist but in this dissertation I follow Ulaby et al. (1986):

$$\varepsilon'_{\text{ds}} = \left(1 + 0.51\rho_{\text{ds}}\right)^3 \tag{2.5}$$

where ρ_{ds} is the density of dry snow in g cm^{-3} setting the values for ε'_{ds} to 1.1–2.0 for a density range of 0.05–0.5 g cm^{-3}. For comparison, pure ice has a relative permittivity of $\varepsilon'_{\text{ice}} \approx 3.15$. Other contributing factors include snow grain size and shape as well as salinity. Especially the bottommost layers of the snow pack on FYI may be saline due to brine expulsion from the underlying sea ice or incorporated highly saline frost flowers, or they may be flooded by saline sea water increasing the relative dielectric constant of snow. Additionally, introduction of liquid water quickly increases the dielectric constant, both the relative permittivity and the dielectric loss, with strong dependence on frequency, temperature, and the volume fraction of liquid water (Lubin and Massom, 2006). This has major implications for the penetration depth of the EM wave (δ_p), defined as the depth where the incident energy is reduced to e^{-1}

[1] Note that dielectric polarisation is not to be confused with EM wave polarisation introduced earlier.

(Ulaby and Long, 2014). For a low-loss medium ($\frac{\varepsilon''}{\varepsilon'} < 0.01$), such as dry snow, the penetration depth is

$$\delta_p = \frac{\lambda\sqrt{\varepsilon'}}{2\pi\varepsilon''}. \tag{2.6}$$

In microwave frequencies, dry snow is therefore near-transparent as the penetration depth can be several metres.

The relative permittivity ε' is related to the ratio between the propagation speed of the EM wave in free space and in the medium through the index of refraction (Ulaby and Long, 2014). In the case of dry snow, it results in

$$\frac{c}{c_s} = n_s = \sqrt{\varepsilon'_{\mathrm{ds}}} \tag{2.7}$$

where c_s is the propagation speed in snow and n_s in the refractive index of snow.

Surface roughness

From an electromagnetically smooth surface, the incident radiation partially undergoes a mirror-like, specular (coherent) reflection and part of it is transmitted into the medium. As the surface roughness increases, this will result in an increasingly diffuse (incoherent) reflection behaviour where the reflected energy is scattered to different directions (Fig. 2.1). Whether a surface is electromagnetically smooth is defined by Rayleigh or Fraunhofer roughness criteria relating the difference in travelled distance to a resulting phase difference of less than $\frac{\pi}{2}$ or $\frac{\pi}{8}$ radians, respectively:

$$h_{\mathrm{rms}} < \begin{cases} \dfrac{\lambda}{8\cos\theta_i} & \text{(Rayleigh criterion)} \\ \\ \dfrac{\lambda}{32\cos\theta_i} & \text{(Fraunhofer criterion)} \end{cases} \tag{2.8}$$

where h_{rms} is the standard deviation of the surface height variance, or root-mean-square (rms) height, and θ_i is the incidence angle (Ulaby and Long, 2014). In the microwave region, the wavelength is in the same order of magnitude as the rms height and thus, the stricter Fraunhofer criterion is often used. Assuming a nadir-looking radar (i.e., normal incidence), electromagnetically smooth surfaces in the microwave spectrum have an rms height of less than 3×10^{-5} – 3×10^{-2} m, which is rarely achieved by snow-covered sea ice. This can be exploited in surface type classification as calm and open water surfaces in the cracks of the sea-ice cover offer a smooth surface with a contrasting high backscatter. On a larger scale, surface roughness affects the radar footprint size. A very rough surface or tall surface features located off-nadir within the radar beam can cause earlier or multiple reflections that do not correspond to the mean height of the surface at nadir.

2.2 Observation

2.2.1 Radar altimetry

2.2.1.1 Pulse- and beam-limited radar

Nadir-looking radars look straight down and measure the time delay (τ_d), or the two-way travel time (TWTT), between the transmitted and received radar pulse (Fig. 2.2). It is converted to range distance using the propagation speed of the EM wave, which in free space is the speed of light (Ulaby and Long, 2014):

$$R = \frac{c\tau_d}{2}. \tag{2.9}$$

The range resolution (ΔR) of the radar is directly proportional to the pulse length (τ):

$$\Delta R = \frac{c\tau}{2}. \tag{2.10}$$

Therefore, a shorter pulse length results in enhanced range resolution but in turn may compromise sufficient strength of the reflected signal. In other words, achieving a centimetre-scale resolution would require a pulse length in the order of nanoseconds. However, generating a single-frequency pulse that short is difficult. To enhance the precision and range

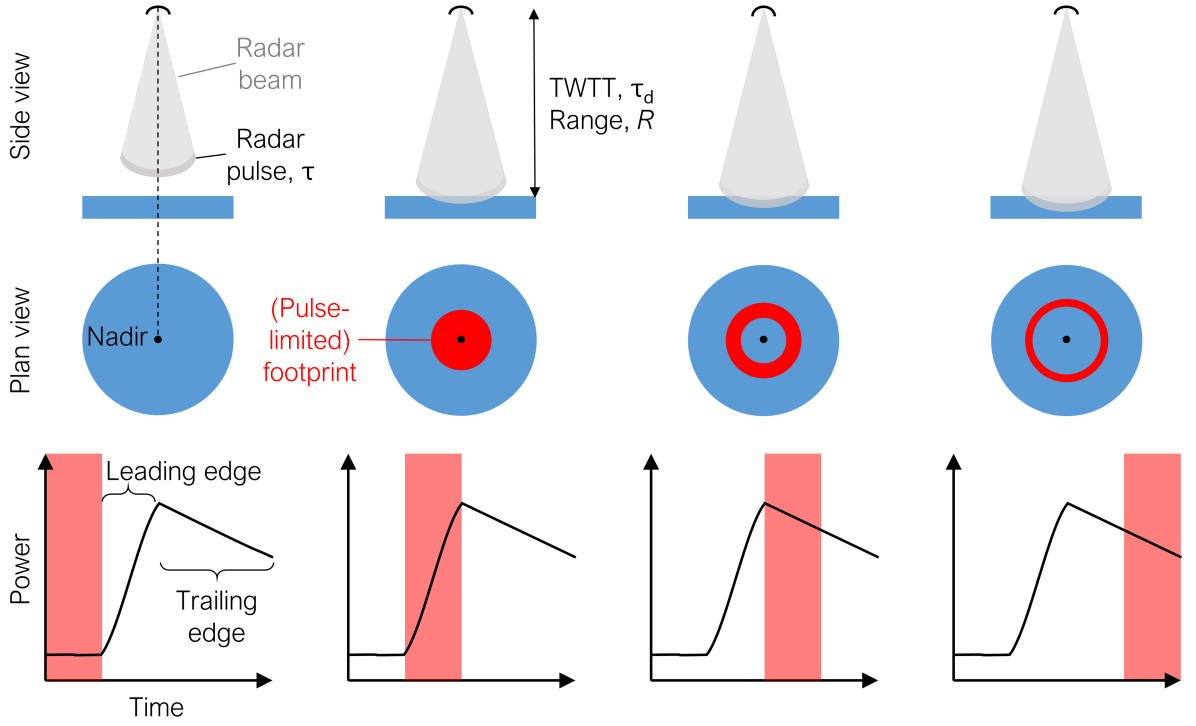

Figure 2.2. Schematic of a nadir-looking, pulse-limited radar altimeter over a flat, level surface. (Top panel) Side view of the radar signal with a pulse duration of τ. TWTT stands for the two-way travel time τ_d. (Middle panel) Time evolution of the pulse-limited radar footprint indicated in red and viewed from above. (Bottom panel) An idealised radar waveform where the red shading represents each column of the figure or step in time.

resolution of radar altimeters, a technique called pulse compression is often used. The energy of the EM pulse is spread in time and linearly over a range frequencies generating a frequency-modulated signal often referred to as a chirp. The equivalent pulse width is the inverse of the chirp bandwidth. The return chirp is passed through an inverse matched filter containing a delayed copy of the transmitted chirp, which compresses the signal back to a short pulse. This technique also decreases the required transmit power significantly, which is a highly desired feature especially in satellite applications (Ulaby and Long, 2014).

There are two main types of nadir-looking radars, i.e. altimeters, depending on the pulse length: beam-limited and pulse-limited altimeters. If the pulse completely illuminates the radar footprint in the radar beam and the full radar footprint contributes to the return signal, the radar is called beam-limited. Usually, the angular width of the radar beam is expressed using the 3-dB beamwidth of the antenna pattern that corresponds to the half-power points of the main lobe (Ulaby and Long, 2014). For a pulse-limited radar, the pulse only partially illuminates the surface resulting in a radar return from a disc-shaped to a ring-shaped footprint on a flat and level surface (Fig. 2.2).

Chapter 3 of this dissertation includes field experiments using conventional pulsed radars deployed on sea ice.

2.2.1.2 Frequency-modulated continuous-wave radar

In contrast to a pulsed radar, a continuous-wave (CW) radar transmits continuously instead of discrete pulses of microwave energy. However, a CW radar cannot measure range, because there is no basis for time discrimination due to the infinitely long pulse length. Ranging-capability can be achieved with frequency-modulation (FM), where the frequency of the transmit signal is varied in time. Such a radar is called a frequency-modulated continuous-wave (FMCW) radar (Ulaby and Long, 2014). Chapters 4 and 5 of this dissertation deal with an FMCW radar deployed on an airborne platform.

The basic ranging principle of an FMCW radar is shown in Fig. 2.3. A linear, FM signal is created by varying its frequency across the transmission bandwidth (B) from the start frequency (f_0) to the end frequency (f_1) within a modulation period (T_{pd}) and transmitted. The return signal reflected from the target is received after a time delay (τ_d) and mixed with the instantaneous transmission signal to determine the intermediate frequency difference known as the beat frequency (f_b) (Yan et al., 2017a). It can be solved using a geometrical similarity between the transmitted and received signals, highlighted in Fig. 2.3, which results in the following relationship (Ulaby and Long, 2014):

$$\frac{f_b}{f_1 - f_0} = \frac{\tau_d}{T_{pd}}. \tag{2.11}$$

Substituting $f_1 - f_0 = B$ and τ_d with Eq. (2.9) yields

$$f_b = \tau_d \frac{f_1 - f_0}{T_{pd}} = \frac{2R}{c} \frac{B}{T_{pd}}, \tag{2.12}$$

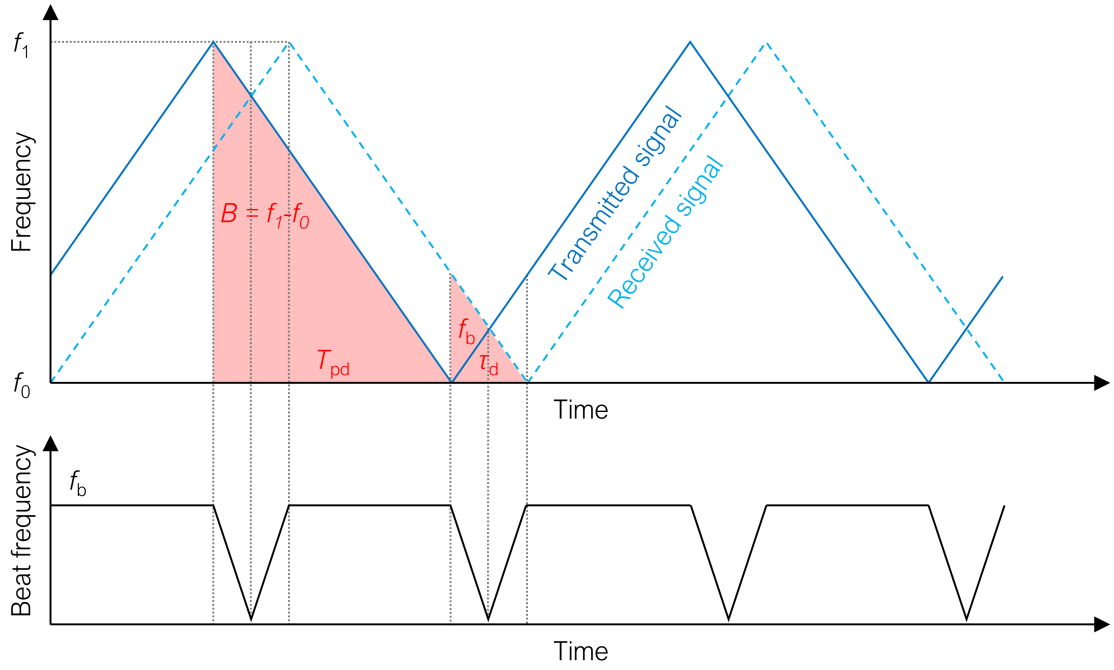

Figure 2.3. A frequency time plot illustrating the basic ranging principle of an FMCW radar. In the upper panel, a linear frequency-modulated signal is transmitted (solid dark blue line) sweeping across the transmission bandwidth, $B = f_1 - f_0$, during a modulation period of T_{pd}. The signal reflected from the target is received (dashed light blue line) after a time delay of τ_d. The lower panel shows the mixed transmitted and received signals to solve the respective frequency difference known as the beat frequency, f_b. The transparent red triangles highlight the relationship between T_{pd}, τ_d, B, and f_b. Figure is adapted from Yan et al. (2017a).

i.e., the beat frequency is directly proportional to range. Therefore, rearranging for range gives

$$R = \frac{c f_b T_{pd}}{2B}. \tag{2.13}$$

The range resolution of an FMCW radar is determined by the effective frequency resolution $\Delta f_b = \frac{1}{T_{pd}}$ and thus, its bandwidth (Ulaby and Long, 2014):

$$\Delta R = \frac{c \Delta f_b T_{pd}}{2B} = \frac{c T_{pd}}{2B} \frac{1}{T_{pd}} = \frac{c}{2B}. \tag{2.14}$$

Therefore, increasing the bandwidth of the radar will improve the range resolution. Sub-decimetre-scale range resolution is necessary to resolve snow depth on sea ice, and it can be achieved with a bandwidth of greater than 1.5 GHz. This value is also one of the bandwidth-based definitions for an ultrawideband radar (IEEE, 2007). Other definitions exist.

FMCW radars have been used in snow research for more than 40 years to study not only snow depth but also snow water equivalent (SWE), snow density, and wetness among other topics. In many cases, FMCW radar studies have been focused on validating retrievals of snow parameters from satellite radars (Marshall and Koh, 2008). Since the 2000s, FMCW radars have been deployed on airborne platforms, perhaps most notably on OIB to measure snow depth over sea ice and near-surface snow layering over glaciers in 2009–2020 (Yan et al.,

2017a; MacGregor et al., 2021). During that time, the radar system improved constantly, most importantly increasing its bandwidth from 4–6 to 2–18 GHz. Several different algorithms have been developed and used to retrieve snow depth on both Arctic and Antarctic sea ice from FMCW radar data (e.g., Kurtz and Farrell, 2011; Kwok et al., 2011; Kurtz et al., 2013, 2014; Kwok and Maksym, 2014; Newman et al., 2014; Koenig et al., 2016; Kwok et al., 2017; Jutila et al., 2021b).

2.2.1.3 Synthetic aperture radar

Further enhancement can be achieved by decreasing the radar footprint size through synthetic aperture radar (SAR) processing. This method is called delay/Doppler radar altimetry and takes advantage of the along-track motion of the radar on an aircraft or satellite platform (Raney, 1998; Ulaby and Long, 2014). A ground target is illuminated in the footprints of consecutive radar pulses and due to the along-track motion of the radar, the returning signals from the target are delayed and experience a Doppler shift in frequency[1] (Fig. 2.4, left). In other words, a radar footprint can be divided into cross-track sections called Doppler beams according to the frequency shift. After delay compensation, the Doppler frequency information can be used to integrate returns from a collection (burst) of consecutive pulses that originate from the same target. While the cross-track radar footprint size is unaffected, this method effectively decreases the along-track footprint by an order of magnitude and increases the signal-to-noise ratio. SAR altimetry has been successfully established on both airborne (e.g., Helm, 2008; Yan et al., 2017a) and spaceborne platforms, where in the latter it is currently operational on the CryoSat-2 (Wingham et al., 2006) and Sentinel-3 (Donlon et al., 2012) satellite missions.

Recently, Egido and Smith (2017) introduced a more advanced method called fully focused SAR (FFSAR) where the integration time is extended to cover multiple bursts of coherent pulses and as long as the ground target is illuminated by the radar (Fig. 2.4, right).

[1] Analogous to the siren of an emergency vehicle passing an observer.

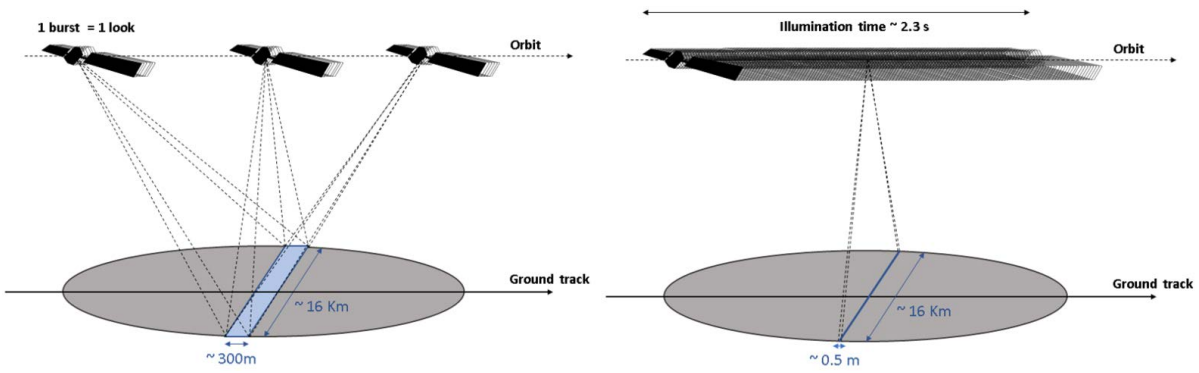

Figure 2.4. (Left) Unfocused synthetic aperture radar altimetry. (Right) Fully focused synthetic aperture radar altimetry. Figure credit: Collecte Localisation Satellites (CLS). Source: https://www.aviso.altimetry.fr/en/techniques/altimetry/principle/delay-doppler-/-sar-altimetry.html

Hardware-permitted, this technique leads to even greater along-track resolution increase than in unfocused SAR processing described above, up to the theoretical maximum of half the antenna length (sub-metre scale). The Poseidon-4 SAR altimeter on the current Sentinel-6/Jason-CS satellite mission is suitable for FFSAR processing (Scharroo et al., 2016; Donlon et al., 2021).

2.2.1.4 From waveform to range

The shape and the magnitude of the transmitted radar pulse change as it interacts with the target. The distribution of the backscattered power in time is called a *waveform*. The bottom panel of Fig. 2.2 shows an idealised and simplified example, where the maximum return power corresponds to the largest illuminated footprint area around the nadir point and marks the end of the leading edge of the waveform. As the pulse propagates outward on the surface, the illuminated area of the footprint decreases and so does the backscattered power. This trailing edge of the waveform is affected by reflections from off-nadir targets and volume scattering from within the target medium. As a first approximation and in the simplest of terms, the range distance can be determined assuming that the maximum backscattered power corresponds to the location of the main scattering horizon and the largest dielectric discontinuity. In general, the dielectric discontinuity at the snow–sea-ice interface is larger than at the air–snow interface resulting in a stronger return signal from the sea-ice surface than from the snow surface.

Waveforms from natural targets can be much more complex in reality. For example, a specular reflection from open water in a sea-ice lead results in a single distinctive local maximum (peak) with a short leading edge in the waveform (Fig. 2.5a), whereas the return signal from snow-covered sea ice can include multiple peaks from the different interfaces depending on the wavelength and sensitivity of the radar (Fig. 2.5b). Moreover, increasing surface roughness decreases the amount of EM energy returned to the radar as it is scattered to different directions, contributes to the width of the leading edge, and adds noise in the signal that can obscure the reflections from the interfaces (Fig. 2.5c).

The raw range estimate given by the altimeter is only approximate, because the radar continuously tracks the surface to apply a range window to be able to mix the received signal with the copy of the transmitted one. The exact location of the mean scattering surface, a point on the leading edge of the waveform, must be defined using retrackers. These are physical and empirical models fitted to the waveform data, with dedicated retrackers used for different waveforms which are classified based on surface types inferred from waveform power and shape characteristics (e.g., Fig. 2.5). One of the most commonly used retrackers is called the threshold first-maximum retracker algorithm (TFMRA) that empirically defines the tracking point on the leading edge of the waveform using a simple percentage power threshold (Quartly et al., 2019).

Due to the spaceborne orbit of the satellite altimeters, various geophysical corrections must be considered for accurate determination of the range distance to the sea-ice and snow surface. These include, e.g., the ionospheric and tropospheric corrections, which take

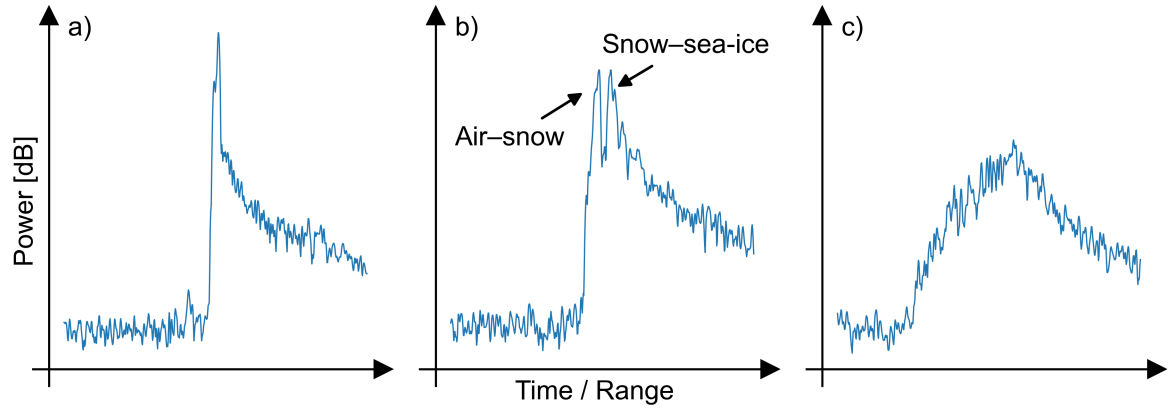

Figure 2.5. Example waveforms from different surfaces in the sea-ice environment. a) Strong single-peak echo from open water in a sea-ice lead. b) Return signal from snow-covered sea ice with two peaks corresponding to the air–snow and snow–sea-ice interfaces. c) Very rough surfaces, such as pressure ridges, cause an ambiguous return signal where interfaces cannot be determined. These waveforms were captured by the airborne 2–18 GHz FMCW radar used in this thesis (Fig. 4.5c).

into account the varying EM wave propagation speed in the atmosphere, and various topographic factors due to dynamic sea-surface height affected by tides, ocean currents, and atmospheric pressure (Quartly et al., 2019). For range and range resolution in a medium other than free space, the speed of light in Eqs. (2.9) and (2.10) is replaced with a corresponding propagation speed, for example the propagation speed in dry snow from Eq. (2.7). Knowing the orbit of the satellite precisely, surface elevations based on a reference ellipsoid can be converted to freeboard values, i.e., height above the local sea level, by subtracting the instantaneous sea-surface height of lead measurements. The difference in snow and sea-ice freeboards, i.e., the distance between the snow and sea-ice surfaces, results in snow depth.

2.2.2 Satellite altimetry applications

For global-scale observations of snow depth on sea ice, using satellites is the only practical option to get reasonable and sufficient coverage both in space and in time. Satellite radar altimeters apply the same basic methodology as the previously described nadir-looking radars by transmitting pulses of EM energy towards the surface and measuring the TWTT and the power of the backscattered signal. However, international frequency allocations allow satellite radar altimeters a transmit bandwidth of only some hundreds of megahertz (Ulaby and Long, 2014). Therefore, ultrawideband FMCW technology cannot be directly applied in satellite altimetry but instead pulse compression is used.

Satellite radar altimeters are not sensitive enough to distinguish both snow and sea-ice surfaces at once and thus, a combination of satellite altimeters must be used to derive snow depth: one that penetrates the snow cover and one that does not (Fig. 2.6). Based on laboratory experiments by Beaven et al. (1995), a 13.4 GHz radar signal penetrates the snow and the ice surface dominates the backscatter. It is therefore assumed that the main scatter-

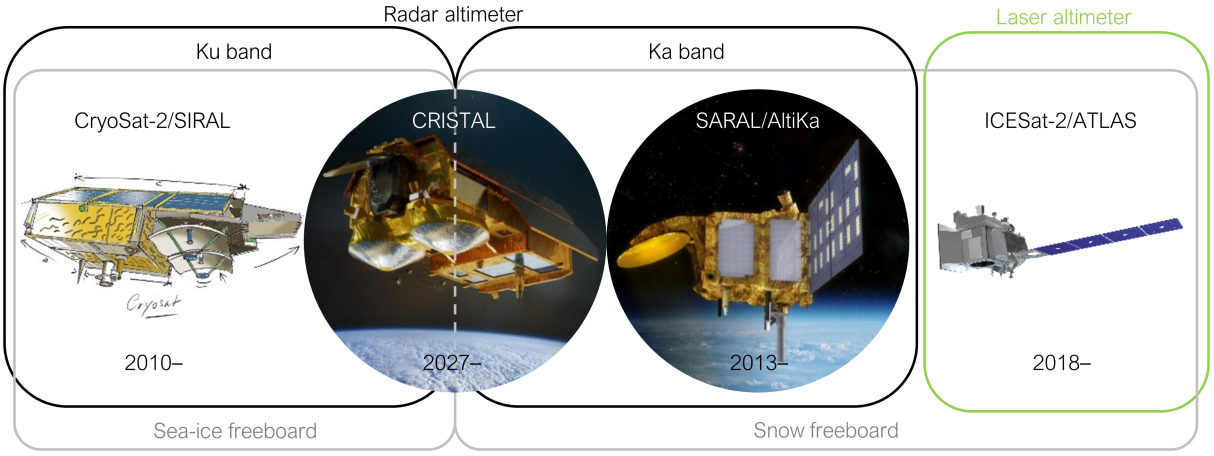

Figure 2.6. Schematic illustrating some of the current and future satellite altimetry missions used for dual-frequency retrieval of snow depth on sea ice. Ku band radar altimeters are used to derive sea-ice freeboard, whereas laser and Ka band radar altimeters measure the snow freeboard. Difference in these freeboard values yields snow depth. Illustration credits: ESA-C. Vijoux for CryoSat-2; Airbus for CRISTAL; CNES/O. Sattler for SARAL; NASA for ICESat-2.

ing horizon for Ku band satellite altimeters, such as the 13.6 GHz SAR Interferometric Radar Altimeter (SIRAL) onboard the ESA CryoSat-2 satellite (Wingham et al., 2006), is located at the snow–ice interface. In contrast, the Ka band microwaves, such as from the 35.75 GHz nadir altimeter in Ka band (AltiKa) onboard the French/Indian Satellite for ARgos and AltiKa (SARAL), are more sensitive to surface scattering decreasing the penetration depth and shifting the main scattering horizon to the snow surface (e.g., Guerreiro et al., 2016). Snow freeboard can be retrieved also with a satellite laser altimeter, such as the Advanced Topographic Laser Altimeter System (ATLAS) onboard the NASA ICESat-2 satellite (Markus et al., 2017), since a laser beam does not penetrate snow.

While the previously mentioned assumptions of Ku and Ka band radar penetration depths corresponding to the snow–sea-ice and air–snow interfaces, respectively, are generally well acknowledged and widely used, there are also studies that put the assumptions under debate. Willatt et al. (2010, 2011) investigated the Ku band penetration into snow using an on-ice radar in the Antarctic and an airborne radar in the Arctic and found that the snow–ice interface was not the dominant scatterer for all cases but only for cold and dry snow lacking any morphological features. Moreover, Nandan et al. (2017) proposed a vertical shift of the main scattering horizon due to the altered dielectric properties of saline snow on FYI. Armitage and Ridout (2015) compared the Ka band AltiKa data against airborne laser and radar altimeter data and found that the main scattering occurred at approximately 50 % depth in the snow cover.

Snow depth retrievals using satellite altimetry are restricted in time and space. As the radar signal does not penetrate wet snow, sea-ice freeboard can be determined only in winter, i.e., between October and April in the Arctic, when the snow can be expected to be cold and dry. Furthermore, in summer, melt ponds complicate the retrieval of local sea-surface height needed for the freeboard conversion as their water level differs from the surround-

ing leads and they are also effective sources of backscatter in contrast to the surrounding wet sea-ice surface (Quartly et al., 2019). More constrictions arise from the satellite orbit factors. The inclination of the satellites that allow them to cover area only up to a certain latitude: 81.5° N/S (e.g., ERS-1/2, Envisat, SARAL, Sentinel-3A/B), 86° N/S (e.g., ICESat), or 88° N/S (e.g., CryoSat-2, ICESat-2). Differing orbits also mean that the satellites do not measure the same sea ice at the same time. In addition, specifications of the different sensors cause differences in altimeter footprint size ranging from less than 100 m of the laser altimeters up to several kilometres of the older radar altimeters leading to potential intermission biases due to surface roughness. Despite the challenges of the dual-altimetry approach, several attempts have been made to derive snow depth on the Arctic sea ice (Guerreiro et al., 2016; Lawrence et al., 2018; Kwok et al., 2020). Improvements are expected due to the orbit resonance and near real-time acquisitions of the CryoSat-2 and ICESat-2 satellites (since July 2020, CRYO2ICE) and the future single-platform dual-frequency radar altimetry mission CRISTAL (Kern et al., 2020).

Besides using freeboard information from satellite altimeters, snow depth on sea ice has been derived using brightness temperatures from multifrequency passive microwave sensors (e.g., Markus and Cavalieri, 1998; Comiso et al., 2003; Maaß et al., 2013; Rostosky et al., 2018; Braakmann-Folgmann and Donlon, 2019; Kilic et al., 2019). While satellite radiometers offer up to daily coverage, snow depth products utilising them are mainly limited to only FYI and a snow cover of less than 0.5 m in thickness as well as suffer from underestimation over rough surfaces (Webster et al., 2018).

Chapter 3

C and K band microwave penetration into snow using off-the-shelf radars

Abstract. Snow cover on sea ice poses a challenge for radar measurements as microwave penetration into snow is not yet fully understood. In this chapter, the aim is to investigate microwave penetration into snow on Arctic sea ice using commercial C (6 GHz) and K (26 GHz) band radars. Radar measurements collected at nine study locations over first-year and multi-year landfast sea ice in the Lincoln Sea in May 2018 are analysed together with detailed measurements of the physical properties of the snow cover to determine the dominant scattering horizons at both frequencies and evaluated for the feasibility to determine snow depth. The results show that in 39 % of the measurements and only on first-year ice major fraction of the C band radar backscatter originated closer to the snow–ice interface potentially enabling snow depth retrieval. At K band, 81 % of the radar returns originated from the snow surface. However, the analysis was potentially hampered by relatively warm air temperatures (up to −0.9 °C) during the study period and morphological features found in the snow cover, partly confirming the findings of previous studies.

3.1 Introduction

Our knowledge of microwave penetration into snow on sea ice is inconsistent. In theory, penetration depth of microwaves is inversely (directly) proportional to frequency (wavelength) as introduced previously in Section 2.1.3 and Eq. (2.6). In addition, microwave penetration into snow is affected by the interplay between scattering and absorption, which in turn depend on the physical properties of snow, such as density, grain size and shape, salinity, and wetness. Of particular interest has been the Ku band frequency (~13.6 GHz) that is used by many past, present, and proposed satellite radar altimeter missions, such as ERS-1/2, Envisat, CryoSat-2, Sentinel-3A/B, and CRISTAL (Quartly et al., 2019). Using their data for the freeboard-to-thickness conversion in sea-ice thickness measurements relies on the assumption that the Ku band radar return penetrates the snow cover and originates from the sea-ice surface. It has been shown in a laboratory that for a cold, dry, homogeneous, 21 cm thick snow cover the snow–ice interface return indeed dominated and the snow volume scatter contribution was negligible at Ku band (Beaven et al., 1995). However, both field

observations and modelling studies suggest that the assumption may be invalid outside laboratory conditions (e.g., Willatt et al., 2010, 2011; Nandan et al., 2017, 2020).

Observations from ground-based radar systems are required to understand not only how different snow and sea-ice types affect the backscattered radar signal and from where the dominant scattering originates but also to interpret the measurements from other radar platforms correctly. Due to their larger footprint size, radar observations from aircraft and satellites can often include contributions from a mixture of surface types whereas a ground-based system can target a single homogeneous surface and assist in decomposing the backscatter signal (Stroeve et al., 2020).

There is an abundance of studies focusing on microwave penetration into snow using ground-based frequency-modulated continuous-wave (FMCW) radars (e.g., Marshall and Koh, 2008, and references therein). They focus mostly on frequencies at or smaller than the Ku band and on terrestrial snow while similar studies using higher frequencies, such as the K or Ka band, or focusing on snow on sea ice are scarce. One example including higher frequencies is the study by Koh et al. (1996), where multiband FMCW radars at C (3.9–5.9 GHz), X (8.2–12.4 GHz), and Ka (26.5–40 GHz) bands were used to characterise the snow cover in terrestrial test sites in the Northeastern United States. It was demonstrated that the higher frequencies were more sensitive to the snow microstructure revealing subtle changes between layers while sometimes unable to detect the ground reflection. The lower frequencies were more suitable for studying deeper and wetter snow packs.

Previous ground-based radar studies about microwave backscatter and extinction mechanisms and determining snow thickness on sea ice have concentrated on the Antarctic, where the snow cover is generally deeper and more complex compared to the Arctic due to warmer winter temperatures and frequent flooding. Kanagaratnam et al. (2007) studied snow on the Antarctic sea ice with an S/C band (2–8 GHz) FMCW radar finding the air–snow and snow–ice interfaces dominating the radar echoes and a high correlation between in situ and radar-derived snow depths. Willatt et al. (2010) extended the bandwidth to higher frequencies by using a C/X/Ku band (4.5–16 Ghz) FMCW radar to study radar response from different snow types also in the Antarctic. They found that the assumption of the snow–ice interface returns dominating at Ku band was valid for the surveyed sea ice in the Antarctic only when morphological features and flooding were absent. Using an airborne radar altimeter in the Arctic, Willatt et al. (2011) showed that Ku band microwaves did not penetrate as deep but were reflected closer to the air–snow interface when the snow temperature was relatively warm, i.e., close to freezing (up to -4 °C). More recently, Stroeve et al. (2020) developed a new dual-frequency, Ku (12–18 GHz) and Ka (30–40 GHz) band, FMCW radar with fully polarimetric capability. The radar was deployed on the Arctic sea ice during the year-long Multidisciplinary drifting Observatory for the Study of Arctic Climate (MOSAiC) drift expedition in 2019–2020 to study the dominant scattering horizon and also backscatter relevant to satellite radars in different snow packs. The data are currently being processed together with a vast amount of year-round observations of snow depth and other relevant physical properties of the snow cover.

The studies mentioned above and many others alike have been conducted with purpose-built FMCW radars. Using FMCW technology combined with a wide bandwidth rather than conventional pulsed radars is beneficial for acquiring better range resolution, but it may bring unwanted complexity to the radar system and increased development costs. In recent years, using commercial radars has become increasingly popular for their ease of use and relatively low cost. Ground-penetrating radar (GPR) is a well-established method in studying glaciers (Navarro and Eisen, 2009) and the seasonal snow cover especially in the Nordic countries (Lundberg et al., 2010). Pfaffhuber et al. (2017) pulled off-the-shelf, 400 MHz and 800 MHz GPRs in a sledge over the Antarctic sea ice and argued that GPRs are efficient in snow thickness surveys and "thus, making purpose-developed, complicated step frequency/frequency-modulated radars is not strictly necessary for the task". The usage of commercial FMCW radars in snow research is still in its infancy as technology continues to become more affordably available, but recently Pomerleau et al. (2020) demonstrated the use of an off-the-shelf, 24 GHz FMCW radar in measuring lake ice thickness and monitoring snow water equivalent (SWE) and snow density (snow depth was determined by other means).

This chapter investigates the penetration of C (6 GHz) and K (26 GHz) band microwaves into snow on sea ice using field experiments with commercial pulsed radars aided by detailed surveys of snow stratigraphy. The measurements were conducted over landfast first-year and multi-year sea ice in the Arctic in May 2018. The objectives are the following: (1) to determine the locations of the dominant scattering surfaces for each of the two frequencies and relate them to the structure and physical properties of the snow cover, (2) to assess a hypothesis that snow depth could be derived from their respective difference, and (3) to explore if off-the-shelf, conventional pulsed radars and their software are feasible for the purpose of snow depth retrieval.

3.2 Data and methods

3.2.1 Study site and general conditions

The field campaign of the 2018 Multidisciplinary Arctic Program — Last Ice took place on landfast sea ice in the Lincoln Sea approximately 6 km off the coast of Ellesmere Island near Canadian Forces Station (CFS) Alert in May 2018 (Fig. 3.1a–c). The study site was chosen so that both first-year ice (FYI) and multi-year ice (MYI) were easily accessible (Lange et al., 2019). The respective sea-ice thicknesses measured using a ground-based electromagnetic (EM) induction sounding instrument (Geonics EM31SH; method described in Haas et al., 2017) along a 240 m long transect crossing both ice types on 24 May were on average 1.4 ± 0.2 m and 2.9 ± 0.7 m. Snow thickness was measured along the same transect using an automatic snow depth probe (Snow-Hydro LLC magnaprobe; Sturm and Holmgren, 2018) on 9–10 and 24 May resulting in average values ranging between 0.22 ± 0.14 m and 0.30 ± 0.12 m for FYI and between 0.42 ± 0.24 m and 0.47 ± 0.23 m for MYI, respectively (Lange et al., 2019).

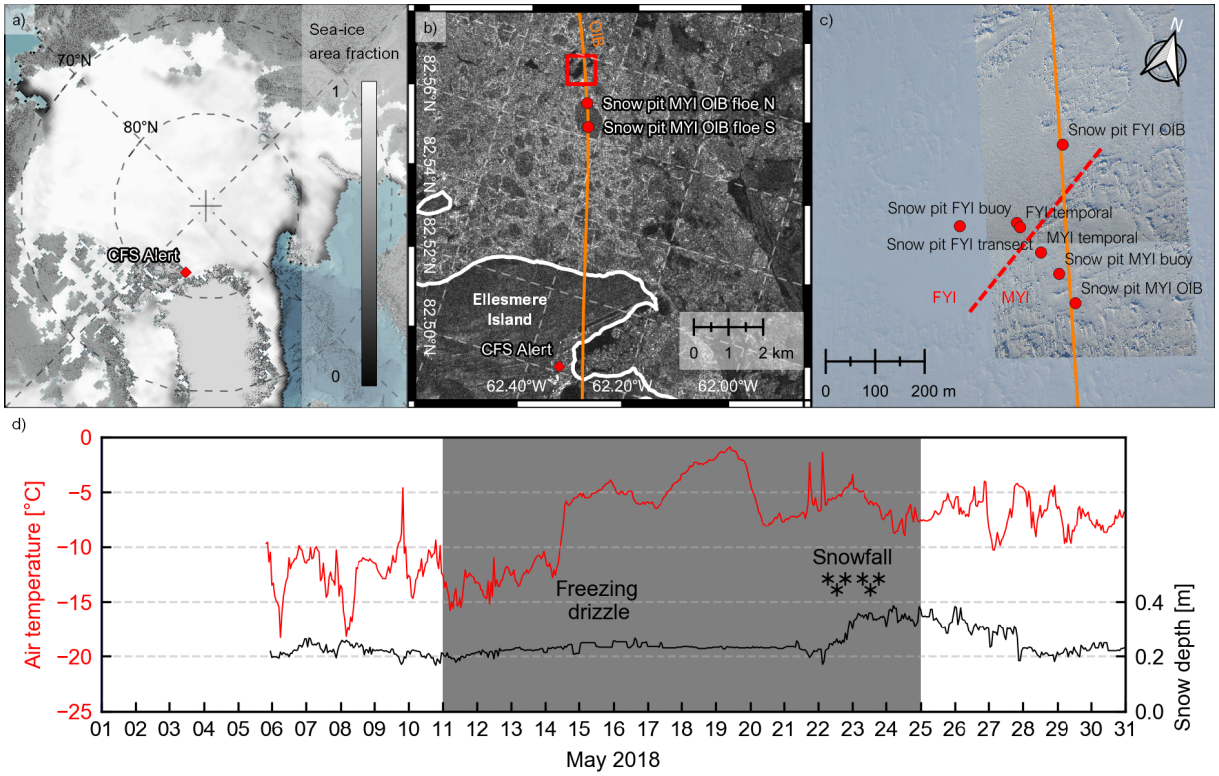

Figure 3.1. a) The study site in Alert in the Arctic-wide context together with the average sea-ice area fraction in May 2018 (Meier et al., 2021). b) The main ice camp (red square, the extent of panel c)) in relation to Ellesmere Island and the Canadian Forces Station (CFS) Alert (red diamond) on a Sentinel-1 level-1 interferometric wide swath (IW) ground range detected (GRD) dual-polarised (HH+HV) SAR image acquired in the beginning of the field campaign on 5 May 2018 as well as two snow study locations (red dots) on a big MYI floe. The orange line is the NASA Operation IceBridge (OIB) flight track on 16 April 2018 (NASA, 2018). Brighter colours of the SAR image indicate higher backscatter, i.e., rougher (older) sea ice, and darker colours lower backscatter, i.e., smoother (younger) sea ice. Copernicus Sentinel data 2018. c) The detailed snow study locations close to the main ice camp on OIB Digital Mapping System (DMS) optical imagery from 4 April and 16 April 2018 (Dominguez, 2010, updated 2018). The red dashed line shows the approximate border between FYI and MYI. d) Hourly air temperature (red, left-hand side) and snow depth (black, right-hand side) in May 2018 measured by Snow Buoy 2018S65 (Grosfeld et al., 2015; Katlein and Nicolaus, 2019; Nicolaus et al., 2021) deployed close to the snow pit MYI buoy in panel c). Grey background indicates the period of detailed snow studies. Moreover, major weather events, such as freezing drizzle observed on 15 May and snowfall on 22–23 May, are marked.

During the field measurements, the mean air temperature was -9 ± 4 °C and the following major weather events were observed: wind-driven snow distribution event on 9–10 May, freezing drizzle on 15 May, and snowfall without significant redistribution by wind on 22–23 May (Fig. 3.1d). Moreover, aircraft surveys by NASA Operation IceBridge (OIB) were carried out over the study site prior to the field campaign on 4 and 16 April 2018 (Studinger et al., 2011; NASA, 2018).

3.2.2 Detailed snow studies

The detailed snow studies took place between 11 and 24 May as summarised in Table 3.1. A total of nine locations were studied, divided roughly equally between FYI and MYI, including

Table 3.1. Summary of the detailed snow studies including instruments and parameters. h_s is snow depth, SMP is the SnowMicroPen instrument, T_s is snow temperature, ρ_s is snow density, SSA is specific surface area using the IceCube instrument, F is snow grain shape/form, E is snow grain size, R is snow hardness, and S is salinity. Symbols follow Fierz et al. (2009). The last column indexes the figures summarising the measurement results.

Date	Name	h_s [cm]	Radar	SMP	T_s	ρ_s	SSA	F, E, R	S	Fig.
12 May 2018	FYI buoy	18	x	x[c,d]	x	x	x	x	x	A.1
14 May 2018	MYI buoy	42	x	x[d]	x	x	x	x	x	3.4
16 May 2018	FYI OIB	12	x	x[d]	x	x	x	x	x	A.2
18 May 2018	MYI OIB	43	x	x[e]	x	x	x	x	x	A.3
21 May 2018	MYI OIB floe N	36	x	x	x	x	x	x	x	A.4
21 May 2018	MYI OIB floe S	68	x	x	x	x	x	x		A.5
22 May 2018	FYI transect	20	x	x	x	x	x	x	x	3.3
24 May 2018	FYI temporal	40	x[a]	x				x		3.5
24 May 2018	MYI temporal	28	x[b]	x				x		A.6

[a] Only radar and h_s also on 11, 13, 15, 17, 19, and 22 May 2018
[b] Only radar and h_s also on 17, 19, and 22 May 2018
[c] One day later
[d] Coarse (20-25 cm) lateral resolution
[e] Data saving failure

two locations with repeated visits to create a short time series of the radar response. The measurement procedure was the following and is explained in more detail below:

1. Radar measurements
2. High-resolution snow penetrometer measurements
3. Snow pit measurements
   (a) Temperature
   (b) Density
   (c) Specific surface area (SSA)
   (d) Stratigraphy, including snow grain type and size as well as hand hardness
   (e) Salinity

First, a mostly wooden instrument stand was carefully placed over an untouched snow cover (Fig. 3.2, left). The stand had two crossbars for radar measurements at heights of approximately 1 m and 1.5 m, depending on the bearing capacity of the snow cover. The radars used for studying microwave penetration were commercial, off-the-shelf Endress+Hauser Micropilot radars FMR54 (C band, ~6 GHz) and FMR51 (K band, ~26 GHz). Their main parameters are summarised in Table 3.2. Such radars are commonly used in industrial applications for continuous monitoring of a material level in a tank. The radar measurements were recorded first at the lower 1 m height, then at the higher 1.5 m height, repeated at the lower height, and then duplicated with the other radar using the manufacturer's licensed FieldCare

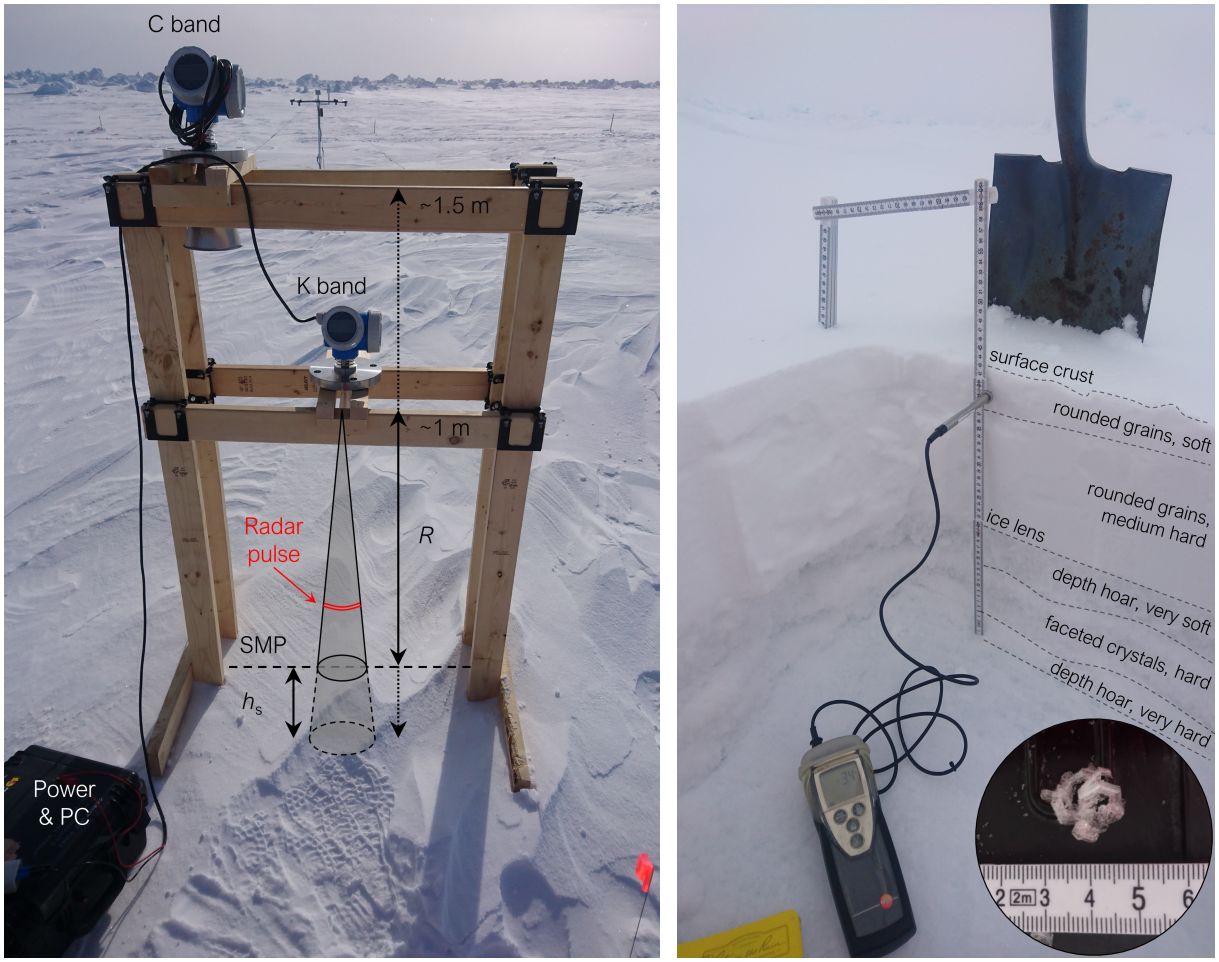

Figure 3.2. (Left) Photograph illustrating the setup using the off-the-shelf radars. R is range, h_s is snow depth, and the dashed line across the radar footprint shows the SnowMicroPen (SMP) measurement line. (Right) Snowpit MYI OIB on 18 May 2018 (Fig. A.3) while measuring the temperature profile overlaid with annotations of different snow layers. The dashed lines indicate approximate transitions between layers. The inset in the lower-right corner of the photo illustrates the centimetre-scale depth hoar crystals that were found in the lower layers.

software on a laptop computer. The software outputted the returned power in dB as a function of distance from the radar. During the first radar measurement at each measurement height, the range to the snow surface was recorded with a ruler to compare the location of the air–snow interface in the radar data. At two study locations, called FYI temporal and MYI temporal, the radar measurements were repeated every other day in the exact same location to record short time series of the radar response and therefore, only snow depth was recorded with a thin metal probe. The more destructive penetrometer and snow pit measurements, described in the following paragraphs, were done only on the last sampling day.

Next, the radars and the instrument stand were carefully removed with minimal disturbance to the snow. A high-resolution snow penetrometer, SnowMicroPen (SMP; Schneebeli et al., 1999), was used to sample the snow cover across the radar footprint every 10–25 cm (dashed line in Fig. 3.2, left). The SMP measures high-resolution profiles of penetration force when the measurement tip at the end of a metal rod is driven with constant speed vertically

Radar	Frequency	Beamwidth	Footprint[a]	Accuracy
FMR54	~6 GHz	23°	0.41/0.61 m	±6 mm
FMR51	~26 GHz	18°	0.32/0.47 m	±2 mm

Table 3.2. Summary of the radar parameters reported by the manufacturer Endress+Hauser.

[a] In diameter, beam-limited, range 1/1.5 m

into the snow pack. Proksch et al. (2015) empirically linked the penetration force to physical snow properties, such as density and specific surface area (SSA, surface area per unit mass). These derivatives are used here only for illustrative purposes, as recalibration might be necessary for the snow pack on the Arctic sea ice but also due to instrument hardware updates (Proksch et al., 2015; King et al., 2020b) but that is out of scope for this study.

After the SMP measurements, the disturbed snow was cleared and a vertical wall of snow was prepared in a way that it was shadowed from direct sunlight (Fig. 3.2, right). First, a snow temperature profile was recorded using a digital thermometer (testo 110 with a stainless steel food probe) in 2–5 cm vertical resolution. Second, 100 cm^3 (6 cm × 3 cm × 5.5 cm) samples of snow were extracted using a light-weight box cutter (also known as the Taylor-LaChapelle cutter) in 3 cm vertical resolution and weighed on a digital scale for the density measurement. Third, the snow was sampled in 3 cm intervals for an SSA profile using the IceCube instrument (A2 Photonic Sensors; Gallet et al., 2009). Fourth, the different snow layers were identified based on snow grain shape and average size, determined with a crystal card and a magnifying glass, and a hand hardness test by the observer. The grain shape and hardness scales follow the classification in Fierz et al. (2009). Last, samples of snow were collected in 3–5 cm resolution to plastic bags, allowed to melt in a heated tent, and measured for salinity the following day using the WTW Conductivity portable meter ProfiLine Cond 3110.

For the analysis, the radar measurements were aligned with the SMP and snow pit measurements using the manually measured range between the radar and the snow surface. The vertically averaged bulk density of snow from the box cutter measurements was used for calculating the propagation speed of the radar wave in snow according to Eqs. (2.5) and (2.7) to adjust the radar range in snow. The radar return power was converted to linear scale using Eq. (2.3) and normalised to the maximum power for a readily determination of the dominant scattering horizon. The location of the maximum power (normalised power equals 1) was taken as the location of the main scattering horizon.

3.3 Results and discussion

In this section, two opposing examples of the detailed snow studies together with the longer time series of radar response are presented and discussed. The remaining figures that summarise the measurements are included in Appendix A of this thesis and indexed in Table 3.1.

The observed general structure of the snow cover was typical for the Arctic sea ice. Closest to the snow–ice interface was a low-density, large-grained layer of depth hoar underlying a

wind slab layer with smaller, rounded grains and higher density (Fig. 3.2, right). Many of the studied snow covers had a layer of melt forms or even an ice lens between them indicating a warmer period earlier that winter. Freezing drizzle on 15 May created a thin, icy crust on the surface and snowfall on 22–23 May brought up to 10 cm of very soft, new snow. In general, the snow cover on FYI was relatively thin with bottommost layers reaching up to 12 ppt in salinity, whereas snow on MYI was thicker but fresh (non-saline).

During the measurement period 11–24 May, the air temperature rose close to and even above −5 °C (Fig. 3.1d) increasing the possibility of liquid water presence in the snow cover and subsequently, also the possibility of changes to the dielectric properties of snow. However, liquid water content (LWC) profiles were not measured as part of the detailed snow studies.

Figure 3.3 shows the measurements carried out on the snow and sea-ice thickness transect, i.e., at the location called snow pit FYI transect, on 22 May and represents the expected radar behaviour. From a 20 cm thick snow cover, the main scattering horizon for the C band radar originated exactly from the snow–ice interface whereas the K band microwaves were reflected from the air–snow interface regardless of the measurement height. The difference in the range-corrected distance between the peaks of the two frequencies was in excellent agreement with the snow depth. Both radar frequencies seemed surprisingly unaffected by the high salinity of 12 ppt in the bottommost 5 cm of the snow pack and the relatively warm snow temperature ranging from −6 °C to −3 °C. Increased salinity and temperatures close to freezing have been reported to increase microwave absorption and shift the main scattering horizon upwards.

The measurements conducted at the snow pit MYI buoy on 14 May are shown in Fig. 3.4. Here, the radar measurements were affected by a few centimetres thick, high-density, icy layer approximately 20 cm above the snow–ice interface. All but one of the radar returns placed the main scattering horizon to this layer or slightly above it. For an unknown reason, the C band measurement from the higher measurement height had the strongest return about 15 cm higher than the respective K band measurement, although similar in shape, placing it above the air–snow interface. This particular measurement was regarded erroneous. In addition, it must be noted that the thickness of the snow cover directly under the radar was about 32 cm (increasing from left to right), but as the disturbed snow was cleared for the snow pit measurements, the resulting height of the snow pit wall was 42 cm.

Figure 3.5 shows the evolution of the radar return signals from the exact same snow at the study location FYI temporal. In the beginning of the time series on 11 May, the higher-frequency K band microwaves reflected from or slightly below the air–snow interface whereas the lower-frequency C band microwaves expectedly penetrated deeper. However, the C band main scattering horizon seemed to correspond to a high-density layer of melt forms, which was located at 7–13 cm above the ice surface in the snow pit measurements on 24 May, rather than to the snow–ice interface. Later on by 22 May, the location of the strongest C band return had migrated upward to less than 10 cm below the snow surface. The K band penetration into snow was even more variable with the dominant scattering horizon

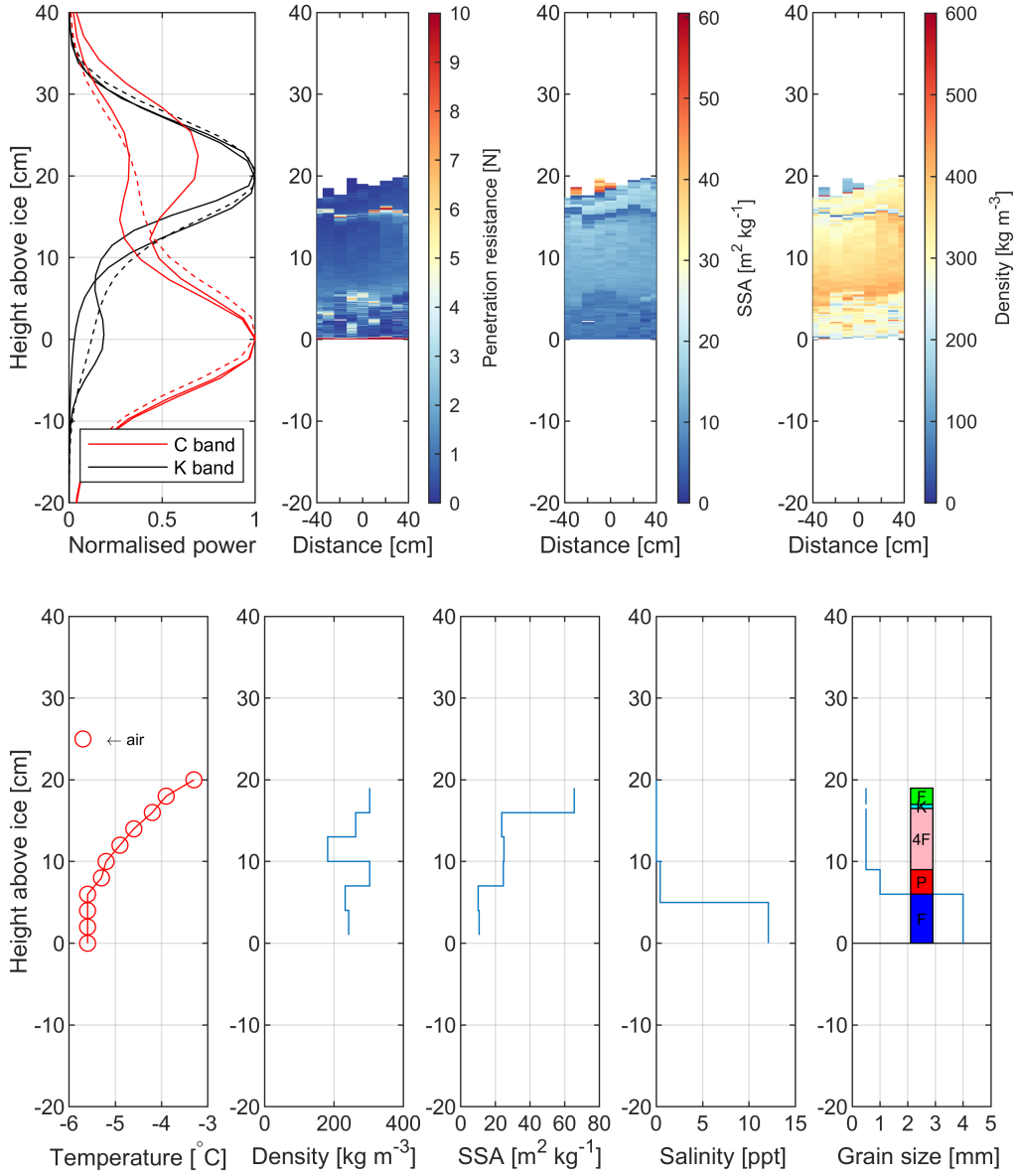

Figure 3.3. Snow pit FYI transect on 22 May 2018. (Top) The first panel shows the normalised radar returns for C (red) and K bands (black) and for the lower (solid) and higher (dashed) measurement height. The next three panels show the SnowMicroPen measurements across the radar footprint, where zero distance indicates directly under the radar at the middle of the instrument stand and positive distance is to the right. (Bottom) Standard snow pit measurements. SSA stands for specific surface area. Letter code for hand hardness: very soft, F (fist); soft, 4F (4 fingers); medium, 1F (1 finger); hard, P (pencil); very hard, K (knife blade); ice, I (ice). Colour code for snow grain type: precipitation particles, lime; decomposing and fragmented precipitation particles, forest green; rounded grains, light pink, faceted crystals, light blue; depth hoar, blue; melt forms, red; ice formations, cyan (Fierz et al., 2009).

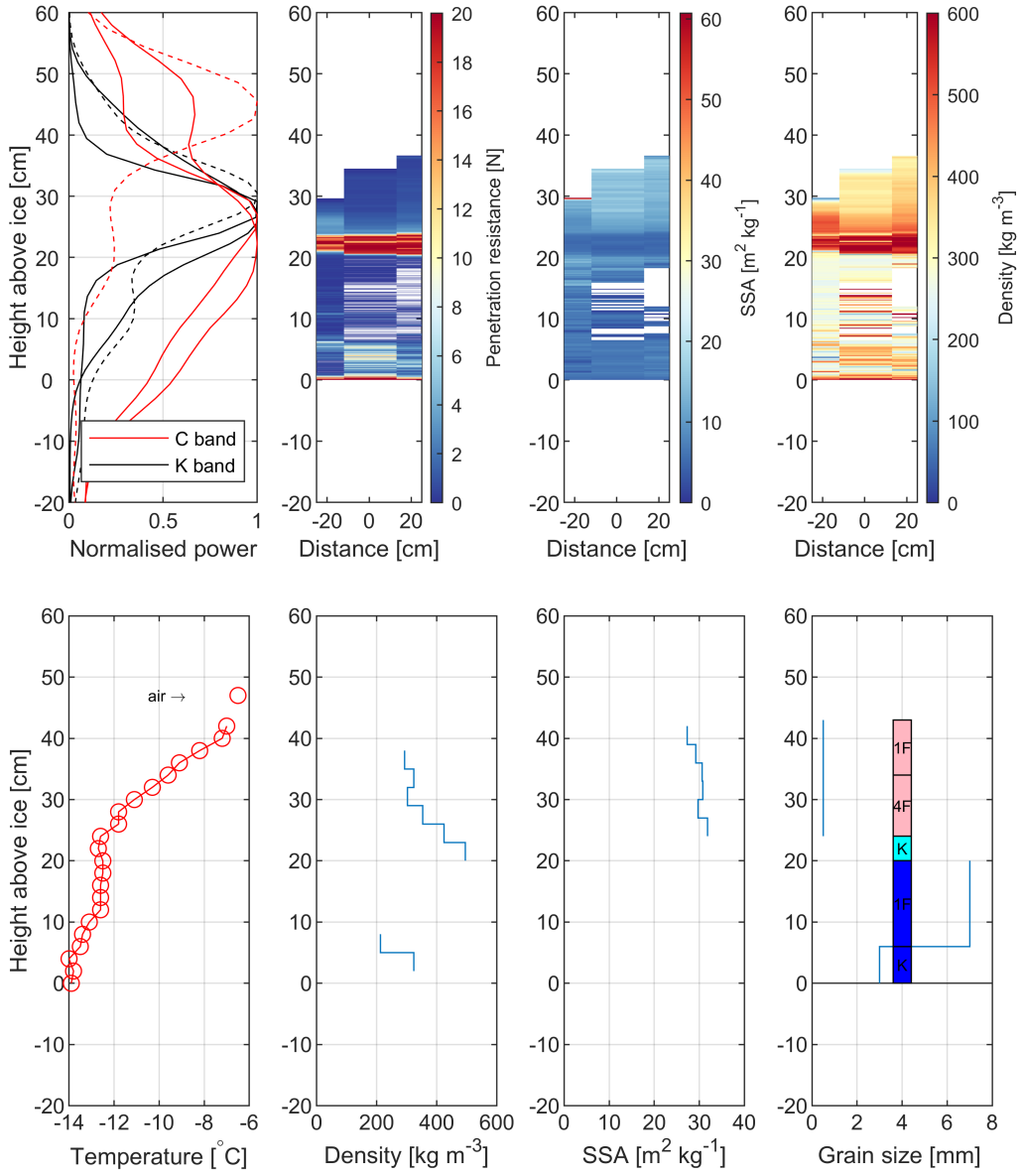

Figure 3.4. Snow pit MYI buoy on 14 May 2018. (Top) The first panel shows the normalised radar returns for C (red) and K bands (black) and for the lower (solid) and higher (dashed) measurement height. The next three panels show the SnowMicroPen measurements across the radar footprint, where zero distance indicates directly under the radar at the middle of the instrument stand and positive distance is to the right. Note that snow depth for the radars and penetrometer was about 10 cm less than for the snow pit measurements (top). (Bottom) Standard snow pit measurements. SSA stands for specific surface area. Letter code for hand hardness: very soft, F (fist); soft, 4F (4 fingers); medium, 1F (1 finger); hard, P (pencil); very hard, K (knife blade); ice, I (ice). Colour code for snow grain type: precipitation particles, lime; decomposing and fragmented precipitation particles, forest green; rounded grains, light pink, faceted crystals, light blue; depth hoar, blue; melt forms, red; ice formations, cyan (Fierz et al., 2009). The salinity profile is not shown, because all MYI snow pits had zero salinity.

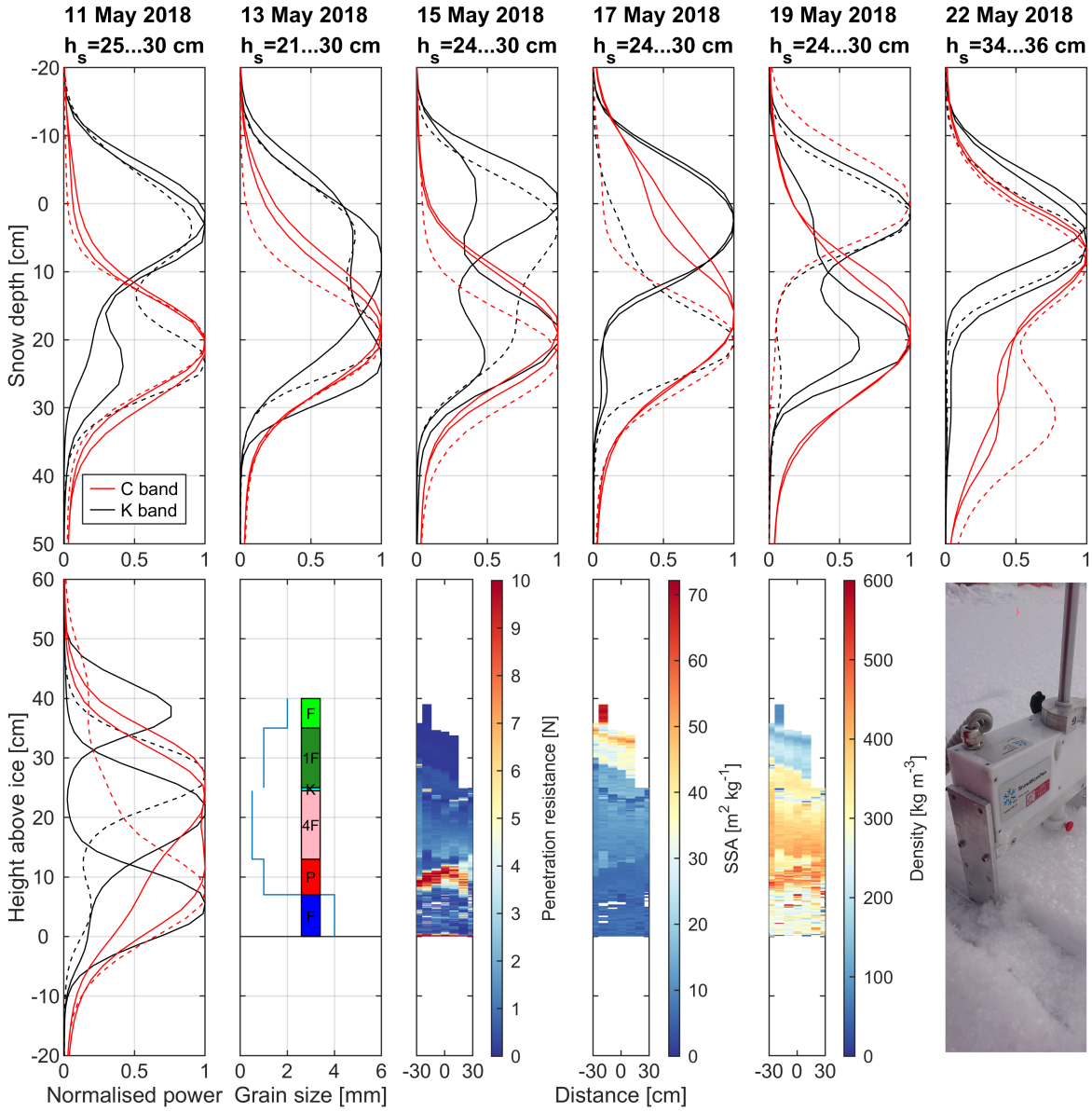

Figure 3.5. Measurements at the study location FYI temporal. (Top) Repeated C (red) and K band (black) radar measurements for the lower (solid) and higher (dashed) measurement height between 11 and 22 May 2018 without detailed snow pit measurements. Note that the vertical axis is normalised to the snow surface and converted into snow depth. Range of snow depth values probed under the radar are indicated above each panel. (Bottom) Radar measurements on 24 May 2018 followed by stratigraphy and penetrometer measurements. SSA stands for specific surface area. Note that the vertical axis is now normalised to the ice surface. Letter code for hand hardness: very soft, F (fist); soft, 4F (4 fingers); medium, 1F (1 finger); hard, P (pencil); very hard, K (knife blade); ice, I (ice). Colour code for snow grain type: precipitation particles, lime; decomposing and fragmented precipitation particles, forest green; rounded grains, light pink, faceted crystals, light blue; depth hoar, blue; melt forms, red; ice formations, cyan (Fierz et al., 2009). The photograph in the bottom right corner shows a close-up of the SnowMicroPen instrument and illustrates the softness of the topmost layers.

changing between the snow surface and the melt form layer or both showing double-peak behaviour. Also opposing behaviour depending on the measurement height was observed for both radars, on 17 May for K band and on 19 May for C band. Very likely reasons for the decrease in penetration depth could be the increased temperature (air temperature peaked at −0.9 °C on 19 May, Fig. 3.1d) and possible wetness of the snow cover during the measurement period. Unfortunately, neither of those parameters were measured at this study location. The new snow accumulated during the snowfall on 22–23 May remained mostly undetected by the radars due to the very low density and thus, lack of dielectric contrast between air and snow. The top layers up to a total thickness of 15 cm consisted of (fragmented) precipitation particles and were so soft that only one of the SMP measurements captured the full profile, while for most of them the instrument did not register enough resistance.

In summary, the radars were operated at nine locations recording a total of 108 radar returns divided equally between the C and K band frequencies and in 2:1 ratio between the lower and higher measurement height. For the C band radar, the dominant scattering surface was closer to the air–snow interface in 54 % of the returns, whereas in 39 % of the returns, all in snow on FYI, the strongest signal originated closer to the snow–ice interface. A minority (7 %) of the dominant scattering horizons seemed to be located above the snow surface (Fig. A.4) indicating perhaps a measurement error due to possible, unrecorded movement of the instrument stand into the snow, although still within the range resolution of the radars (about 2.9 cm for the C band radar and about 2.2 cm for the K band radar). For the K band radar, a clear majority, 81 %, of the dominant returns were located within the range resolution distance of 2–3 cm to the air–snow interface, whereas a small fraction, 17 %, originated closer to the snow–ice interface. One single return was located a few centimetres below the snow–ice interface within the sea ice (Fig. A.1).

Altogether, the analysis of microwave penetration was challenging and very dependent on the prevailing conditions. All studied snow packs had some morphological features, such as a surface crust, an ice lens, or a melt form layer of varying thickness, that could have influenced the radar wave propagation. Additionally, the air temperature was close to or even above −5 °C for the majority of the study period increasing the possibility of liquid water and resulting microwave absorption in the snow pack (Barber et al., 1995). Further inaccuracies may arise from the radar parameters allowing a range resolution of approximately 3 cm. Inarguably, FMCW radars would have been able to acquire more detailed radar profiles increasing the sensitivity to thin layers (Marshall et al., 2007) and perhaps also resolve thin (< 10 cm) snow thicknesses often encountered on level FYI. The thinnest snow pack measured with the radars was about 9 cm in thickness at the snow pit FYI OIB (Fig. A.2) where neither radar detected the snow–ice interface.

Choosing commercial, off-the-shelf radars, such as the Endress+Hauser Micropilot radars used here, over purpose-built radars may save for the trouble and costs of designing, although additional costs may be inflicted by software license costs to operate the radar. Rather than being open source, the details of the radars as well as their software and algorithms can be trade secrets that the manufacturers are unwilling to disclose. That can make

them seem like black boxes where the exact processing steps between input and output are unknown. However, the rugged design of the industrial off-the-shelf radars could potentially make them useful in remote continuous monitoring of the local snow and sea-ice backscatter in harsh Arctic environments, where the risk of loosing an expensive FMCW radar would be too high.

3.4 Conclusions

The field trials with commercial pulsed radars at the C and K band frequencies showed that the theoretically deeper-penetrating C band radar had its dominant scattering horizon more often closer to the air–snow interface than to the snow–ice interface. The latter was detectable only on FYI. Most K band measurements were expectedly reflected at or close to the snow surface, although in few occasions they penetrated deeper. Based on these results, retrieving snow depth determined by the difference in distance between the main scattering surfaces at C and K band is possible only on FYI and even then only under certain conditions. The analysis was hampered by morphological features in the snow cover and relatively high temperatures close to freezing confirming findings of previous studies. Further insights could be gathered including data from the large number of airborne instruments on the OIB survey that flew over the site approximately one month before the field experiments described here were conducted.

Direct comparison between commercial and purpose-built radars is not possible based on this study because both radar types were not deployed simultaneously. Future studies should consider deploying both kinds of radars together with coincident extensive investigations on the physical properties of the snow pack, including liquid water content. It is also recommended to schedule the study period earlier in the year than May to avoid temperatures close to freezing complicating the analysis. Another desirable application for these off-the-shelf radars would be long-term autonomous observation of the changes in snow and sea-ice backscatter behaviour over a range of environmental conditions.

Acknowledgements

J. Hildebrand and R. ten Boer are acknowledged for assisting in the data collection in May 2018. Polar Continental Shelf Program (PCSP), Natural Resources Canada, Department of National Defense (DND) at CFS Alert, Defense Research and Development Canada (DRDC), Environment and Climate Change Canada (ECCC), Kenn Borek Air, and the communities and Hunters and Trappers Associations of Resolute Bay and Grise Fjord are acknowledged for supporting the field program. Special thanks to A. Platt (ECCC), C. Brown, J. Milne, J. Higgins and M. Simms at DRDC for all their efforts in logistics, and Major C. Stiles (CO), R. Hansen (SWO) and R. Lutz (Alta SWO) at CFS Alert. The MAP — Last Ice Program is led by C. Michel, funded by Fisheries and Oceans Canada (DFO) Science. Autonomous sea ice measurements (air temperature and snow depth) from 5 May 2018 to 31 May 2018 were obtained from https://www.meereisportal.de (grant: REKLIM-2013-04).

Chapter 4

High-resolution snow depth using an airborne radar

This chapter has been published as

Jutila, A.[1], King, J.[2], Paden, J.[3], Ricker, R.[1], Hendricks, S.[1], Polashenski, C.[4,5], Helm, V.[1], Binder, T.[1,a], and Haas, C.[1]: **High-Resolution Snow Depth on Arctic Sea Ice From Low-Altitude Airborne Microwave Radar Data**, *IEEE Transactions on Geoscience and Remote Sensing*, https://doi.org/10.1109/TGRS.2021.3063756, 2021.

[1] *Alfred Wegener Institute, Helmholtz Centre for Polar and Marine Research, Bremerhaven, Germany*
[2] *Climate Research Division, Environment and Climate Change Canada, Toronto, ON, Canada*
[3] *Center for Remote Sensing of Ice Sheets, University of Kansas, Lawrence, KS, USA*
[4] *US Army Corps of Engineers, Cold Regions Research and Engineering Laboratory Alaska Projects Office, Fort Wainwright, AK, USA*
[5] *Thayer School of Engineering, Dartmouth College, Hanover, NH,USA*
[a] *Currently at: Ibeo Automotive Systems GmbH, Hamburg, Germany*

Author contributions

AJ calibrated the radar data, developed the snow depth retrieval method, carried out the analysis, and wrote the manuscript. JP provided support during the radar data calibration and JK assisted in the snow depth retrieval. AJ, RR, SH, VH, and TB collected the data. CP provided the data for validation. JK, JP, RR, SH, CP, and CH contributed to the discussion and provided input during the writing process.

Abstract. We present new high-resolution snow depth data on Arctic sea ice derived from airborne microwave radar measurements from the IceBird campaigns of the Alfred Wegener Institute (AWI) together with a new retrieval method using signal peakiness based on an intercomparison exercise of colocated data at different altitudes. We aim to demonstrate the capabilities and potential improvements of radar data, which were acquired at a lower altitude (200 ft) and slower speed (110 kn) and had a smaller radar footprint size (2-m diameter) than previous airborne snow radar data. So far, AWI Snow Radar data have been derived using a 2–18-GHz ultrawideband frequency-modulated continuous-wave (FMCW) radar in 2017–2019. Our results show that our method in combination with thorough calibration through coherent noise removal and system response deconvolution significantly improves the quality of the radar-derived snow depth data. The validation against a 2-D grid of *in situ* snow depth measurements on level landfast first-year ice indicates a mean bias of only 0.86 cm between radar and ground truth. Comparison between the radar-derived snow depth estimates from different altitudes shows good consistency. We conclude that the AWI Snow Radar aboard the IceBird campaigns is able to measure the snow depth on Arctic sea ice accurately at higher spatial resolution than but consistent with the existing airborne snow radar data of NASA Operation IceBridge. Together with the simultaneous measurements of the total ice thickness and surface freeboard, the IceBird campaign data will be able to describe the whole sea-ice column on regional scales.

4.1 Introduction

A key factor contributing to our current limited knowledge of snow on sea ice and its importance to polar climate is the lack of representative snow observations. As a layer separating dynamic sea ice and atmosphere, snow exhibits heterogeneity that evolves over time and varies in space through different scales. Characterizing the spatial and temporal variability of snow with point scale *in situ* measurements in a harsh and dynamic sea-ice environment is logistically challenging (Webster et al., 2018). Satellite remote sensing of snow depth offers a practical solution through two main approaches. Brightness temperatures from multifrequency passive microwave sensors (Kilic et al., 2019), their gradient ratios (Markus and Cavalieri, 1998; Comiso et al., 2003; Rostosky et al., 2018), or combined with emission modeling (Maaß et al., 2013) are found to correlate with snow depth. A dual-altimetry method uses radars of two different frequencies, of which one is assumed to penetrate the snow, while the other is used to retrieve the air–snow interface (Guerreiro et al., 2016; Lawrence et al., 2018). Recently, Kwok and Markus (2018) and Kwok et al. (2020) presented a combination of radar and laser satellite altimeters to estimate snow depth. However, data from satellite systems are constrained by spatiotemporal coverage, spatial resolution and differences in footprint size, surface roughness, ice type, and availability of ground measurements for validation (Webster et al., 2018). Airborne observations are often used to validate satellite measurements even though they share many of the same constraints. In addition, measurements from different platforms need intercomparison to minimize uncertainty if the blended analysis is required.

Snow on Arctic sea ice modulates the thickness of the underlying ice (Maykut and Untersteiner, 1971): in winter, it retards ice growth due to its low thermal conductivity (Sturm, 2002); in spring and summer, the high albedo of snow delays surface melt and melt pond formation (Perovich et al., 2007; Perovich and Polashenski, 2012). Moreover, snow contributes significantly to sea-ice mass balance through snow-ice formation (Merkouriadi et al., 2017; Granskog et al., 2017; Rösel et al., 2018). In addition, snow loading is a critical parameter to estimate sea-ice thickness from satellite radar and laser altimeter measurements through the assumption of hydrostatic equilibrium (Laxon et al., 2003; Giles et al., 2007). Studies have shown that the widely used snow depth climatology in Warren et al. (1999), derived from *in situ* measurements on multiyear ice (MYI) during 1951–1991, requires adjustments for applications on Arctic sea ice due to large interannual variability and basin-wide thinner, younger ice (Kurtz and Farrell, 2011; Farrell et al., 2012; Webster et al., 2014, 2018). Despite the high importance of snow on sea ice to polar climate, "snow depth on sea ice is essentially unmeasured" as expressed by the Intergovernmental Panel on Climate Change (IPCC) Special Report on the Ocean and Cryosphere in a Changing Climate (SROCC) (Meredith et al., 2019).

Frequency-modulated continuous-wave (FMCW) radars have been used for snow research for more than 40 years and on airborne platforms since the 2000s (Marshall and Koh, 2008). Since 2009, NASA's Operation IceBridge (OIB) campaigns have included an airborne ultrawideband FMCW radar, known as the Snow Radar, developed by the Center for Remote Sensing of Ice Sheets (CReSIS) at the University of Kansas (Koenig et al., 2010). Through the duration of OIB, several algorithms have been developed to estimate snow depth from the Snow Radar echograms (Kwok et al., 2011; Kurtz and Farrell, 2011; Kurtz et al., 2013, 2014; Koenig et al., 2016; Kwok and Maksym, 2014; Newman et al., 2014; Kwok et al., 2017). For descriptions of the algorithms, we ask the reader to refer to the brief summaries in Kwok et al. (2017). The number of radar returns, and therefore potential snow depth estimates, collected in a full season of Western Arctic OIB surveys is in the order of 10^6, clearly surpassing the number and spatial coverage of current seasonal *in situ* measurements of snow depth on sea ice.

Despite the recent efforts of the science community in the past decade to overcome the sampling deficiency with manual measurements of snow depth from dedicated field campaigns with limited spatial and temporal coverage, point measurements from drifting autonomous measuring platforms, such as ice mass-balance buoys (IMBs) (Richter-Menge et al., 2006; Polashenski et al., 2011; Planck et al., 2019; Jackson et al., 2013), and snow buoys, or extensive airborne campaign programs, such as OIB, the current observations still are not enough to monitor the state of snow on sea ice at the high spatial resolution, therefore introducing a key knowledge gap and uncertainty (Meredith et al., 2019). Moreover, single ground transects are not sufficient for validation of snow depth estimates from snow radars since they are not suitable for capturing the variability within the radar footprint (Newman et al., 2014). Therefore, we require ground surveys with a true 2-D grid layout. The 2-D validation can improve accuracy and decrease the uncertainty of radar-derived snow depth estimates while also limiting the necessity for spatial averaging. In addition, accurate esti-

mates of snow depth on sea ice combined with simultaneously acquired information from other airborne instruments measuring the sea ice would allow describing the whole layer of sea ice and snow.

In this article, we present new data of snow depth on sea ice derived from airborne ultrawideband FMCW microwave radar measurements collected during the Alfred Wegener Institute's (AWI) IceBird campaigns between 2017 and 2019. We evaluate the performance of the AWI Snow Radar at low altitude (200 ft) and demonstrate improvements associated with a decrease in radar footprint size over previous acquisitions. We validate the data with multiple passes over a 2-D grid of *in situ* snow depth measurements on level landfast first-year ice (FYI). To retrieve the snow depth, we apply multiple retrieval algorithms, of which one is based on signal peakiness and developed by us, using the open-source pySnowRadar package as a framework for processing echogram data from CReSIS snow radar systems.

4.2 Data and Methods

We start by giving a short description of the radar system (see Section 4.2.1) and introducing the campaigns where we used the radar (see Section 4.2.2). We then continue by describing the calibration workflow of raw data (see Section 4.2.3), snow depth retrieval (see Section 4.2.4.1), and postprocessing (see Section 4.2.4.3).

4.2.1 Snow Radar Description

The ultrawideband microwave radar, which we from now on refer to as Snow Radar, is a 2–18-GHz airborne FMCW radar developed by CReSIS at the University of Kansas. Since 2009, different versions of the Snow Radar have been operated as part of OIB to measure snow depth on sea ice (Koenig et al., 2010; Yan et al., 2017a; Arnold et al., 2018). After a testing phase in 2015–2016, a similar radar was deployed on the AWI IceBird airborne sea-ice campaigns between 2017 and 2019. The radar system consists of a chirp generator based on a direct digital synthesizer (DDS) with a frequency multiplier and a downconverter, dual-polarized transmitter and receiver antennae, intermediate frequency section, and a digital acquisition unit. The radar has the full polarimetric capability with four channels VV, HH (co-polarized), VH, and HV (cross-polarized), which can be used to acquire further information about the snowpack properties. A detailed technical description of the radar is given in Yan et al. (2017a), and the key parameters are summarized in Table 4.1.

Following Panzer et al. (2013), the theoretical range resolution of the radar in free space is 0.94 cm, determined by:

$$\Delta R = \frac{c}{2B} \tag{4.1}$$

where c is the speed of light in a vacuum and B is the radar bandwidth. The propagation speed of the wave in snow, c_s, is lower than in free space by a factor of approximately 0.81

assuming a snow density of 0.3 $g \cdot cm^{-3}$ and results in a range resolution of 1.14 cm

$$\Delta R = \frac{kc_s}{2B}, \text{ where } c_s = \frac{c}{\sqrt{\varepsilon'_{ds}}} = c(1 + 0.51\rho_{ds})^{-\frac{3}{2}} \tag{4.2}$$

including the effect of windowing to reduce sidelobes ($k = 1.5$, Hanning). ε'_{ds} is the relative permittivity of dry snow determined by the density of dry snow, ρ_{ds}, in $g \cdot cm^{-3}$ (Ulaby et al., 1986).

For a smooth surface, the cross-track resolution equals the diameter of the pulse-limited nadir-looking footprint

$$r_{pl} = 2\sqrt{\frac{kch}{B}} \tag{4.3}$$

where h is the radar altitude above ground level. For a rough surface, the footprint size increases depending on the topographic height of the surface features illuminated in the radar beam and their location off-nadir. The along-track resolution

$$r_{at} = 2h \tan\frac{\beta}{2} \tag{4.4}$$

depends on the half-power beamwidth for the synthetic aperture, β, in addition to the altitude. The half-power beamwidth is defined in Ulaby et al. (1982) as

$$\beta = \frac{\lambda}{2L} \tag{4.5}$$

where λ is the wavelength at the center frequency and L is the unfocused synthetic aperture length. The latter is defined as

$$L = \frac{nv}{\text{PRF}} \tag{4.6}$$

where $n = 8 \cdot 4 = 32$ is the product of the presums made in hardware and software, v is the velocity of the platform, and PRF is the pulse repetition frequency. The AWI Snow Radar switches between vertically and horizontally polarized transmit modes; thus, the effective PRF is halved relative to the OIB Snow Radar to approximately 2 kHz. Using the radar parameters from Table 4.1, the footprint sizes of 2.6 and 1.0 m in the cross- and along-track directions for the low (200 ft) altitude surveys of the AWI Snow Radar are much smaller than those of the OIB Snow Radar and allow for more accurate retrievals due to reduced clutter from off-nadir snow and ice. Assuming elliptical footprints with along- and cross-track radii as the semimajor and semiminor axes, respectively, the low-altitude (200 ft) footprint is only 3%–7% in size relative to the ones from high altitude (1500 ft). Also, the nominal along-track sample spacing of the AWI Snow Radar at the low survey altitude is improved compared to the high-altitude acquisitions.

Table 4.1. Snow Radar parameters for AWI IceBird missions and for NASA's Operation IceBridge (OIB) for comparison

Parameter	**AWI IceBird**		**Equation**	**OIB (2017–2019)**
Radar version	snow5			snow8
Bandwidth	2–18 GHz			2–18 GHz
Pulse length	240 μs			240 μs
Pulse repetition frequency (PRF)	3.9 kHz			3.9 kHz
Sampling frequency	125 MHz			250 MHz
Analog-to-digital converter (ADC)	14-bit			14-bit
Antennae	Dual-pol Horn Ainfo LB-SJ-2018			Single-pol Horn ETS Lindgren 3115
Range resolution	0.94–1.14 cm		(4.1) & (4.2)	0.94–1.14 cm
Nominal survey altitude	61 m (200 ft)	457 m (1500 ft)		457 m (1500 ft)
Nominal survey velocity	57 m $\cdot$ s^{-1} (110 kn)	82 m $\cdot$ s^{-1} (160 kn)		129 m $\cdot$ s^{-1} (250 kn)
Cross-track footprint diameter	2.6 m	7.2 m	(4.3)	7.2 m
Along-track footprint diameter	1.0 m	5.1 m	(4.4)	13.0 m
Sample spacing	~4–5 m	~7–9 m		~5–6 m
Transmit power	100 mW	1000 mW		1000 mW

4.2.2 Deployments

The operational platforms for the AWI Snow Radar have been the Basler BT-67 research aircraft, Polar 5 and Polar 6 of the AWI (Alfred-Wegener-Institut Helmholtz-Zentrum für Polar- und Meeresforschung, 2016). The nadir-looking transmitter and receiver antennae were located side by side under the floor toward the aft of the aircraft (see Fig. 4.1). In addition to the Snow Radar, scientific instrumentation included an airborne laser scanner (ALS) for surface topography and snow freeboard measurements, an electromagnetic induction sounding instrument (EM-Bird) to measure total ice thickness (i.e., snow + ice thickness), an infrared radiation pyrometer for surface temperature, and a nadir-looking camera for surface type identification.

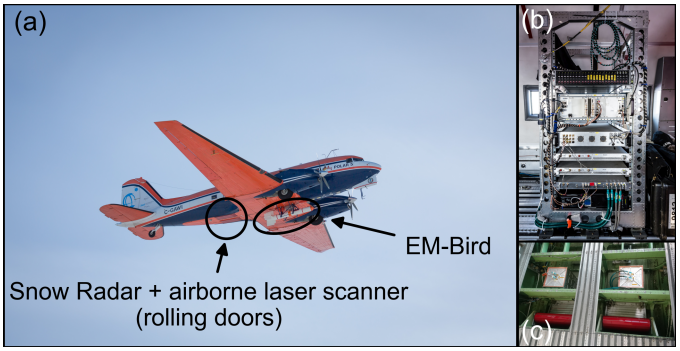

Figure 4.1. (a) AWI research aircraft Polar 5 with complete IceBird sea-ice survey instrumentation. (b) AWI Snow Radar instrument rack. (c) AWI Snow Radar horn antennae (gray cuboids) installed under the floor panels above the rolling doors (red cylinders).

The IceBird survey pattern over sea ice included surveys at two different altitudes. The outward leg of each mission was flown in our primary low-altitude survey mode of 200 ft with a slow surveying velocity of 110 kn. At this altitude, we were able to use all instruments mentioned above and collect high-resolution data. We prevented signal saturation at low altitudes by adding 10-dB attenuators to the Snow Radar transmitter. Approximately, every 15–20 min, the aircraft needed to ascend to 500 ft to monitor the EM-Bird sensor drift for postprocessing. This caused a transition in the Nyquist zone for the Snow Radar, thus introducing short data gaps. During the multipurpose return leg, the aircraft surveyed at higher altitude and speed to maximize operational range. Particularly, in 2019, the return leg was flown in a comparable configuration to most OIB surveys, at 1500 ft and 160 kn, with continuous measurements of the Snow Radar and ALS.

We have operated the AWI Snow Radar on three airborne campaigns over the Arctic sea ice in the Greenland, Lincoln, Beaufort, and Chukchi Seas and the Central Arctic Ocean (see Fig. 4.2 and Table 4.2). In 2017, the Snow Radar was operated during six sea-ice survey flights as part of the Polar Airborne Measurements and Arctic Regional Climate Model Simulation Project (PAMARCMiP) (Haas et al., 2010; Herber et al., 2012) from Eureka, Inuvik, and Utqiagvik (Barrow) between March 30 and April 10, 2017. In the following year, we operated the Snow Radar over sea ice in the Fram Strait during a flight from Longyearbyen to Station Nord on April 10, 2018, as part of the campaign RESURV79 focused on surveying Nioghalvfjerdsbrae (79 N) Glacier in Greenland. Between April 1 and April 10, 2019, we did a total of seven survey flights with the Snow Radar from Eureka and Inuvik during the campaign IceBird Win-

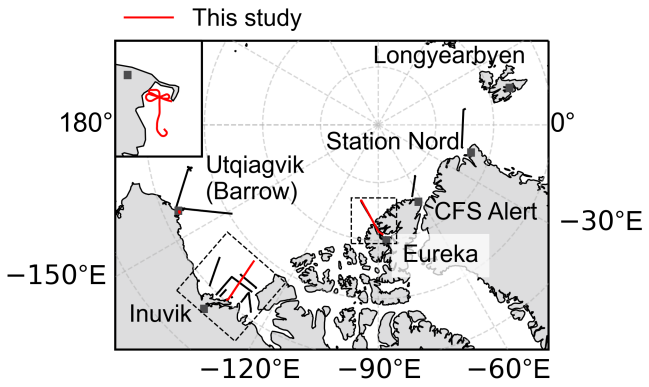

Figure 4.2. Airborne surveys with the AWI Snow Radar between 2017 and 2019 (see Table 4.2). The flight segments with the main focus in this article are highlighted in red, and the dashed squares indicate the extent of Figs. 4.9(a) and 4.10(a). The inset in the top-left corner shows a close-up of the short validation flight over the Elson Lagoon near Utqiagvik (Barrow) on April 10, 2017.

ter 2019, including areas in the Beaufort Sea not covered by OIB in that year. During these deployments, we recorded over 980 000 radar returns.

Our analysis focuses on three individual flights on April 10, 2017, April 2, 2019, and April 10, 2019 (see Fig. 4.2 and Table 4.2). The first flight coincided with *in situ* snow depth measurements carried out on landfast ice, which we used for validation. The surveys on April 2 and 10, 2019, contained long segments where flight tracks at two different survey altitudes overlapped. We used them for comparison to assess the effect of the survey altitude on the AWI Snow Radar measurements with the objective to quantify potential improvements of the low-altitude mode and evaluate the consistency with earlier OIB surveys.

4.2.3 Calibration

For calibration of the raw data, we used the MATLAB-based cresis-toolbox software provided by CReSIS (CReSIS, 2020a,b). Fig. 4.3 illustrates the workflow that followed the same principle steps of methods applied previously to retrieve snow depth from Snow Radar waveforms (Panzer et al., 2013; Kwok et al., 2017; Yan et al., 2017b; CReSIS, 2020b). The first major step was the removal of altitude-independent coherent noise [visible in Fig. 4.5(a) below as undulating lines above the sea-ice surface]. Using a low-pass boxcar filter with a sampling frequency of 1/7.5 Hz and a cutoff frequency of 1/30 Hz, we subtracted low-frequency along-track noise from the data resulting in only the high-frequency signal left in the data.

The next step was to analyze each data segment to detect specular targets by using an along-track discrete Fourier transform (DFT) over 512 range lines to extract the system response. Over the polar ocean and in calm wind conditions, we could use open water leads that were large enough (at least one Fresnel zone) as targets (Yan et al., 2017b). We detected sea-ice leads by comparing the coherent signal power in the 32 lowest frequency bins of the DFT with the incoherent power in the 425 highest frequency bins. When the power in the lowest frequency bins exceeded the power in the highest frequency bins by 25 dB, we further processed that block of 512 range lines to extract a waveform representing the system impulse response. This was done by motion compensating each range line followed by taking an average over all of them to achieve a high signal-to-noise ratio impulse response estimate. After collecting all the impulse responses from the blocks that satisfied the threshold, we tested the peak sidelobe ratio of each impulse response by deconvolving a sample range

Table 4.2. Airborne surveys with the AWI Snow Radar (see Fig. 4.2)

Flight ID[a]	Base	Mission	Altitude
20170330_01 20170330_02 20170330_03	Eureka, Canada	Nansen Sound, Arctic Ocean	low
20170402_01	Inuvik, Canada	Beaufort Loop	low
20170404_01 20170404_02	Inuvik, Canada	AltiKa track	low
20170406_01	Utqiagvik (Barrow), USA	Sentinel-3A track	low
20170408_01	Utqiagvik (Barrow), USA	ULS & UiTSat	low
20170410_01[b]	Utqiagvik (Barrow), USA	Elson Lagoon snow site	low
20180410_01	Longyearbyen, Norway	Fram Strait	high
20190401_01	Eureka, Canada	North of Ward Hunt ice shelf	low
20190402_01[b] 20190402_02[b]	Eureka, Canada	Nansen Sound, Arctic Ocean	low high
20190405_01 20190405_02	Eureka, Canada	Lincoln Sea	low
20190407_01 20190407_02 20190407_03 20190407_04	Inuvik, Canada	Beaufort Triangle	low high
20190408_01 20190408_01	Inuvik, Canada	Amundsen Gulf	low
20190410_01[b] 20190410_02[b]	Inuvik, Canada	ICESat-2 track	low high
20190410_03	Inuvik, Canada	Trail Valley Creek (over land)	high

[a] In format <date of flight (yyyymmdd)>_<flight segment>

[b] Flight segments with the main focus of interest in this paper, highlighted in red in Fig. 4.2

line from each block. We used the waveform with the lowest sidelobes for each segment to deconvolve that corresponding segment. If a data segment did not have any good waveforms (e.g., segments were flown over MYI with few leads), then we manually chose impulse responses from another segment with corresponding nominal survey altitude. Usually, there were only a few sufficiently good impulse responses found for each segment, and some segments had no impulse responses extracted that improved the sidelobes.

To apply deconvolution, we convolved the radar data with the inverse of the extracted system response, which we limited to 400 range bins before and 150 range bins after the mainlobe with a Tukey window. We limited the range bin extent to reduce the amount of noise included in the impulse response and because this lowered the sidelobes in a large

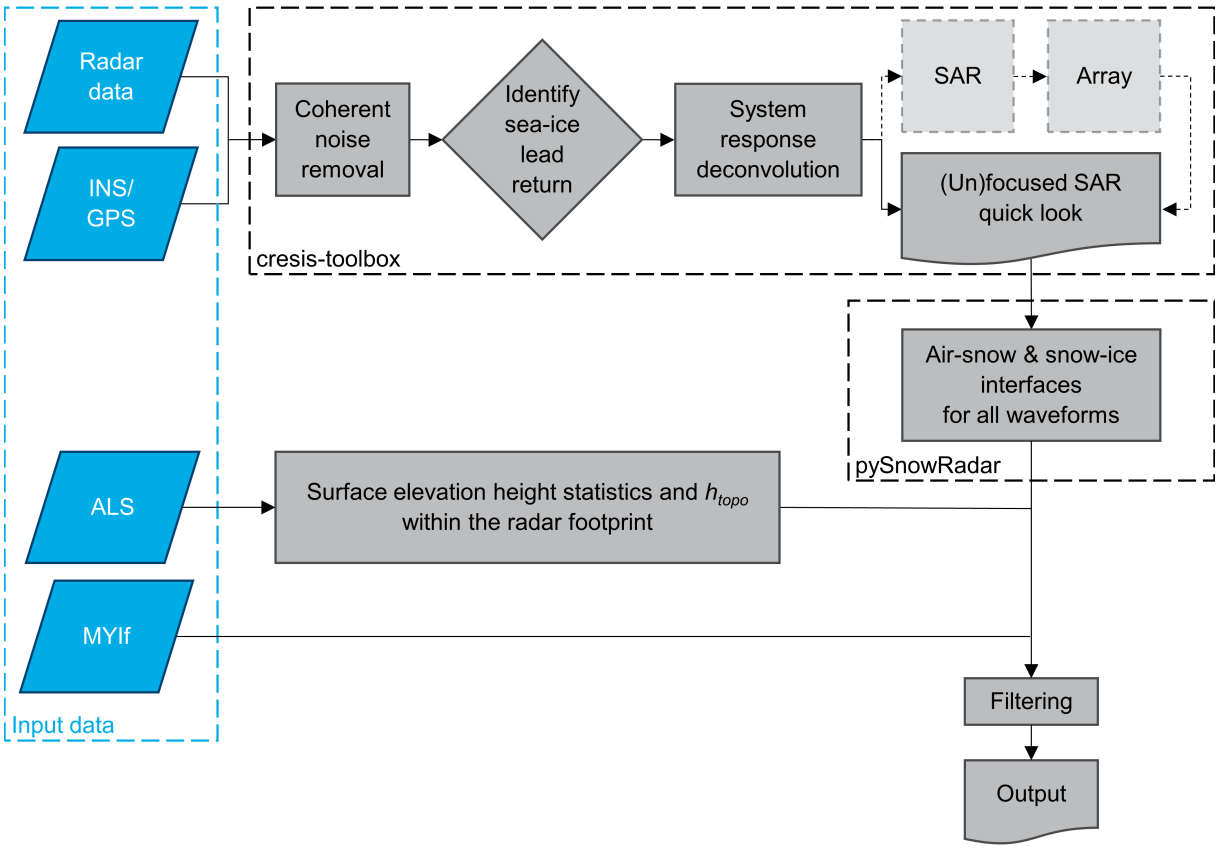

Figure 4.3. Principal steps of the AWI Snow Radar data calibration and processing.

enough region around the mainlobe to prevent sidelobes from disrupting snow thickness tracking. Good system response deconvolution will suppress the range sidelobes [visible in Fig. 4.5(b)] and improve the 3-dB range resolution, which, in turn, will enhance the clarity of air–snow and snow–ice interfaces.

As part of deconvolution, we radiometrically calibrated the data so that the peak power was scaled to $1/R^2$, where R is the range. We used the impulse response with the lowest sidelobes as the calibration target. We assumed that the power reflection coefficient from this target (specular sea water surface) should be 0 dB. We scaled all the data products by the amount required to scale this calibration target to 0 dB. In addition, we narrowed the frequency window from 2–18 GHz to roughly half, 4–11.5 GHz, to avoid amplifying high-frequency noise.

As the final step, we applied elevation compensation to correct for changes in platform altitude and truncated the radar data frames to the default CReSIS radar sea-ice mission depth range of 8 m above and 5 m below the surface. We used the output of these two main steps, an unfocused synthetic aperture radar (SAR) quick look product of the vertically co-polarized channel (VV), as an intermediate product for our further analysis.

4.2.4 Processing

4.2.4.1 pySnowRadar

We identified air–snow and snow–ice interfaces from the calibrated Snow Radar echograms using the open-source pySnowRadar package (King et al., 2020a). Python-based pySnowRadar provides a modular framework to extract, transform, and load Snow Radar data. The generalized structure of the package allows for rapid development and validation of retrieval algorithms with parallel processing capabilities to scale with compute infrastructure. Originally developed to use the Haar wavelet interface detection method introduced in Newman et al. (2014), pySnowRadar produces along-track snow depth estimates, which are largely insensitive to variations in mission-specific transmission power or receiver noise. However, methods described in Newman et al. (2014) have not previously been validated for the 2–18-GHz bandwidth radar version of the Snow Radar used by the AWI. Early investigations with the Haar wavelet method revealed incorrect interface detection especially when the air–snow interface was the dominant scattering surface. Therefore, to assess the suitability of this method, we developed a new interface picker module for comparison.

4.2.4.2 Peakiness method

Adapting an approach from satellite radar altimetry in Ricker et al. (2014), we used the concepts of left- and right-hand peakiness, $\mathrm{PP_l}$ and $\mathrm{PP_r}$, respectively, to determine correct interface locations and disregard ambiguous waveforms. To detect the air–snow interface, we first identified all local maxima (peaks) that were above the mean noise level of the first 100 range bins by a user-defined peak detection power threshold in the normalized, logarithmic-scale waveform, whereas, for the snow–ice interface, we did the same but using normalized, linear-scale data to decrease the number of possible interface locations. In general, maximum return power was assumed to correspond to the snow–ice interface, i.e., the largest change in the dielectric properties. If more than five peaks above the peak detection power threshold were found in the linear data at this stage, the algorithm does not return any interface locations for the waveform in question because reliable interface signal cannot be retrieved but regards it as ambiguous. For each peak identified from the logarithmic (linear) data, we calculated the left-hand (right-hand) peakiness value using the mean of N preceding (succeeding) range bins in the linear normalized data as defined by Ricker et al. (2014)

$$\mathrm{PP_l} = \frac{\tilde{s}_{\mathrm{peak}}}{\frac{1}{N}\sum_{i=1}^{N} \tilde{s}_{\mathrm{peak}-i}} \cdot N \tag{4.7}$$

$$\mathrm{PP_r} = \frac{\tilde{s}_{\mathrm{peak}}}{\frac{1}{N}\sum_{i=1}^{N} \tilde{s}_{\mathrm{peak}+i}} \cdot N \tag{4.8}$$

where $\tilde{s}_i = s_i / s_{\max}$ is the normalized waveform in linear scale, i is the range bin index, and N is the number of range bins. We chose $N = 10$ for the calculations as it equaled two times the 3-dB range resolution (see Section 4.3.1). We assigned the air–snow (snow–ice) interface to the first (last) peak identified from the logarithmic (linear) data that exceeded a user-defined left-hand (right-hand) peakiness value. An example of applying the method to a waveform is shown in Fig. 4.4. The four user-definable parameters described here were determined semiempirically through validation (see Section 4.3.2) and random test frames from each segment to ensure consistency (see Table 4.3).

Table 4.3. Waveform peak detection parameters: power thresholds (TH) in the logarithmic (log) and linear (lin) scales, and left-hand (l) and right-hand (r) peakiness (PP) threshold values

Flight ID	**Log-scale power**	**Lin-scale power**	**Left-hand peakiness**	**Right-hand peakiness**
	TH_{log}	TH_{lin}	PP_l	PP_r
20170410_01	0.7	0.2	20	20
20190402_01	0.6	0.2	20	20
20190402_02	0.6	0.5	20	30
20190410_01	0.6	0.2	20	20
20190410_02	0.6	0.5	20	30

4.2.4.3 Snow Depth Postprocessing

Following Newman et al. (2014), we characterized the variability of the sea-ice surface within the radar footprint with the nonparametric surface topography estimate h_{topo}, which is defined as the difference of the 95th percentile and the 5th percentile of the surface elevation height:

$$h_{\text{topo}} = h_{95} - h_{05}. \tag{4.9}$$

Here, we approximated the radar footprint to be circular with a radius corresponding to the theoretical smooth surface and cross-track footprint size. For the estimation of h_{topo}, we used data acquired with the onboard near-infrared (1064 nm), fast line-scanning ALS (Riegl VQ-580), which has an accuracy and precision of 25 mm. Resulting WGS84 surface elevation point clouds were gridded into 0.25- or 0.50-m lateral resolution for the low and high survey altitudes, respectively [see Fig. 4.4(a)].

Following again the approach of Newman et al. (2014), we set an upper limit of 0.5 m for h_{topo} where surface elevation data from the ALS were available. This was to include surface features on level ice, such as sastrugi, but to exclude potentially false snow depth estimates in the heavily deformed sea-ice environment. We filtered out snow depth estimates that were acquired during the EM-Bird calibration maneuvers using a simple elevation threshold and when the absolute roll or pitch of the aircraft exceeded 5°. In addition, we regarded snow depths larger than 1.5 m as outliers and discarded them from further analysis.

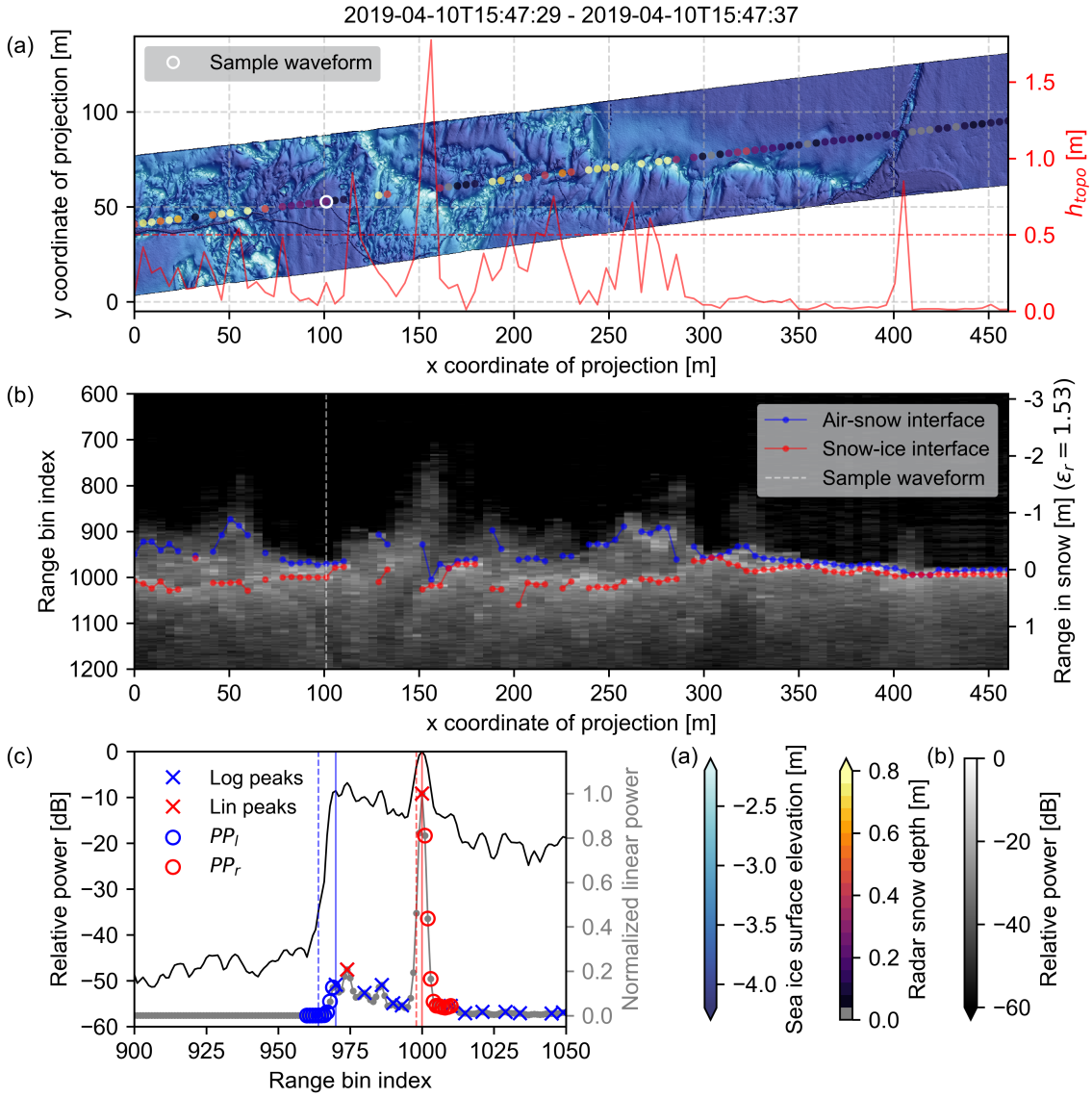

Figure 4.4. Example from the low-altitude survey flight 20190410_01 at approximately 71.36°N, −131.15°E. (a) Snow Radar derived snow depth estimates with the peakiness method (colored dots, footprint diameter has been exaggerated by a factor of 2) overlaid on ALS-derived WGS84 surface elevation (bluish swath). The red solid line is the corresponding along-track topographic variability (h_{topo}), and the dashed line is its 0.5-m threshold (right-hand side vertical axis). (b) Corresponding section of the Snow Radar echogram with air–snow (blue) and snow–ice (red) interfaces identified with the peakiness method. (c) Sample waveform [white circle in (a) and white dashed line in (b)] in logarithmic scale (black) and in linear scale (gray, right-hand side vertical axis) together with the air–snow (blue) and snow–ice (red) interfaces identified using the peakiness (solid line) and Haar wavelet (dashed line) methods. The blue (red) crosses and circles illustrate the left-hand (right-hand) peakiness calculation.

4.2.5 Auxiliary Sea Ice Data

To assist in the analysis and evaluate the results, we connected the snow depth estimates with coinciding multiyear ice fraction (MYIf) information using the 12.5-km resolution MYI concentration product from the University of Bremen (Ye et al., 2016a,b).

4.3 Results

4.3.1 Calibration

Fig. 4.5 shows how the radar data improved during the calibration process through coherent noise removal and system response deconvolution, which take place between the figure panels. Due to the lack of open water leads during some survey flights, not all segments could be deconvolved using specular targets from the same flight. However, in those cases, we used a deconvolution waveform from another segment with the same survey altitude, which may lead to reduced deconvolution quality due to drifts in the system response over time. Fig 4.6 shows the system impulse deconvolution for the flight segments on April 10, 2019, which crossed several leads. The reduction in bandwidth from 2–18 to 4–11.5 GHz during deconvolution [see Fig. 4.6 (Right)] prohibited amplifying high-frequency noise but caused an increase in the range resolution, which was evident also in the 3-dB range resolution that had a value of approximately 4.2 cm after deconvolution. While the deconvolution did not sharpen the main lobe significantly, the side lobes were suppressed to about −30 dB or less [see Fig. 4.6 (Left)].

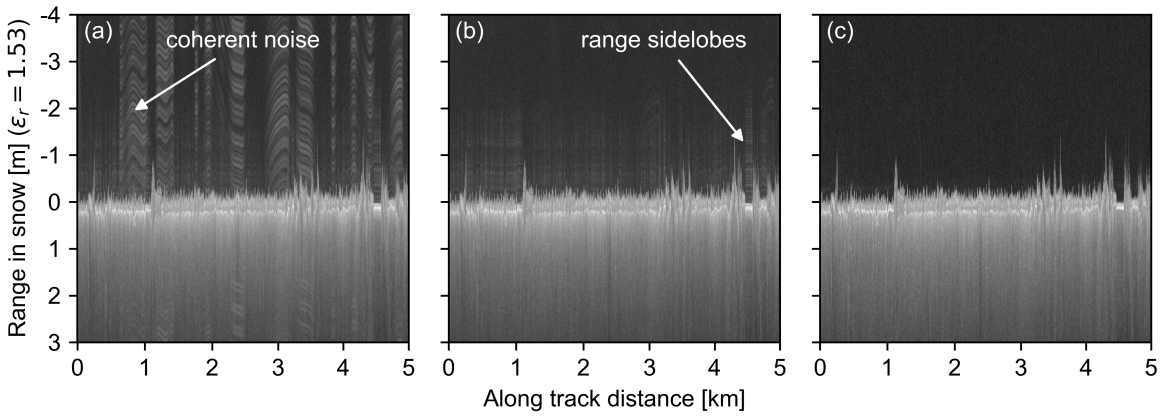

Figure 4.5. Example frame of the low survey altitude AWI Snow Radar data during different steps of the calibration process (a) before coherent noise removal, (b) after coherent noise removal, and (c) after system response deconvolution. Brighter colors indicate higher return power of the radar signal. The range axis is calculated assuming a snow density of 0.3 g · cm^{-3}.

To further investigate the effect of the system response deconvolution, we considered the system sidelobe strength dependence for our data both before and after deconvolution following Kwok and Maksym (2014), Kwok and Haas (2015), and Kwok et al. (2017). While they calculated the curves for the whole campaign (over 10^6 waveforms), we restricted our analysis to individual flight segments due to the differing survey altitudes, thus limiting the total number of waveforms (in the order of 10^4) in the resulting group of curves. The curves in Fig. 4.7 show radar returns that were oversampled by a factor of 16, averaged with a rolling window of the same size, and normalized with respect to the peak (maximum) return, $\tilde{s}(i) = s(i)/s_{\text{peak}}$. We averaged them over 2-dB intervals of the peak signal-to-noise ratio, PSNR =

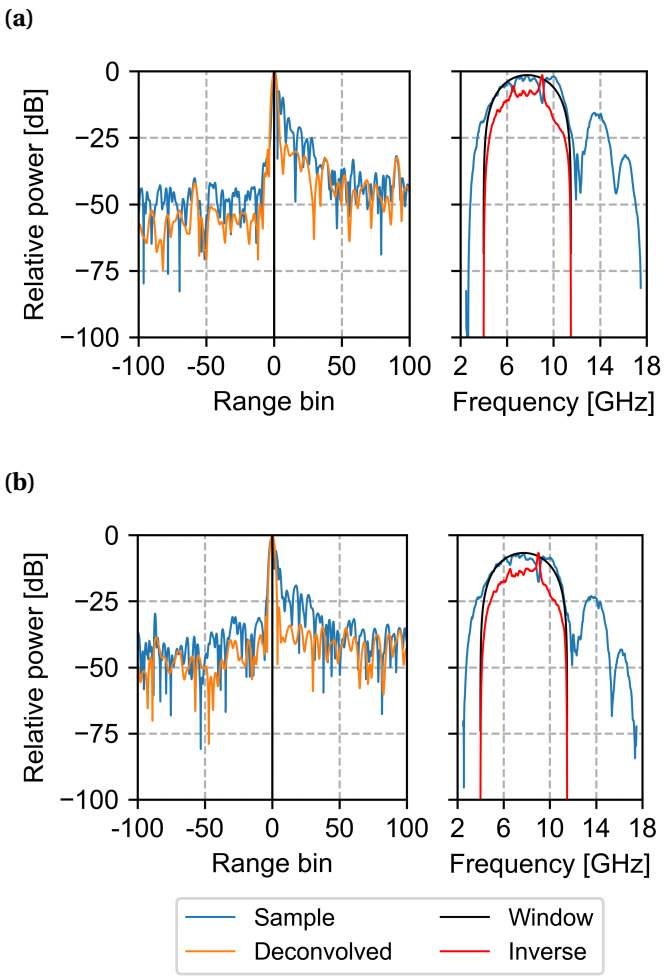

Figure 4.6. (Left) Deconvolution waveforms and (Right) transfer functions for flight segments (a) 20190410_01 (low altitude) and (b) 20190410_02 (high altitude). The positive range axis is away from the radar.

$s_{\text{peak}}/\bar{n}$, where $\bar{n}$ is the noise calculated from the first 100 range bins of the waveform. The figure shows the desired effect of reduced side lobes after deconvolution and also generally higher SNR levels with lower altitude and for deconvolved data.

4.3.2 Validation

The last flight of the 2017 campaign on April 10 took place over a site with high-resolution and 2-D *in situ* snow measurements in the Elson Lagoon close to Point Barrow, Alaska. The ground-truth snow depth data were collected in a 650 × 450-m area surveyed using a terrestrial laser scanner (TLS) to establish snow surface position relative to an array of 15 reference reflectors frozen to the ice on level landfast FYI on March 30–April 1, 2017. Snow depth was determined from the surface position by subtracting an ice surface that was presumed to be planar. The planar ice surface assumption, in this case, is well supported by scans of the snow-free ice surface in autumn, which showed less than 2 cm of surface height variation, a lack of vertical deformation in the reference reflector array during the course of the winter, and cross comparison of the derived snow depths with probe-based measurements. The horizontal resolution of the resulting TLS field was 25 cm, and the vertical accuracy was determined to be approximately 1 cm by cross-comparison with manually measured snow

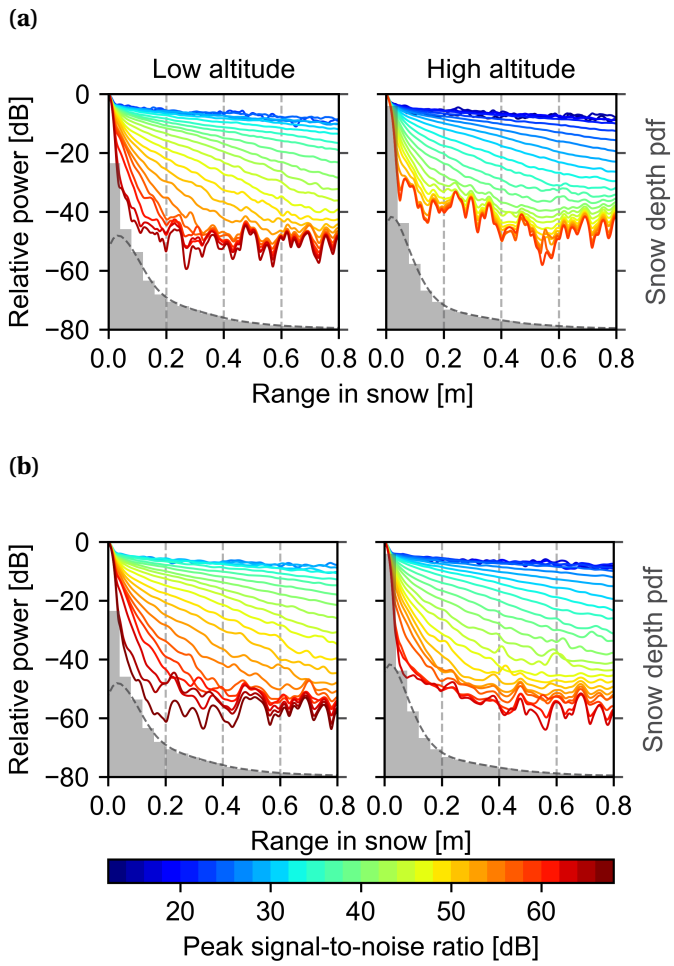

Figure 4.7. Investigating system side lobes (a) before and (b) after the system response deconvolution for flight segments 20190410_01 (low altitude, left) and 20190410_02 (high altitude, right). Gray histograms show the probability density functions (pdf) of the snow depth estimates retrieved with the peakiness method with a bin size of 4 cm (right-hand side vertical axis). The range in snow is calculated assuming a snow density of 0.3 $g \cdot cm^{-3}$.

depths collected with automatic snow depth probes (magnaprobe) within the survey area. The snow depth in the entire area ranged from 1 to 71 cm with a mean value of 23 cm and a standard deviation of 6 cm. There was no precipitation and very little redistribution between the TLS and Snow Radar surveys. Prevailing winds from east-northeast affected the morphology of the dunes [see Fig. 4.8(i)].

We surveyed the field site with the aircraft at the low survey altitude mode (200 ft) in three different directions: 1) from southeast to northwest; 2) from southwest to northeast; and 3) from north to south (see Fig. 4.8). For each radar return, we calculated the snow depth estimate using a snow density of 0.3 $g \cdot cm^{-3}$ derived from four snow pit profiles, which agreed also with the climatological value (Warren et al., 1999). We determined the corresponding TLS snow depth as the mean value within a radius that we assumed to equal the theoretical smooth surface and cross-track radar footprint radius. To evaluate the validation, we calculated root mean square errors (RMSEs), mean biases, and correlation coefficients (r) for each crossing flight line separately and all overlapping points together.

The validation results from the TLS comparison with the peakiness method are shown in Fig. 4.8 and Table 4.4. Bias in the comparison was minimized with peak detection power thresholds of 0.7 and 0.2 to detect the air–snow and snow–ice interfaces, respectively, and setting the threshold value to 20 for both peakiness parameters (see Table 4.3), which re-

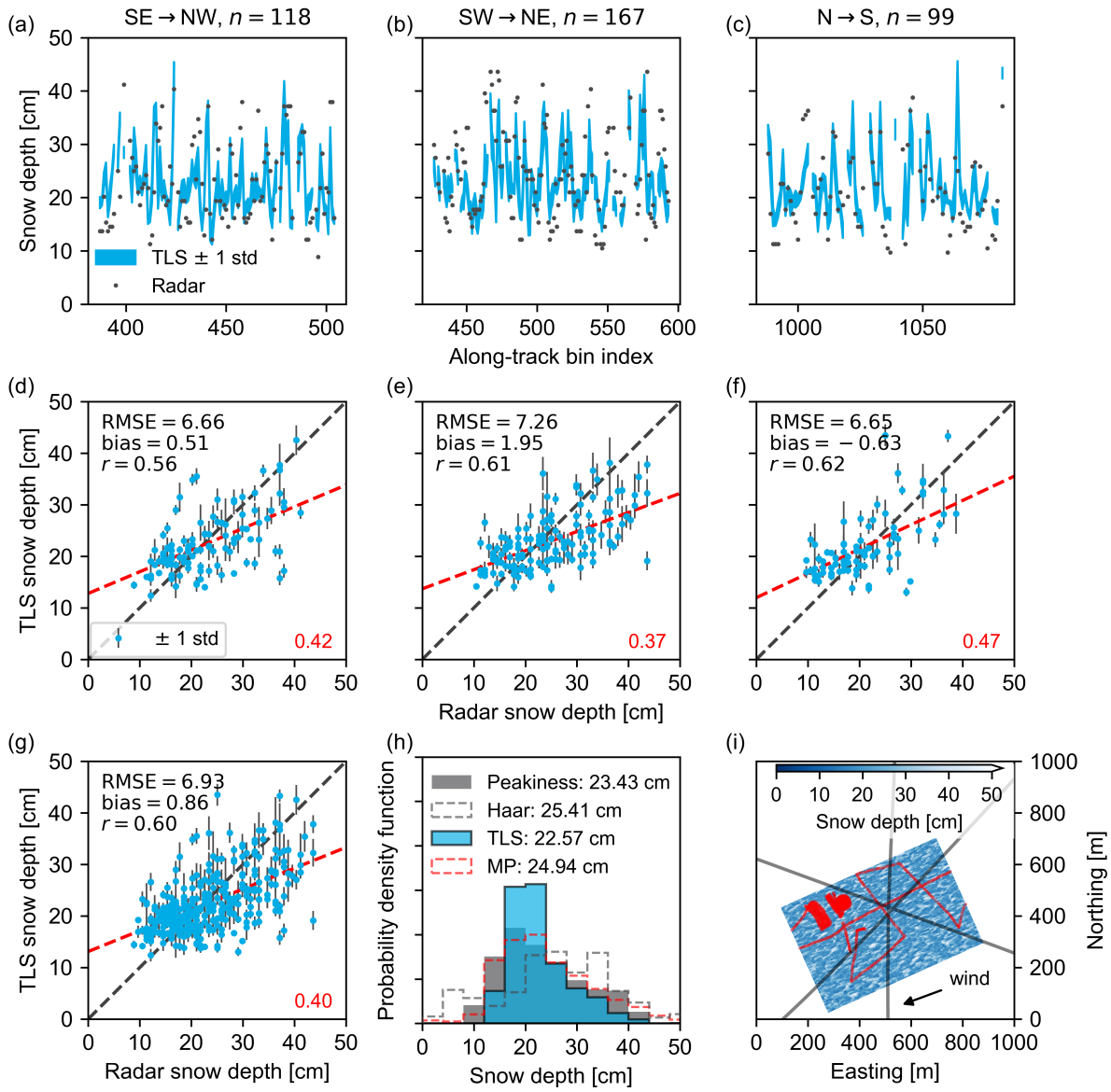

Figure 4.8. Validation over the TLS snow depth field in Utqiagvik (Barrow) on April 10, 2017. The three columns are the flight paths crossing the field in three different directions: 1) from southeast (SE) to northwest (NW); 2) from southwest (SW) to northeast (NE); and 3) from north (N) to south (S). (a)–(c) Along-track snow depth estimates derived from the radar and TLS data, whereas (d)–(f) show them as scatter plots with the calculated statistics in addition to the first-order least-squares fit lines and their respective slopes in red. (g) All overlapping snow depth estimates together ($n = 384$) as a scatter plot and (h) their probability density functions using a bin width of 4 cm. For comparison, the snow depth distributions using the Haar wavelet method (gray dashed) and magnaprobe (MP, red dashed) are shown. The values in the figure legend correspond to the mean snow depths. (i) Overview of the validation site: the snow depth is shown with a range of bluish colors, the crossing flight tracks as black lines, and the magnaprobe measurements in red. The arrow shows the prevailing wind direction from east-northeast. The origin is at 4W 590250 7917600 in UTM coordinates.

tained 90% of the collected waveforms. Line 1 had the lowest correlation coefficient of 0.56, the shared-lowest RMSE of 6.66 cm, and a mean bias of 0.51 cm. Line 2 ran against the dominant orientation of the snow dunes and had the most values for comparison across the validation field. However, the results showed the largest values for RMSE and mean bias of 7.26

	Radar: Peakiness	TLS
Line 1	23.0 ± 7.9 (19) cm	22.4 ± 5.9 (21) cm
Line 2	24.9 ± 8.9 (19) cm	22.9 ± 5.3 (22) cm
Line 3	21.5 ± 8.4 (17) cm	22.1 ± 6.3 (17) cm
All	23.4 ± 8.5 (19) cm	22.6 ± 5.8 (22) cm

Table 4.4. Mean ± standard deviation (mode) of the peakiness method and the terrestrial laser scanner (TLS) derived snow depth estimates in centimeters for the validation Site (see Fig. 4.8)

and 1.95 cm, respectively. Line 3 revealed a slightly negative bias (−0.63 cm), the best correlation coefficient out of the three crossing lines (0.62), and shared-lowest RMSE (6.65 cm). Considering all overlapping radar and TLS snow depth estimates together, we found a correlation coefficient of 0.60, an RMSE of 6.93 cm, and a mean bias of 0.86 cm, which was still well within the assumed TLS accuracy of 1 cm. The peakiness method well captures the snow depth distribution indicated by both the TLS and magnaprobe [see Fig. 4.8(h)].

On average, the validation of snow data picked with the Haar wavelet method showed worse results compared to the new picker method, despite retaining all waveforms, resulting in a correlation of 0.42 (ranging from 0.36 to 0.51 between the crossing lines), a mean bias of 2.57 cm (1.62–4.59 cm), and an RMSE of 10.26 cm (9.57–10.90 cm). The Haar wavelet method overestimated the mean snow depth by approximately 10% [see Fig. 4.8(h)].

We estimate the uncertainty by following the approach of Newman et al. (2014) where the mean bias between the Snow Radar (SR) and TLS snow depths ($\delta_{\mathrm{SR-TLS}}$), the precision of the radar snow depths ($\varepsilon_{\mathrm{SR}}$), and the precision of the TLS snow depths ($\varepsilon_{\mathrm{TLS}}$) are added in quadrature:

$$\sigma_{SR}^2 = \delta_{\mathrm{SR-TLS}}^2 + \varepsilon_{\mathrm{SR}}^2 + \varepsilon_{\mathrm{TLS}}^2. \tag{4.10}$$

Taking the 3-dB range resolution of 4.2 cm as the Snow Radar precision, the uncertainty results in σ_{SR} = 4.4 cm (18% of the overall snow depth). This uncertainty value is lower than the simplistic error estimate of 5.7 cm in Kurtz et al. (2013) still being used for the current OIB snow depth on sea ice products (Kurtz et al., 2015; NSIDC, 2016).

To this date, no further colocated AWI Snow Radar data and ground-truth measurements were available to us, neither were there flight tracks with colocated AWI and OIB Snow Radar data.

4.3.3 Intercomparison at Different Altitudes

Because of the differences in the nominal along-track spacing of the AWI Snow Radar data points between the two survey altitudes, the total number of high-altitude waveforms was 59% and 57% of the low-altitude waveforms for April 2 and 10, 2019, respectively. Therefore, we present the snow depth estimates averaged to 40-m and 1-km along-track bins. In Table 4.5, the percentages show the fraction of valid waveforms after postprocessing (see Section 4.2.4.3) included in averaging. Due to the filtering according to the user-defined waveform parameter thresholds, the percentages for the peakiness method were consistently smaller than for the Haar wavelet method. In addition, due to the data gaps that

Table 4.5. Total along-track distance (km), mode (m), mean (m), standard deviation (m), fraction of valid postprocessed waveforms (wfs) included in averaging, and number of valid 40-m averaged AWI Snow Radar snow depth estimates for the two algorithms and for the low and high survey altitude flight segments on April 2 and 10, 2019

Flight ID	Altitude	Distance	Peakiness					Haar wavelet				
			mode	mean	std	wfs	n	mode	mean	std	wfs	n
20190402_01	low	304	0.44	0.44	0.26	49%	3480	0.23	0.43	0.25	86%	3688
20190402_02	high	305	0.52	0.44	0.26	68%	3239	0.61	0.48	0.25	76%	3361
20190410_01	low	444	0.00	0.19	0.19	79%	7318	0.05	0.25	0.20	93%	7271
20190410_02	high	385	0.00	0.16	0.18	84%	7272	0.12	0.22	0.18	87%	7304

resulted from the EM-Bird calibration maneuvers, we limited the snow depth comparison to those sections where estimates from both altitudes were available. We did not apply any drift correction nor adjust the flight track of the return segment.

4.3.3.1 MYI

The flight on April 2, 2019, departed from Eureka along the Nansen Sound and out to the Arctic Ocean at the low survey altitude and returned at the high survey altitude [see Fig. 4.9(a)]. It was characterized by FYI in the Nansen Sound until a stretch of landfast MYI (a "plug") several tens of kilometers in length right at the mouth of the sound, which is shown with a black circle in Fig. 4.9(a) around −92°E. After a short decrease in MYIf down to 40%, major parts of the segments were dominated by MYI only. The sea-ice drift of the surveyed area in the Arctic Ocean during that day was marginal, less than about 1.2 $\mathrm{cm} \cdot \mathrm{s}^{-1}$ toward the south. Due to more turbulent conditions at the low survey altitude, we did not attempt to keep the exact overlap between the segment flight tracks. During the flight, the distance between the two segments was within 730 m with a mean of 250 m.

The retrieved snow depth distributions were mostly bimodal due to the continuously thick snow cover of around 0.5–0.6 m over the MYI plug; however, the bimodality was less clear in the low-altitude data and even absent in the corresponding Haar wavelet distribution [see Fig. 4.9(b)–(e)]. The mean snow depth (0.44 m) and standard deviation (0.26 m) using the peakiness method were consistent between the two survey altitudes, whereas the mean difference in snow depth of 0.06 m between the altitudes over the MYI plug mainly contributed to the differing modal values (see Table 4.5). In comparison, the Haar wavelet method returned larger values for the mean and modal snow depth at the high survey altitude. For the low altitude, the mean snow depth and standard deviation were similar (0.43 and 0.25 m), but the missing second peak in the distribution resulted in a modal value of only 0.23 m.

Fig. 4.9(f) and (g) shows the snow depth estimate profiles derived using the peakiness method in 40-m and 1-km bins at the two survey altitudes. The 1-km averaged profiles follow each other reasonably well considering that the flight tracks did not match exactly and no ice drift correction was done [see Fig. 4.9(h)]. However, we found a discrepancy over the MYI plug around −92°E. The 40-m binned snow depth estimates from the two survey altitudes showed the maximum correlation of 0.58 when the distance between the segments was up to 30 m and decreased to 0.2 and below when distance exceeded 300 m, and more values were included in the analysis. Similarly, RMSE was 0.14 m at small distances and slowly increased to 0.3 m for distances larger than 500 m. A small negative bias of the low-altitude snow depth estimates, up to −0.1 m due to the difference over the MYI plug, eventually balanced out to near zero as the distance increased.

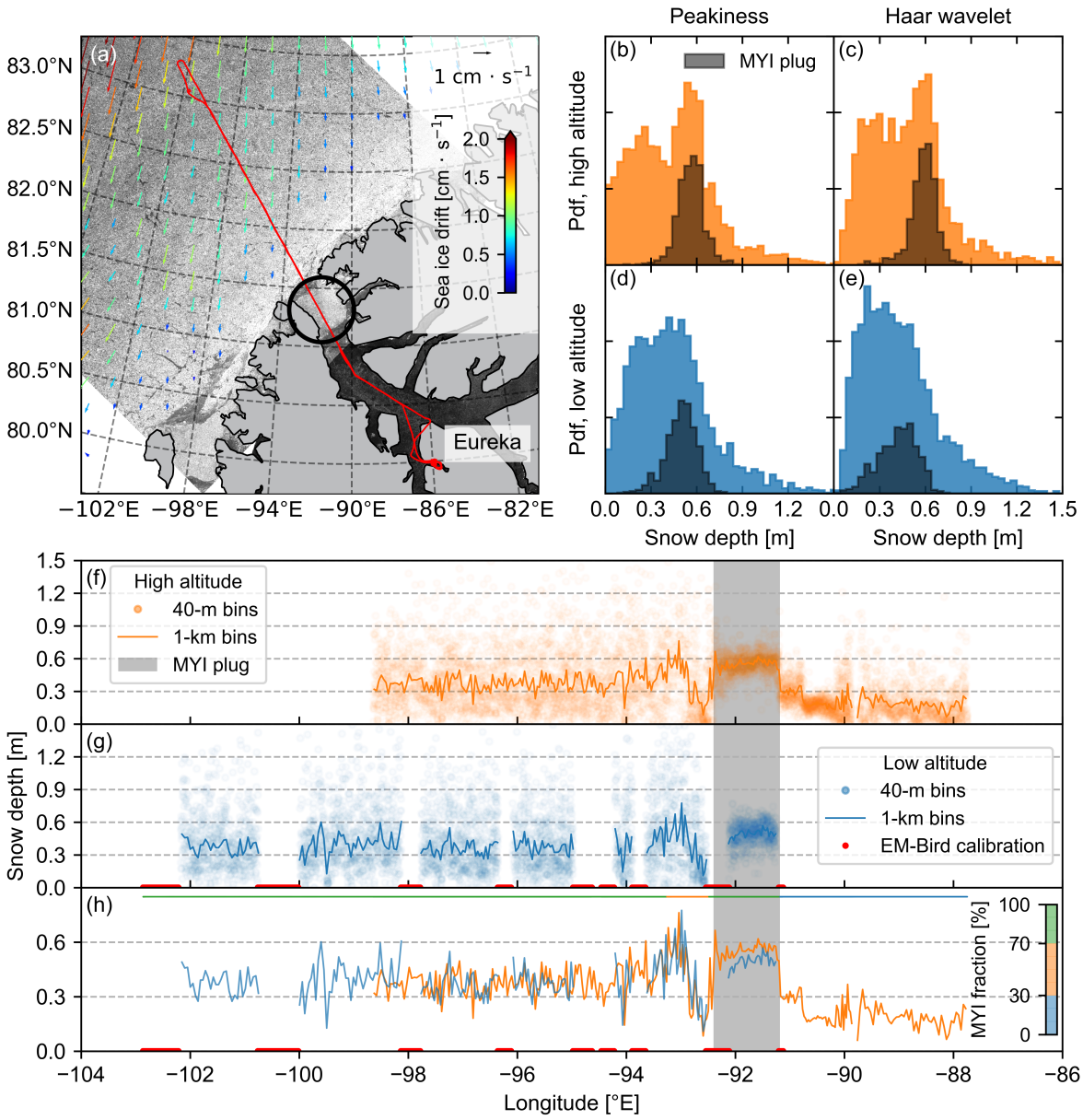

Figure 4.9. Snow depth estimates over the Nansen Sound and the Arctic Ocean on April 2, 2019. (a) Flight track (red line) and Polar Pathfinder daily 25-km EASE-grid sea ice motion vectors (Tschudi et al., 2019a) (colored arrows) overlaid on Sentinel-1 Level-1 extra-wide (EW) swath ground range detected (GRD) HH-polarized SAR images acquired on the day of the survey. Brighter colors indicate higher backscatter, i.e., rougher (older) sea ice. The black circle shows the location of the MYI plug at the mouth of the Nansen Sound. Copernicus Sentinel data 2019. (b) pdf of the 40-m averaged snow depth from the high-altitude segment using the peakiness method. The gray histogram shows the snow depth distribution over the MYI plug. (c) 40-m averaged snow depth pdf from the high-altitude segment using the Haar wavelet method. (d) and (e) Same as (b) and (c) but for the low-altitude segment. The bin width in the pdfs (b)–(e) is 4 cm. Basic statistics are given in Table 4.5. (f) Along-track snow depth profile in 40-m (dots) and 1-km (line) bins using the peakiness method (the Haar wavelet method not shown) for the high-altitude segment against longitude. The gray section indicates the location of the MYI plug. (g) Same as (f) but for the low-altitude segment together with EM-Bird calibration maneuvers (red). (h) 1-km bin along-track profiles of the two segments combined together with MYIf classification.

4.3.3.2 Mixed Ice Types

The flight on April 10, 2019, followed a ground track of the ICESat-2 satellite, namely, the ground track of the strong center beam of orbit number 189 of cycle 3, out to the East Beaufort Sea (Hendricks et al., 2019) [see Fig. 4.10(a)]. The flight path crossed several leads and varying types of ice: young and older FYI near the coast but also embedded in the MYI zone north of 71.75°N. Similar to the flight on April 2, we did the outbound survey at low altitude and returned at the high survey altitude. However, in more challenging flight conditions due to higher wind speeds, the maximum distance between the segments was 1.8 km and the average 460 m. Sea-ice drift velocity in this area on the day of the survey was up to one order of magnitude larger, around 10 $\mathrm{cm} \cdot \mathrm{s}^{-1}$ with direction varying from south to southwest, moving the ice as much as 1.3 km during the 4-h survey.

Table 4.5 shows that the snow depth estimates at the low survey altitude were on average 0.03 m larger than at the high altitude. The same was true comparing the two retrieval methods, where the Haar wavelet method resulted in 0.06 m deeper mean snow depth estimates than the peakiness method. The shapes of the distributions were similar, but the snow depths derived with the Haar wavelet included significantly less thin (<0.04 m) snow [see Fig. 4.10(b)–(e)], which was reflected also in the modal values.

The snow depth estimates derived using the peakiness method in 40-m and 1-km bins at the two survey altitudes are shown in Fig. 4.10(f) and (g). The 1-km averaged profiles captured the main features across the different ice types [see Fig. 4.10(h)]. However, compared to the profiles from April 2, snow depth estimates from the two survey altitudes differed more frequently, i.e., low-altitude estimates exceeded the ones acquired from the high-altitude segment. This was because the radar measured inherently different snow due to the sea-ice drift between the overpasses as a function of temporal and spatial separations between the flight track segments over heterogeneous sea-ice conditions. The 40-m binned snow depth estimates from the two survey altitudes showed the maximum correlation of 0.40 when the distance between the low- and high-altitude segments was less than 40 m and decreased to 0.2 and below when including values that were separated by more than 620 m. Similarly, RMSE was 0.2 m at small distances and increased to 0.23 m for distances larger than 600 m. A small positive bias of 0.06 m of the low-altitude snow depth estimates was eventually halved to 0.03 m as the distance increased.

4.4 Discussion

We have demonstrated the feasibility of sensor calibration for the AWI Snow Radar at the unprecedented low altitude of 200 ft, which included coherent noise removal and system response deconvolution using the cresis-toolbox (see Figs. 4.5–4.7). Previously, Yan et al. (2017b) showed the effect of coherent noise removal and system response deconvolution at the nominal 1500-ft survey altitude and found an improvement of 0.24 cm in the 3-dB range resolution. However, we did not find such an effect on our deconvolved sample data on ei-

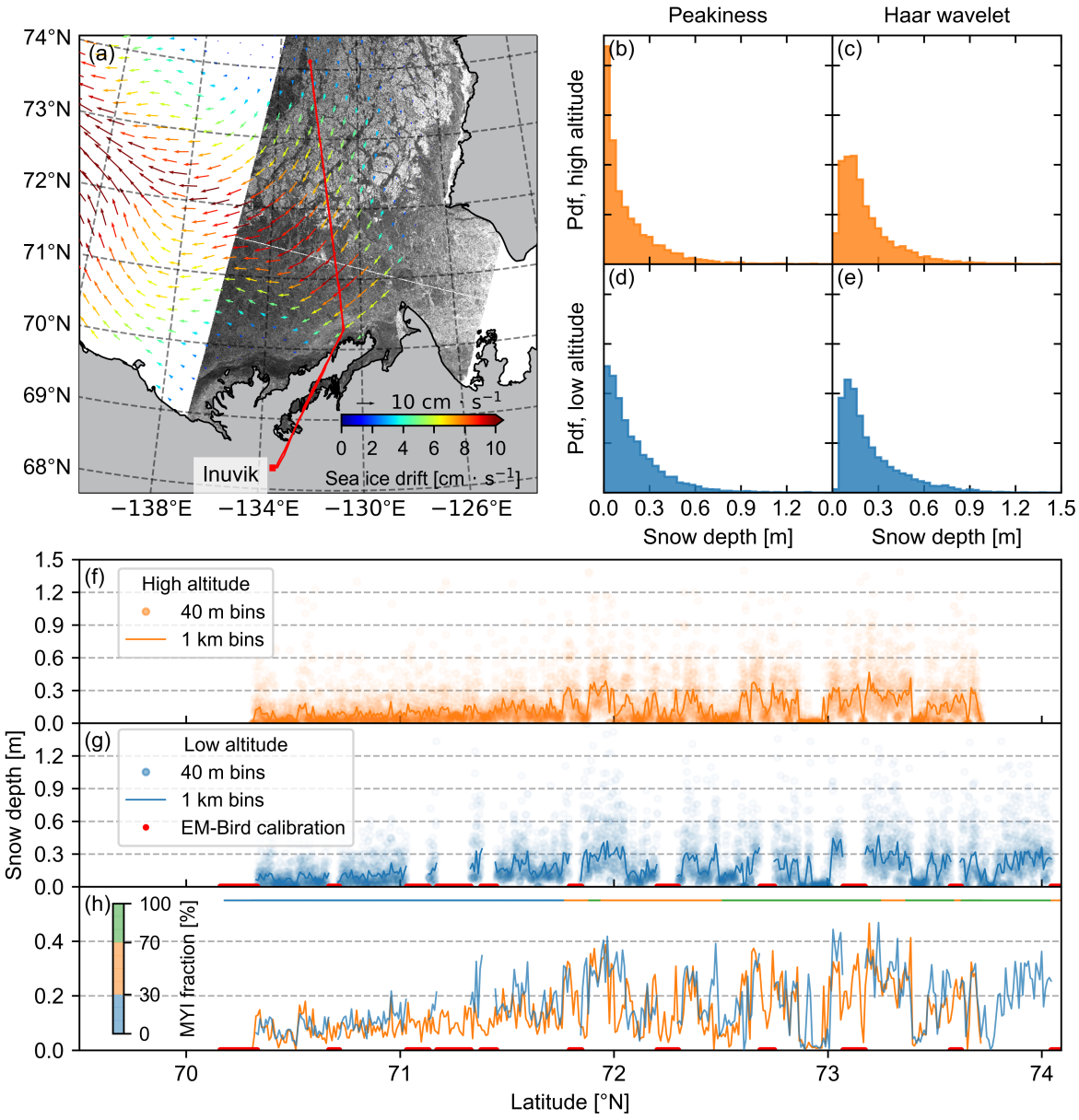

Figure 4.10. Snow depth estimates over the East Beaufort Sea on April 10, 2019. For description, see the caption of Fig. 4.9. Note the different scales of the sea-ice drift in (a) and the different horizontal axes in (f)–(h). Basic statistics are given in Table 4.5.

ther survey altitude. Moreover, they did not report any reduction in bandwidth that we were obliged to do to avoid amplifying high-frequency noise. We also think that the specularity of the sea-ice leads that we used as targets might have been compromised due to windy conditions and insufficient size. Using a man-made calibration target, for example, a corner reflector, as suggested in Yan et al. (2017b), would be a solution but logistically challenging. Future calibration steps include SAR-focused and array processing, which may further improve the radar data quality.

For the validation of our novel peakiness-based retrieval method, we compared the snow depth estimates derived from the AWI Snow Radar measurements at low survey altitude

against 2-D *in situ* snow depth measurements from a TLS. Mean values of 23.43 and 22.57 cm revealed an excellent agreement. The resulting slightly positive mean bias of 0.86 cm was well within the accuracy of the TLS snow depths and below radar sensor resolution. However, there were two main shortcomings to this validation. First, the range of TLS snow depths was narrow, only 31 cm. This lack of range likely reduced the obtained correlation between the data sets. For a more comprehensive validation, *in situ* snow depths with higher spatial variability are required. Second, the validation was limited to level landfast FYI, low survey altitude, and one season only. Due to weather constraints, further validation opportunities against *in situ* measurements on other ice types are not available to this date. For this reason, we chose to follow the approach of Newman et al. (2014) and use the nonparametric surface topography estimate h_{topo} to filter out potentially false snow depth estimates where the sea-ice surface was deformed.

We found that the new peakiness method worked better for the AWI 2–18-GHz radar version and low survey altitude than the Haar wavelet method. Although the retrieved snow depth estimates indicated similar statistics (see Table 4.5 and Figs. 4.9 and 4.10), the Haar wavelet method led to overestimation and underestimation of snow depth. As we showed in the validation (see Section 4.3.2, Fig. 4.8) and further illustrated in Fig. 4.4(c), the Haar wavelet method overestimated the mean snow depth in a regular case where the snow–ice interface had the largest return power. This was caused by the assumption of the method to assign the air–snow interface to the first range bin on the leading edge of the waveform that was above the noise floor, i.e., when the radar pulse began to illuminate the interface. This reflection could originate from the top of a sea-ice surface feature, such as a snow dune or a pressure ridge, and even from off-nadir (Newman et al., 2014). Therefore, the resulting snow depth estimate would correspond more to the maximum snow depth within the radar footprint rather than to the average. However, studies have shown that the air–snow interface may also be the dominant scattering surface in certain conditions and within the frequency range of the Snow Radar (Kanagaratnam et al., 2007; Willatt et al., 2010, 2011). Consequently, the assumption of the Haar wavelet method to consider only points on the leading edge of the waveform (Newman et al., 2014) could lead to drastic underestimation of the snow depth when the maximum return power was associated already with the air–snow interface, while the signal from the assumed snow–ice interface was less powerful. The newly developed approach with peakiness parameters has been specifically designed to picking correct interfaces also in such cases.

By design, the Haar wavelet method will not derive a zero snow depth as it considers two points on the leading edge of the waveform. Because we did not use any lead detection for filtering, in particular, the snow depth estimates derived with the Haar wavelet method on April 10, 2019, might be biased high. We also did not assign any limit, such as the theoretical or a multiple of the 3-dB range resolution (Kwok et al., 2011; Newman et al., 2014), for the minimum detectable snow depth to include the physical result of zero snow depth and to avoid biasing by excluding thin snow.

We acknowledge that the use of several user-definable peak detection parameter thresholds in the new peakiness method may introduce additional uncertainties and would ideally require validation in each season to constrain them properly. Our method decreases the sensitivity to the sea-ice surface features and the leading edge of the waveform compared to the Haar wavelet method, therefore bringing the derived snow depth estimates closer to the average value rather than the maximum. Increasing (decreasing) the peak detection threshold for the logarithmic power would decrease (increase) the snow depth as the air–snow interface is moved up (down) the leading edge of the waveforms. Varying the peak detection threshold for the linear-scaled power could allow more possible snow–ice interfaces to be detected especially when the air–snow interface is the dominant scatterer but, at the same time, risks increasing the number of ambiguous waveforms. We think it would be worthwhile to further investigate if the parameter thresholds could be expressed as functions of surface roughness using data from the ALS. For example, the observed discrepancy in the snow depth estimates over the MYI plug [see Fig. 4.9(h)] indicates that assigning the thresholds for the peakiness method parameters dynamically based on ice type and radar footprint size rather than choosing constant values for each segment could improve the accuracy of the snow depth estimates. In addition, the detection of the air–snow interface could be improved by aligning the Snow Radar and ALS snow freeboard measurements, such as the approach of Kwok et al. (2011).

It is challenging to conclusively compare the overlapping flight segments with only centimeter-scale differences in the statistical values of the snow depth estimates without validation data on the ground. Considering the sea-ice drift, especially its cross-track component present during both flights [see Figs. 4.9(a) and 4.10(a)], and the distance between the segment flight paths, we think a direct comparison between flight segments is problematic.

In this article, we have demonstrated the viability of the AWI Snow Radar calibration and processing chains and that they are consistent with existing survey configurations. Together with the small radar footprint size, the high-resolution ALS data, and the new peakiness retrieval method, we are confident that the snow depth estimates presented here are of sufficient accuracy to derive snow depth on a regional scale for sea-ice mass balance and long-term monitoring.

4.5 Conclusion

Taking advantage of the slow speed and low altitude of the airborne AWI IceBird sea-ice surveys, we are able to measure sea ice with high spatial resolution. The quadpolarized 2–18-GHz FMCW microwave radar developed by CReSIS accurately measures snow depth on sea ice, and we have demonstrated that our new snow depth retrieval algorithm based on a signal peakiness parameter is capable to provide precise estimates of snow depth over different ice types and survey altitudes, even when the air–snow interface is the dominant scattering surface. The small radar footprint size at the low survey altitude of 200 ft enhances the

spatial resolution and decreases the effect of off-nadir sea-ice surface features compared to acquisitions at higher altitudes. The validation of low-altitude AWI Snow Radar data against a high-resolution 2-D TLS field, which resolves the snow depth distribution within the radar footprint but is restricted to level landfast FYI, is unique and yields a mean bias lower than the radar resolution. However, colocated Snow Radar and 2-D ground-truth surveys over different ice types are required to reduce the uncertainty of snow depth estimates in a deformed sea-ice environment. Comparison between the low and high survey altitudes of overlapping segments shows good consistency in the snow depth estimates derived with the peakiness method and, thus, data from the OIB program.

With the demonstrated capabilities of the AWI Snow Radar, we can now take advantage of the combined data sets of snow depth from the radar, snow surface freeboard from the ALS, and the total ice thickness from the EM-Bird. Linking them will enable us to describe the whole sea-ice layer on a regional scale as part of the long-term AWI IceBird program. Such information will be vital to facilitate studies of, for example, basin-scale snow depth and ice thickness assessment from dual-altimetry products in the era of CryoSat-2 and ICESat-2.

Acknowledgment

The authors acknowledge the use of the CReSIS toolbox from CReSIS generated with support from the University of Kansas. Wavelet-based retrievals described in this work were originally developed by the NOAA Laboratory for Satellite Altimetery and have been adapted for use in pySnowRadar. They thank Kenn Borek Air, AWI technicians and logistics, Environment and Climate Change Canada (ECCC), and Canadian Forces Station (CFS) Alert, who helped at various stages of the data collection.

Funding information

The authors acknowledge support by the Open Access Publication Funds of Alfred-Wegener-Institut Helmholtz-Zentrum für Polar- und Meeresforschung. The CReSIS toolbox used in this work was generated with support from the University of Kansas, NASA Operation IceBridge grant NNX16AH54G, and NSF grants ACI-1443054, OPP-1739003, and IIS-1838230. Development and aircraft integration of the AWI Snow Radar system was made possible with support from Bundesministeriums für Bildung und Forschung (BMBF) grant 03F0700A. The work of Arttu Jutila was supported by the Helmholtz Graduate School for Polar and Marine Research (POLMAR) Short-Term Research Grant for visiting the ECCC Climate Processes Section in Toronto, ON, Canada. The work of Chris Polashenski was supported by the U.S. National Science Foundation under Grant ARC-1603361.

Author biographies

Arttu Jutila was born in Inari, Finland, in 1992. He received the B.Sc. and M.Sc. degrees in hydrospheric geophysics from the University of Helsinki, Helsinki, Finland, in 2014 and 2017, respectively. He is pursuing the Dr. rer. nat. degree with the Alfred Wegener Institute, Helmholtz Centre for Polar and Marine Research, Bremerhaven, Germany.

In 2018, he joined the Alfred Wegener Institute, Helmholtz Centre for Polar and Marine Research. His research interests include snow on sea ice, microwave radar remote sensing, and sea-ice mass balance.

Mr. Jutila is a Junior Member of the International Glaciological Society (IGS).

Joshua King received the M.Sc. and Ph.D. degrees from the University of Waterloo, Waterloo, ON, Canada, in 2009 and 2014, respectively.

He is a Research Scientist with the Climate Research Division, Environment and Climate Change Canada, Toronto, ON. His research interest includes the development of field and remote sensing methods for the characterization of snow properties on land and sea ice.

John Paden (Senior Member, IEEE) received the M.Sc. and Ph.D. degrees in electrical engineering from the University of Kansas (KU), Lawrence, KS, USA, in 2003 and 2006, respectively, studying radar signal and data processing for remote sensing of the cryosphere.

After graduating, he joined Vexcel Corporation, Boulder, CO, USA, a remote sensing company, where he worked as a Systems Engineer and an SAR Engineer for three and a half years before rejoining the Center for Remote Sensing of Ice Sheets (CReSIS), KU, in early 2010 to lead the radar signal and data processing efforts. He is a Research Faculty Member at CReSIS with a courtesy appointment in the Electrical Engineering and Computer Science Department.

Dr. Paden was awarded the American Geophysical Union Cryosphere Early Career Award in 2016. He has also received three NASA group achievement awards for radioglaciology work.

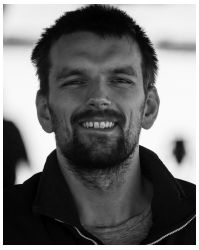

Robert Ricker received the Ph.D. degree from Jacobs University Bremen, Bremen, Germany, in 2015.

He continued his work as a Post-Doctoral Research Fellow at the Institut français de recherche pour l'exploitation de la mer (IFREMER), Brest, France. He is with the Alfred Wegener Institute, Helmholtz Centre for Polar and Marine Research, Bremerhaven. His research interest includes the remote sensing of polar regions.

Stefan Hendricks received the Ph.D. degree from the University of Bremen, Bremen, Germany, in 2009.

Besides the Ph.D. program, he has worked as a Project Scientist and nowadays as a Senior Scientist at the Sea Ice Physics Section of the Alfred Wegener Institute, Helmholtz Centre for Polar and Marine Research, Bremerhaven. His research focus is the observation of global sea-ice thickness with geophysical methods and satellite remote sensing.

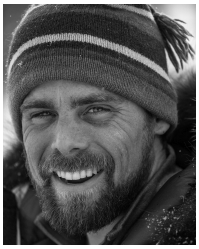

Chris Polashenski received the Ph.D. degree from the Thayer School of Engineering, Dartmouth College, Hanover, NH, USA, in 2007.

He is with the U.S. Army Cold Regions Research and Engineering Laboratory, Fairbanks, AK, USA, and holds an adjunct appointment as an Associate Professor at the Dartmouth College. He is the author of several publications on sea-ice properties and processes, snow deposition and redistribution, and the albedo of sea ice and ice sheets. His research interests involve both remote sensing and detailed *in situ* field study of cryospheric processes.

Dr. Polashenski is a member of the American Geophysical Union, the International Glaciological Society, and the Association of Polar Early Career Scientists.

Veit Helm received the Ph.D. degree from the University of Bremen, Bremen, Germany, in 2008.

He works as a Senior Scientist in the Glaciology Group, Alfred Wegener Institute, Helmholtz Centre for Polar and Marine Research, Bremerhaven. His research interest includes the observation of polar regions using ground-based, airborne, and satellite remote sensing with the main focus in the processing of radar and laser data of various sensors.

Tobias Binder received the Ph.D. degree from the University of Heidelberg, Heidelberg, Germany, in 2014.

He supported the University of Kansas, Lawrence, KS, USA, to deploy the ultrawideband microwave radar aboard the AWI polar research aircraft. He was with the Alfred Wegener Institute, Helmholtz Centre for Polar and Marine Research, Bremerhaven, Germany, from 2014 to 2018. He is with Ibeo Automotive Systems GmbH, Hamburg. His research interests include data processing for radar and lidar sensors in various areas of application.

Christian Haas received the Diploma degree in geophysics from the University of Kiel, Kiel, Germany, in 1993, and the Ph.D. degree in geophysics from the University of Bremen, Bremen, Germany, in 1996.

He was a Senior Scientist at the Alfred Wegener Institute for Polar and Marine Research, Bremerhaven, until 2007, a Professor in sea-ice geophysics at the University of Alberta, Edmonton, AB, Canada, until 2012, and a Tier 1 Canada Research Chair for Arctic Sea Ice Geophysics at York University, Toronto, ON, Canada. Since 2016, he has been a Professor in sea-ice geophysics at the University of Bremen and the Alfred Wegener Institute. His research interest includes the role of sea ice in the climate, eco, and human systems, with a focus on ice and snow thickness observations using *in situ*, airborne, and satellite data.

Chapter 5

Application of airborne snow depth: deriving sea-ice bulk density[1]

This chapter is a preprint currently under review as

Jutila, A.[1], Hendricks, S.[1], Ricker, R.[1,a], von Albedyll, L.[1], Krumpen, T.[1], and Haas, C.[1,2]: **Retrieval and parametrisation of sea-ice bulk density from airborne multi-sensor measurements**, *The Cryosphere Discuss.* [preprint], https://doi.org/10.5194/tc-2021-149, in review, 2021.

[1] *Alfred Wegener Institute, Helmholtz Centre for Polar and Marine Research, Bremerhaven, Germany*
[2] *Institute of Environmental Physics, University of Bremen, Bremen, Germany*
[a] *Present address: Technology Department, Norwegian Research Centre, Tromsø, Norway*

Author contributions

AJ carried out the analysis with support from SH and RR and prepared the manuscript with input from all authors. AJ, SH, and RR collected the data. SH applied the density parametrisation to the CryoSat-2 data and produced Fig. 5.9. LvA processed the EM-Bird data to identify level and deformed ice. TK conducted the backward-tracking of sea ice with ICETrack.

[1] After the submission of this dissertation, this manuscript has been published. The updated citation is **Jutila, A.**, Hendricks, S., Ricker, R., von Albedyll, L., Krumpen, T., and Haas, C.: **Retrieval and parameterisation of sea-ice bulk density from airborne multi-sensor measurements**, *The Cryosphere*, 16, 259–275, https://doi.org/10.5194/tc-16-259-2022, 2022.

Abstract. Knowledge of sea-ice thickness and volume depends on freeboard observations from satellite altimeters and in turn on information of snow mass and sea-ice density required for the freeboard-to-thickness conversion. These parameters, especially sea-ice density, are usually based on climatologies constructed from in situ observations made in the 1980s and before while contemporary and representative measurements are lacking. Our aim with this paper is to derive updated sea-ice bulk density estimates suitable for the present Arctic sea-ice cover and a range of ice types to reduce uncertainties in sea-ice thickness remote sensing. Our sea-ice density measurements are based on over 3000 km of high-resolution collocated airborne sea-ice and snow thickness and freeboard measurements in 2017 and 2019. Sea-ice bulk density is derived assuming isostatic equilibrium for different ice types. Our results show higher average bulk densities for both first-year ice (FYI) and especially multi-year ice (MYI) compared to previous studies. In addition, we find a small difference between deformed and possibly unconsolidated FYI and younger MYI. We find a negative-exponential relationship between sea-ice bulk density and sea-ice freeboard and apply this parametrisation to one winter of monthly gridded CryoSat-2 sea-ice freeboard data. We discuss the suitability and the impact of the derived FYI and MYI bulk densities for sea-ice thickness retrievals and the uncertainty related to the indirect method of measuring sea-ice bulk density. The results suggest that retrieval algorithms be adapted to changes in sea-ice density and highlight the need of future studies to evaluate the impact of density parametrisation on the full sea-ice thickness data record.

5.1 Introduction

Sea ice affects the heat, moisture, and energy exchange between the ocean and the atmosphere, therefore monitoring the state of sea ice is crucial for understanding the current climate, how it may evolve, and what its impact may be (e.g., Stroeve and Notz, 2018). Observing sea-ice thickness and volume over decadal periods relies on freeboard measurements by satellite laser and radar altimeters. The conversion of freeboard to sea-ice thickness requires information of snow mass as well as the density of the sea-ice layer. Observations of both input parameters are sparse and the unknown spatial and temporal variability and trends of snow mass and sea-ice density directly translate into the uncertainty of the sea-ice thickness data record (Giles et al., 2007; Kwok, 2010; Zygmuntowska et al., 2014). The current uncertainties related to sea-ice thickness and volume retrievals are sometimes deemed too large for modelling comparisons (SIMIP Community, 2020), and therefore improved accuracy of sea-ice thickness is highly desired (Duchossois et al., 2018). Coming to the era of satellite altimetry, starting with the European Remote Sensing satellite ERS-1 mission of the European Space Agency (ESA) in 1993, multi-year ice (MYI, ice that has survived at least two melt seasons) covered about 40 % of the late-winter Arctic and already showed signs of reduction in areal coverage. Since then, Arctic sea ice has undergone rapid change due to the warming climate resulting in a thinner and younger ice cover (Maslanik et al., 2011; Comiso, 2012; Meier et al., 2014; Stroeve and Notz, 2018). Toward the end of 2010s, MYI continued to decline and constituted barely 10 % of the Arctic sea-ice extent while the relative extents of the thinner

first-year ice (FYI, ice that has not undergone a melt season) and second-year ice (SYI, ice that has survived one melt season) have increased (Stroeve and Notz, 2018).

Due to the lack of spatially and temporally representative snow observations, sea-ice thickness retrieval methods are based on, e.g., monthly snow climatologies or modelled reconstructions from reanalysis. Currently the most widely used source for snow mass information is the snow climatology in Warren et al. (1999) (hereafter W99) using data collected during the Soviet North Pole drifting stations in 1954–1991. However, the stations were located exclusively on MYI and thus introduce a bias. In response to the declining MYI, many satellite data products of Arctic sea-ice thickness are derived by using a modified W99, where the snow depth values are halved on ice that corresponds to FYI (Kurtz and Farrell, 2011; Sallila et al., 2019). In attempts to overcome the mismatch between the pre-1990s climatology and the shift toward FYI-dominated, thinner, and younger Arctic sea ice, a number of new snow depth products have emerged in recent years. W99 was complemented with data from airborne Sever expeditions covering in particular FYI in the shelf seas of the Eurasian Russian Arctic in late-winter (March–May) 1959–1986. Other approaches have utilised atmospheric reanalysis data to model a reconstruction of snow on Arctic sea ice in varying spatial and temporal resolutions. Snow depth has been derived using brightness temperatures from passive microwave satellites as well as combining dual-altimetry freeboard information from Ku band and Ka band or laser satellite altimeters. Descriptions of the different snow depth products currently available can be found in the inter-comparison study of Zhou et al. (2021). Some constraints of the current products will be reduced by near real-time dual-altimetry acquisitions, such as the resonance of the CryoSat-2 and ICESat-2 satellite orbits (CRYO2ICE) since July 2020, and future single-platform dual-frequency satellite missions like the Copernicus Polar Ice and Snow Topography Altimeter (CRISTAL) mission by ESA (Kern et al., 2020) with a launch planned in 2027. Similar efforts to bring sea-ice density values up-to-date should be taken as well.

Sea ice is a multi-phase substance consisting of solid ice, liquid brine, and gas (air) bubbles with densities and relative amounts depending on temperature (Timco and Frederking, 1996). Calculated from its molecular structure, density of pure ice is 916.8 kg m^{-3} (Pounder, 1965), while liquid, saline water increases and air inclusions decrease the sea-ice bulk density (weight per unit volume including voids and enclosed water). Through processes like brine expulsion, gravity drainage, and meltwater flushing, sea ice is desalinated over time as pore space previously occupied by highly saline brine is replaced by sea water and air resulting in decreased density of MYI (Petrich and Eicken, 2017). Several studies have demonstrated the rather large range of values for sea-ice density despite little brine drainage and with differences in respect to the waterline and ice type: above the waterline FYI density is 840–910 kg m^{-3} and MYI density is 720–910 kg m^{-3}, whereas below the waterline ice is saturated by sea water and has a density of 900–940 kg m^{-3} less dependent on its age (Timco and Frederking, 1996; Timco and Weeks, 2010; Pustogvar and Kulyakhtin, 2016). Especially with satellite altimetry applications in mind, Alexandrov et al. (2010) derived a density of 916.7 ± 35.7 kg m^{-3} for FYI using the drill-hole data set of airborne Sever expeditions

concentrated in the shelf seas of the Eurasian Russian Arctic in the 1980s and a density of 882 ± 23 kg m^{-3} for MYI as a weighted average of the layers above and below the waterline using values from literature. The values by Alexandrov et al. (2010) (hereafter A10) are the most commonly used in sea-ice thickness retrieval algorithms (Sallila et al., 2019).

Accurate and representative measurements of sea-ice density using traditional techniques are temporally and spatially limited. Most of them require coring or cutting out pieces of ice, such as the mass/volume, displacement (submersion), or specific gravity techniques, making them susceptible for inaccuracies through brine drainage and imprecise volume of the samples (Timco and Frederking, 1996). This can be avoided by carefully recording sea-ice thickness and freeboard, e.g., with drill-hole measurements, in addition to the snow depth atop and calculating the sea-ice bulk density assuming isostatic equilibrium and densities of snow and sea water. However, significant error may be introduced locally where sea ice is not isostatically compensated due to lateral stresses, e.g., close to pressure ridges (Timco and Frederking, 1996). Previous parametrisations of sea-ice density include the effective freeboard approach (snow depth converted to ice thickness using their density ratio) by Ackley et al. (1976) using drill-hole measurements from 400 m of profile lines on MYI in the Beaufort Sea and a parametrisation based on ice floe thickness by Kovacs (1997) utilising 17 FYI and 4 MYI sea-ice cores from the Beaufort Sea. Neither of these parametrisations have been widely used. Moreover, the multi-phase nature of sea ice is an ongoing challenge for modelling approaches (Hunke et al., 2011). There is a definite need for evaluating sea-ice density because there is no density climatology available representing the current state of sea ice, nor is it possible to observe density by satellites from space.

Simultaneous, collocated, and preferably single-platform measurements of the key parameters of the entire sea-ice–snow layer covering a wide range of ice types and conditions on regional scales are required to decrease the uncertainties related to the conversion of freeboard to sea-ice thickness. Since 2017, a unique sensor configuration on the Alfred Wegener Institute's (AWI) IceBird winter campaigns combines airborne laser, radar, and electromagnetic induction sounding instruments making it now possible to measure them on a single platform. In this paper, we present high-resolution data of simultaneous airborne sea-ice thickness, freeboard, and snow depth over late-winter Arctic sea ice from the AWI IceBird campaigns in 2017 and 2019. Observing the locations of the air–snow, snow–ice, and ice–water interfaces in the sea-ice system along survey tracks allows us to estimate sea-ice bulk density that also serves as a consistency check between the sea-ice thickness, freeboard, and snow depth measurements. We also derive an updated parametrisation of sea-ice bulk density suitable for the present Arctic sea-ice cover including the densities of deformed sea ice which, if unconsolidated, can deviate even more strongly from the density of solid ice.

5.2 Data and methods

5.2.1 Aircraft campaigns

The AWI IceBird program (see reference list for a link to webpage) is a series of airborne campaigns carried out using the institute's two Basler BT-67 research aircraft *Polar5* and *6* (Alfred-Wegener-Institut Helmholtz-Zentrum für Polar- und Meeresforschung, 2016) to measure Arctic sea ice and its change since 2009. The campaigns operate from airfields extending from Longyearbyen in Svalbard to Utqiagvik (Barrow) in Alaska and coincide closely with the Arctic sea ice summer minimum (August) and winter maximum (April). The primary scientific instrumentation on the aircraft includes an electromagnetic (EM) induction sounding instrument (EM-Bird) to measure total (i.e., ice+snow) thickness, an airborne laser scanner (ALS) for surface topography and freeboard measurements, a microwave radar to measure snow depth, and an infrared radiation pyrometer to record surface temperature (Fig. 5.1). We describe each instrument in the following sections. The low altitude of 200 ft ($\approx$ 60 m) and slow speed of 110 kn ($\approx$ 60 m s^{-1}) during the nominal surveys are beneficial for high-resolution data acquisition.

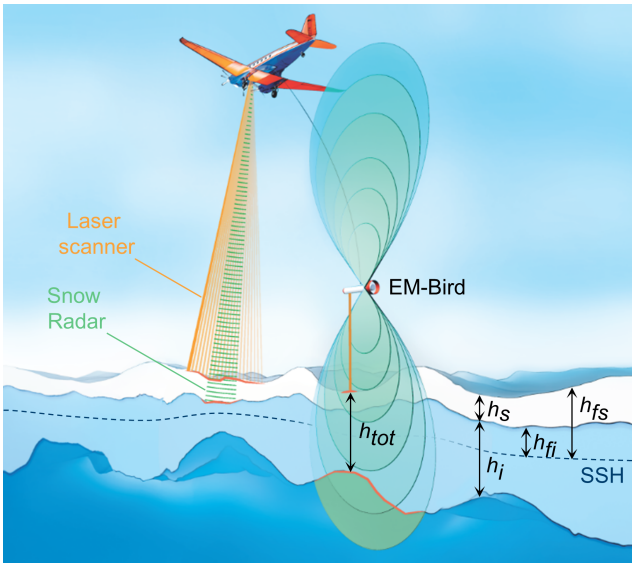

Figure 5.1. Sketch of the IceBird sea-ice campaign setup with the EM-Bird (black text), the laser scanner (orange), and the Snow Radar (green). Different components of sea ice are highlighted in the cross-section: total (ice+snow) thickness (h_{tot}), snow depth (h_s), sea-ice thickness (h_i), sea-ice freeboard (h_{fi}), and snow freeboard (h_{fs}). SSH stands for local sea-surface height, depicted by the blue dashed line. Adapted with annotations from the graphic by Alfred Wegener Institute / Martin Künsting CC-BY 4.0.

In this study, we used data collected during the IceBird winter campaigns in early April of 2017 and 2019 (Table 5.1; Fig. 5.2) utilising the unique data set of simultaneous total thickness, snow freeboard, and snow depth measurements. From 2017, we used measurements from four survey flights that took place over the Beaufort and Chukchi Seas as part of the Polar Airborne Measurements and Arctic Regional Climate Model Simulation Project (PAMARCMiP; Haas et al., 2010; Herber et al., 2012). From 2019, we included five survey flights that covered regions in the Lincoln Sea and the Arctic Ocean in addition to an overlap with the measurements in the Beaufort Sea in 2017.

Table 5.1. IceBird surveys in 2017 and 2019 in the focus of this study (Fig. 5.2) together with their total lengths and instrument retrieval rates.

#	Date	Base	Survey (Region)	Total distance [km]	Retrieval rates [%]		
					EM-Bird	ALS	Snow Radar
1	2 April 2017	Inuvik, Canada	Beaufort Loop	416	87	75	81
2	4 April 2017	Inuvik, Canada	AltiKa track (Beaufort)	265	90	99	82
3	6 April 2017	Utqiagvik, USA	Sentinel-3A track (Chukchi)	463	91	93	79
4	8 April 2017	Utqiagvik, USA	ULS & UiTSat (Chukchi)	619	81	93	77
5	2 April 2019	Eureka, Canada	Nansen Sound, Arctic Ocean	294	90	76	83
6	5 April 2019	Eureka, Canada	Lincoln Sea	189	88	99	78
7	7 April 2019	Inuvik, Canada	Beaufort Triangle	470	85	97	54
8	8 April 2019	Inuvik, Canada	Amundsen Gulf (Beaufort)	279	82	97	70
9	10 April 2019	Inuvik, Canada	ICESat-2 track (Beaufort)	415	76	98	90

Table 5.2. Summary of the key variables and their assumed values, uncertainties, and resolutions.

Variable	Unit	Value	Uncertainty (σ)	Resolution
Total thickness (h_{tot})	[m]		0.1^a	5–6 m spacing, 40 m footprint
Snow freeboard (h_{fs})	[m]		0.1^b	0.25 m regular grid
Snow depth (h_s)	[m]		$\frac{0.069^c}{\sqrt{N}}$	4–5 m spacing, 1.0/2.6 m footprint along-/across-track
Snow density (ρ_s)	[kg m^{-3}]	300^d	34^e	
Sea-water density (ρ_w)	[kg m^{-3}]	1024^f	0.5^f	
Sea-ice density (ρ_i)	[kg m^{-3}]	Eq. (5.3)	Eq. (5.4)	

[a] Pfaffling et al. (2007); Haas et al. (2009); [b] see Sect. 5.2.3; [c] see Sect. 5.2.4; Jutila et al. (2021b); [d] Warren et al. (1999); [e] King et al. (2020b); [f] Wadhams et al. (1992)

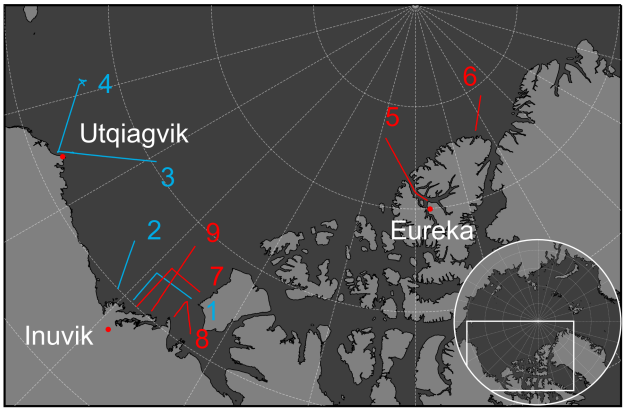

Figure 5.2. IceBird surveys in 2017 (blue) and 2019 (red) in the focus of this study. The numbering corresponds to the individual surveys listed in Table 5.1.

5.2.2 Sea-ice thickness

We measured total (ice+snow) thickness of sea ice (h_{tot}) using the towed EM induction sounding instrument, the EM-Bird, suspended below the aircraft 10–20 m above the sea ice surface (Haas et al., 2009) as illustrated in Fig. 5.1. The EM-Bird utilises the contrast between resistive snow and ice layers and conductive sea water by transmitting an EM field that induces eddy currents only in the latter (Kovacs and Morey, 1991; Haas et al., 1997). The EM-Bird measures the phase and amplitude of a secondary EM field induced by those eddy currents in relation to the primary field. The phase and amplitude of the secondary field depend on the distance between the instrument and the ice–water interface and decrease negative-exponentially with increasing distance. Subtracting the instrument height above the surface, measured by an integrated laser altimeter, from the distance to the sea water gives the total thickness (Haas et al., 2009, 2021). Sea-ice thickness (h_i) was derived by subtracting snow depth from total thickness (see Sect. 5.2.4). The EM-Bird sampling rate was 10 Hz, which translated to 5–6 m point spacing at the nominal survey speed. Approximately every 15–20 minutes brief ascents to more than 100 m were carried out to monitor the sensor drift during post-processing (Haas et al., 2009). Comparison to drill-hole measurements over level ice have indicated an accuracy of 0.1 m, whereas ridge peak thicknesses are generally underestimated by up to 50 % as a result of mass-conserving averaging effects within the approximately 40 m diameter footprint of the instrument (Pfaffling et al., 2007; Haas et al., 2009). For our analysis, we disregarded measurements of total thickness (i) less than the instrument accuracy of 0.1 m, (ii) where total thickness was less than the mean snow freeboard or snow depth, and (iii) where the surface temperature was above −5 °C within the footprint of the instrument to avoid open or newly frozen leads with total thickness below the accuracy of the EM-Bird (see Sect. 5.2.4 and 5.2.5.1).

5.2.3 Freeboard

The near-infrared (1064 nm), line-scanning Riegl VQ-580 airborne laser scanner (ALS) measured ellipsoidal elevations of ice surfaces with a 60° field of view resulting in a swath width approximately equal to the aircraft's altitude above ground (nominally ≈ 60 m). We obtained

freeboard from the ALS data by subtracting the local sea-surface height from the ice surface elevations. The height of the sea surface along the flight track is sporadically observed by the ALS at fractures (leads) of the sea-ice cover and we manually selected the corresponding elevations. We subtracted the mean sea surface (DTU15 MSS; Andersen et al., 2016) from the surface elevations to remove large scale variations and reduce interpolation errors before interpolating the sea-surface height tie points along the flight track. Subtracting the interpolated sea-surface height from the ice elevations results in snow freeboard (h_{fs}), as the elevation measurement of the ALS always includes the snow layer (Fig. 5.1). Sea-ice freeboard (h_{fi}), i.e., the location of the snow–ice interface in relation to the local sea level, was derived by subtracting snow depth from snow freeboard (see Sect. 5.2.4). We then interpolated the obtained point cloud data of snow freeboard onto a regular grid with a 0.25 m resolution. Freeboard uncertainties are dominated by the accuracy of the interpolation of the instantaneous sea surface anomaly that depends on the abundance of leads. Therefore, especially regions with packed MYI and low lead density are associated with high uncertainties (Ricker et al., 2016) and we manually masked out such areas. Supervising the along-track interpolation, we estimated an overall uncertainty of 0.1 m. For each total thickness measurement, we calculated the corresponding mean snow freeboard within the EM-Bird footprint (Fig. 5.3).

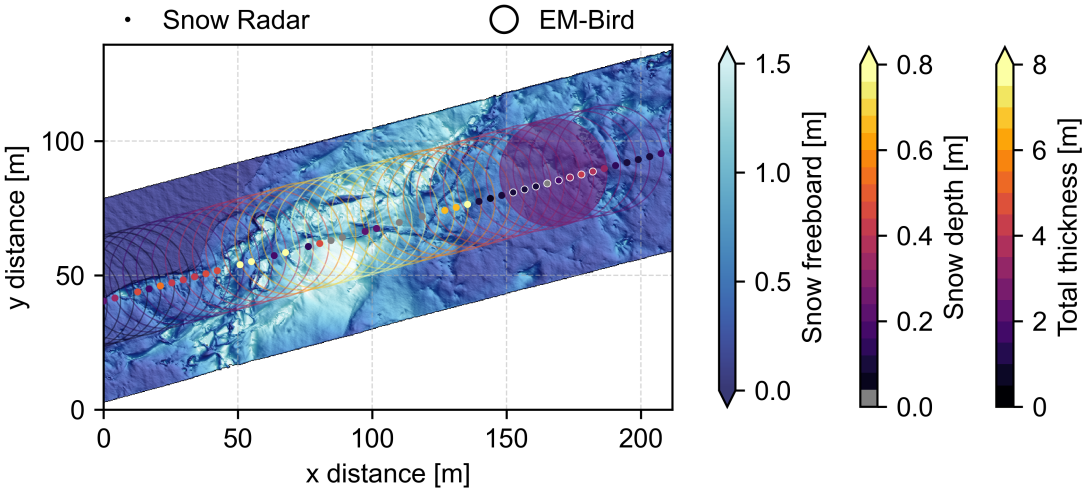

Figure 5.3. Example of the primary data sets: the bluish colours show the gridded 0.25 m resolution swath of snow freeboard (h_{fs}) measured by the ALS; the small filled circles are the snow depth estimates (h_s) from the Snow Radar, where the diameter of the circle corresponds to the theoretical smooth surface cross-track footprint of the radar; and the large open circles represent the total (ice+snow) thickness measurements (h_{tot}) from the EM-Bird in their respective footprint size. One EM-Bird footprint on the right is highlighted (filled transparent colour) to demonstrate the averaging of snow depth estimates (white outlines) and freeboard. A refrozen lead can be seen in the upper left corner of the figure and a pressure ridge in the middle.

5.2.4 Snow depth

We used an ultra-wideband (2–18 GHz), frequency-modulated continuous-wave (FMCW), quad-polarised microwave radar, hereafter Snow Radar, to measure snow depth on sea ice (h_s). The radar was developed by the Center of Remote Sensing of Ice Sheets (CReSIS) at

the University of Kansas, and similar radars have been operated as part of NASA's Operation IceBridge (OIB) since 2009 (MacGregor et al., 2021). Similar to the ALS, the Snow Radar transmitter and receiver antennae were mounted under the aft floor of the aircraft looking nadir (Fig. 5.1). Due to the broad bandwidth of the radar, its range resolution was 1.14 cm in snow when assuming a snow density of 300 kg m^{-3}. The low altitude and slow speed of the IceBird surveys resulted in an approximately 4–5 m sample spacing and a theoretical smooth surface footprint diameter of only 2.6 m across-track and 1.0 m along-track (Fig. 5.3). A detailed description of the radar is given in Yan et al. (2017a) and Jutila et al. (2021b).

To calibrate the raw Snow Radar data, we used a workflow described in Jutila et al. (2021b) including coherent noise removal and system impulse deconvolution. Using an open-source python package pySnowRadar (King et al., 2020a), we detected air–snow and snow–ice interfaces with the algorithm by Jutila et al. (2021b) that is based on a pulse peakiness approach by Ricker et al. (2014) used in satellite altimetry. Taking into account the decreased wave propagation speed in snow by assuming a snow density, the distance between the identified interfaces determined the snow depth estimate. In post-processing, we filtered out values which were acquired during the EM-Bird calibration manoeuvres with a simple altitude threshold of 100 m and when the absolute roll or pitch of the aircraft exceeded 5°. Additionally, for each snow depth estimate we calculated a surface topography estimate (h_{topo}) as the difference between the 95th and 5th percentile of the ALS surface elevation data within the radar footprint to disregard potentially erroneous snow depth estimates over heavily deformed sea ice using a threshold value of 0.5 m (Jutila et al., 2021b).

A validation exercise over level, landfast FYI yielded a mean bias of 0.86 cm and a root-mean-square error (RMSE) of 6.9 cm for the radar-derived snow depth estimates (Jutila et al., 2021b). For each total thickness measurement, we calculated the corresponding mean snow depth requiring at least five valid snow depth estimates within the EM-Bird footprint (corresponds to approximately 50 % of the values; Fig. 5.3). The averaging reduced the error by a factor of $\sqrt{N}$, where N is the number of averaged estimates. We disregarded averaged snow depth values where the surface temperature within the EM-Bird footprint was above −5 °C and where the mean snow freeboard was less than the mean snow depth (negative sea-ice freeboard) to avoid potentially erroneous snow depth retrievals due to changes in the dielectric properties of snow induced by liquid water (Barber et al., 1995; Kurtz and Farrell, 2011; Kurtz et al., 2013).

5.2.5 Auxiliary data

5.2.5.1 Surface temperature

Surface temperature was acquired using the Heitronics infrared radiation pyrometer KT19.85II that recorded the 9.6–11.5 μm spectral band response of the surface with a sampling rate of 50 Hz resulting in an approximately 1 m sample spacing and 3.1 m diameter footprint at the nominal survey speed and altitude. The manufacturer reported an accuracy of ±0.5 °C + 0.7 % of the temperature difference between the target and the instrument hous-

ing. We used the measurements to filter out total thickness and snow depth measurements where the surface temperature was above −5 °C (see Sect. 5.2.2 & 5.2.4).

5.2.5.2 Sea-ice type

Information of sea-ice type is required for accurate classification the sampled ice. However, no remote sensing product or modelling output is able to match the resolution of the airborne survey data. Therefore, we used a custom sea-ice classification scheme. We started with identifying level and deformed ice following the approach of Rabenstein et al. (2010). Conditions for level ice were met when the along-track total thickness gradient using a three-point Lagrangian interpolator was less than 0.04 and the level ice section extended for at least 100 m. Otherwise, ice was deemed deformed. We then chose the nearest neighbour data point from the coinciding EASE-Grid Sea Ice Age (Version 4) product from the National Snow & Ice Data Center (NSIDC; Tschudi et al., 2019b) providing weekly sea-ice age estimates in 12.5 km resolution. Where the NSIDC Sea Ice Age data were not available (landfast ice and close to coasts), we manually assigned the ice type to FYI or MYI (old ice, including SYI) according to the Canadian Ice Service (CIS) regional and weekly ice charts (Canadian Ice Service, 2009). Finally, we defined the ice type as (i) first-year ice (FYI), if the ice was younger than 1 year according to NSIDC/CIS or the observed ice thickness was below 2 m regardless of its age; (ii) second-year ice (SYI), if the ice had a thickness of 2 m or more and its age was 1–2 years; and (iii) multi-year ice (MYI), if the ice had a thickness of 2 m or more and was at least 2 years old. To account for the spatial and temporal limitations of the NSIDC Sea Ice Age product and the drift of sea ice, we adjusted the ice type classification from FYI to MYI for any ice that indicated an age less than 1 year but was level and thicker than 2 m or, after along-track averaging over a length scale (see Sect. 5.2.6), the lower quartile (25th quantile) of the averaged ice thickness values within the length scale was above 2 m.

To support the analysis of the sampled sea ice and to evaluate the indicated sea-ice age in the NSIDC product, we investigated the sea-ice age, pathways, and origin using the Lagrangian drift analysis system ICETrack (Krumpen, 2018; Krumpen et al., 2020). We split the surveyed sea ice into 25 km along-track segments and tracked them backwards in time in daily increments utilising a publicly available low-resolution satellite sea ice motion product from the Ocean and Sea Ice Satellite Application Facility (OSISAF; Lavergne et al., 2010). The tracking was terminated if the trajectory hit the coastline or the edge of landfast ice. In addition, if the sea-ice concentration, provided by the Center for Satellite Exploitation and Research (CERSAT; Ezraty et al., 2007), along the backward trajectory dropped below 25 %, we assumed that the ice was formed in that specific location. To quantify uncertainties of sea-ice trajectories, Krumpen et al. (2019) reconstructed the pathways of 57 drifting buoys. The authors showed that the deviation between actual and virtual tracks was rather small, 36 ± 20 km after 200 days, and considered to be in an acceptable range.

5.2.6 Sea-ice bulk density

Simultaneous measurements of sea-ice thickness, snow depth, and freeboard enable us to calculate sea-ice bulk density using the so-called "freeboard and ice thickness technique" (Timco and Frederking, 1996). Archimedes' principle dictates

$$\rho_i h_i + \rho_s h_s = \rho_w \left(h_i - h_{fi}\right) \tag{5.1}$$

where ρ is density for ice, snow, and sea water denoted with subscripts i, s, and w, respectively. The terms can be rearranged to solve for ρ_i:

$$\rho_i = \rho_w \left(1 - \frac{h_{fi}}{h_i}\right) - \rho_s \frac{h_s}{h_i}. \tag{5.2}$$

By substituting measured total thickness and snow depth for sea-ice thickness ($h_i = h_{tot} - h_s$) in addition to snow freeboard and snow depth for sea-ice freeboard ($h_{fi} = h_{fs} - h_s$), we obtain

$$\rho_i = \rho_w \left(1 - \frac{h_{fs}}{h_{tot} - h_s}\right) + \left(\rho_w - \rho_s\right) \frac{h_s}{h_{tot} - h_s}. \tag{5.3}$$

To solve Eq. (5.3), we need to assume values only for the densities of sea water and snow, but their impact on the uncertainty of sea-ice bulk density is small (see Eq. (5.4) below). Here we took sea-water density and its uncertainty according to Wadhams et al. (1992) as $\rho_w = 1024$ kg m^{-3} and $\sigma_{\rho_w} = 0.5$ kg m^{-3}, respectively. For snow density in April, when measurements were carried out, we chose $\rho_s = 300$ kg m^{-3} following Warren et al. (1999) and for the respective uncertainty $\sigma_{\rho_s} = 34$ kg m^{-3} from King et al. (2020b). These values and the uncertainties of the measured variables are summarised in Table 5.2. Assuming that the individual uncertainties are uncorrelated, we can derive uncertainty for sea-ice bulk density (σ_{ρ_i}) using Gaussian error propagation:

$$\begin{aligned}
\sigma_{\rho_i} &= \left[\left(\frac{\partial \rho_i}{\partial \rho_w}\right)^2 \sigma^2_{\rho_w} + \left(\frac{\partial \rho_i}{\partial \rho_s}\right)^2 \sigma^2_{\rho_s} + \left(\frac{\partial \rho_i}{\partial h_{tot}}\right)^2 \sigma^2_{h_{tot}} + \left(\frac{\partial \rho_i}{\partial h_s}\right)^2 \sigma^2_{h_s} + \left(\frac{\partial \rho_i}{\partial h_{fs}}\right)^2 \sigma^2_{h_{fs}}\right]^{\frac{1}{2}} \\
&= \left[\left(1 + \frac{h_s - h_{fs}}{h_{tot} - h_s}\right)^2 \sigma^2_{\rho_w} + \left(\frac{h_s}{h_{tot} - h_s}\right)^2 \sigma^2_{\rho_s} + \left(\frac{\rho_w \left(h_{fs} - h_s\right) + \rho_s h_s}{\left(h_{tot} - h_s\right)^2}\right)^2 \sigma^2_{h_{tot}} \right. \\
&\quad \left. + \left(\frac{\rho_w \left(h_{tot} - h_{fs}\right) - \rho_s h_s}{\left(h_{tot} - h_s\right)^2}\right)^2 \sigma^2_{h_s} + \left(\frac{\rho_w}{h_{tot} - h_s}\right)^2 \sigma^2_{h_{fs}}\right]^{\frac{1}{2}}.
\end{aligned} \tag{5.4}$$

Following the uncertainty source analysis of Giles et al. (2007) and using the values summarised in Table 5.2, the largest contributors to the uncertainty of sea-ice bulk density are, in descending order of magnitude, snow freeboard, snow depth, and total thickness. We disregarded density values with uncertainty exceeding 100 kg m^{-3} from further analysis.

While the assumption of isostatic equilibrium may not necessarily be valid locally, e.g., close to pressure ridges, it holds true when averaging over a sufficient length scale. We varied the averaging length in 10 m increments and found that the mean bulk densities and

the standard deviations of the surveys did not change significantly beyond a length scale of about 200 m. Here, we computed sea-ice bulk density estimates at two length scales representing the sensor resolution of the CryoSat-2 satellite as well as the typical resolution of gridded sea-ice thickness data. In the first case, we approximated the scale of full-resolution altimeter footprint by the diameter of a circle with the same area as the 300×1650 m pulse-Doppler-limited footprint of CryoSat-2 in the synthetic aperture radar (SAR) acquisition mode. The diameter of that circle is equal to approximately 800 m. In the second case, we chose the typical satellite product grid cell size of 25 km. We assumed that the sea-ice and snow layers are in isostatic equilibrium at both scales. We calculated an along-track weighted average using the squares of individual uncertainty values as weights (inverse-variance method):

$$\bar{\rho_i} = \frac{\sum_{i=1}^{N} \frac{1}{\sigma_{\rho_i}^2} \rho_i}{\sum_{i=1}^{N} \frac{1}{\sigma_{\rho_i}^2}} \tag{5.5}$$

where N equals the number of values within the length scale to be averaged. The resulting uncertainty was determined with

$$\sigma_{\bar{\rho_i}} = \sqrt{\frac{1}{\sum_{i=1}^{N} \frac{1}{\sigma_{\rho_i}^2}}}. \tag{5.6}$$

We calculated inverse-variance weighted averages also for snow depth since its uncertainty varied spatially. For all other variables we calculated an arithmetic mean.

5.3 Results

This study included a total of 3410 airborne survey kilometres split approximately equally between the years 2017 and 2019 (Table 5.1). The abundance of different sea-ice types varied between the years and the individual surveys (see the percentages in Table 5.3). Surveyed sea ice in 2017 was solely FYI. This was a result of the ice-free conditions in the Beaufort and Chukchi Seas in the previous summer, additionally influenced by the collapse of the semipermanent Beaufort high pressure system, and the subsequent reversal of the Beaufort Gyre in the winter prohibiting typical import of MYI to the region (Babb et al., 2020). In 2019, FYI was encountered primarily in the surveys over the southern Beaufort Sea and the Amundsen Gulf but also embedded within the MYI zone in refrozen leads constituting 41 % of the calculated density values. The percentage of SYI was generally low, only around 7 %. The largest percentage of SYI was observed in the survey over the Lincoln Sea on 5 April with minor occurrences on other surveys of that year. Similar to SYI, MYI was included only in the surveys in 2019 not only because of the imported MYI had returned to the Beaufort Sea within the range of the aircraft but also because the data included surveys over the Lincoln Sea and Arctic Ocean within the Last Ice Area where the oldest and thickest sea ice in the

Arctic resides (Moore et al., 2019). Overall, approximately half of the sea ice sampled in 2019 was identified as MYI.

Figure 5.4 shows the backtracked pathways of the sampled sea ice. ICETrack results from 2017 (panel a) confirmed that all sampled ice was FYI. Indicated sea-ice age was up to approximately 180 d in the Beaufort Sea and up to approximately 150 d in the Chuckhi Sea corresponding to freeze-up in October and November, respectively. In 2019 (panel b), the sampled old ice was indeed up to several years old originating from the Beaufort Gyre. The chosen 25 km backtracking segment length did not resolve any SYI in 2019 pointing to a likely very scarce and localised appearance of SYI.

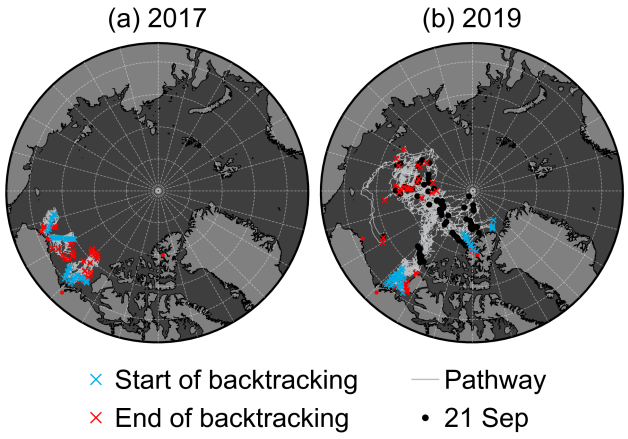

Figure 5.4. Pathways of the sea ice sampled (a) in 2017 and (b) in 2019. Black dots (visible only in (b)) represent the position of the backtracked sea ice on 21 September in the preceding years before sampling, when ice parcels are considered to have survived the summer.

5.3.1 Sea-ice bulk density

Figure 5.5 shows an example section of a measured sea-ice profile, roughly 30 km in length along a survey track and including different ice types in the Beaufort Sea in 2019. The bulk densities of FYI, SYI, and MYI, derived using the along-track length scale of 800 m, are stated in Table 5.3 and shown in Fig. 5.6. On average, FYI bulk density was higher than the value derived by Alexandrov et al. (2010) (A10), also for individual surveys. FYI bulk density in 2017 was slightly higher than in 2019, and combined they resulted in an average density of 928.5 ± 16.4 kg m^{-3}. SYI and MYI bulk densities differed only a little from each other, but were 23–30 kg m^{-3} lower than FYI bulk density. Similar to FYI, the bulk densities of old ice were in the upper range of or even beyond A10. Figure 5.7 shows the spatial distribution of the derived sea-ice bulk density when averaged over a typical satellite product grid cell size of 25 km. As expected, lower density values were generally encountered with increasing ice age (Fig. 5.7e and f). The lowest sea-ice bulk density values were located 50–150 km northwest off the edge of the landfast ice and the coast of Ellesmere Island and Nansen Sound (Fig. 5.7e). Moreover, there was noticeable along-track variability of bulk density also within a single ice type, even FYI where also the highest bulk density values were observed.

Table 5.3. Summary of the 800 m along-track averaged sea-ice bulk density (inverse-variance weighted mean ± one standard deviation) according to survey and ice type. The mean values correspond to the red crosses in Fig. 5.6. The percentage of each sea-ice type encountered on each survey is given in parentheses.

Survey	Region	ρ_i [kg m^{-3}]					
		FYI		SYI		MYI	
2 April 2017	Beaufort Sea	923.5 ± 16.0	(100 %)				
4 April 2017	Beaufort Sea	926.8 ± 13.9	(100 %)				
6 April 2017	Chukchi Sea	932.9 ± 15.3	(100 %)	N/A		N/A	
8 April 2017	Chukchi Sea	930.7 ± 15.8	(100 %)				
Mean		*929.3 ± 16.0*	*(100 %)*				
2 April 2019	Lincoln Sea	873.1 ± 0.0	(0.5 %)	875.2 ± 6.9	(5.5 %)	896.0 ± 19.2	(94 %)
5 April 2019	Arctic Ocean	931.3 ± 27.1	(2 %)	907.8 ± 12.9	(23 %)	907.0 ± 17.5	(75 %)
7 April 2019	Beaufort Sea	923.2 ± 14.8	(52 %)	902.7 ± 11.4	(5 %)	907.3 ± 15.5	(43 %)
8 April 2019	Beaufort Sea	929.7 ± 17.9	(100 %)	N/A		N/A	
10 April 2019	Beaufort Sea	921.6 ± 18.8	(51 %)	915.6 ± 10.4	(3 %)	913.6 ± 17.4	(46 %)
Mean		*925.4 ± 17.7*	*(41 %)*	*899.3 ± 17.4*	*(7 %)*	*902.4 ± 19.4*	*(52 %)*
A10 (Alexandrov et al., 2010)		916.7 ± 35.7		N/A		882 ± 23	

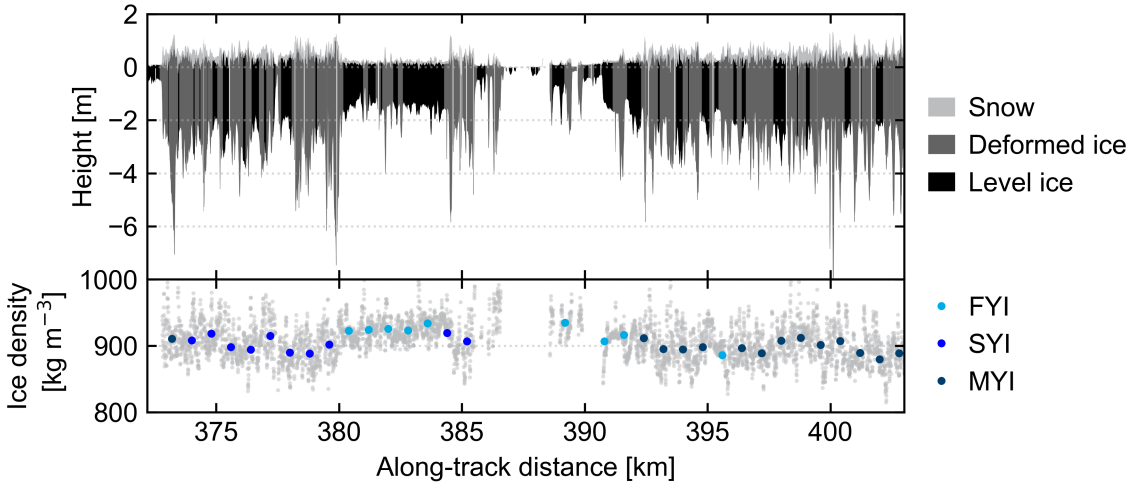

Figure 5.5. Approximately 30 km along-track profile during the survey over the Beaufort Sea on 7 April 2019. The upper panel shows the snow and ice layers, of which the latter is split into deformed and level ice sections, derived from the total thickness, snow freeboard, and snow depth measurements in the native 5–6 m point spacing. The zero height refers to the local sea-surface height. The corresponding calculated sea-ice bulk density values are represented by grey dots in the lower panel together with the 800 m along-track averages that are coded according to the sea-ice type with colour.

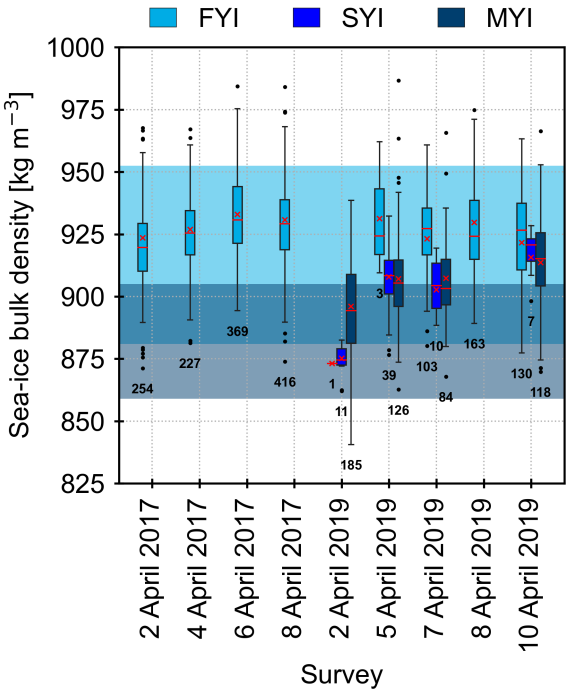

Figure 5.6. Sea-ice bulk density by ice type and survey in the 800 m length scale showing the interquartile range (IQR, Q3–Q1, boxes), the median values (red lines), the inverse-variance weighted mean (red crosses, Table 5.3), and outliers (beyond 1.5×IQR, dots). The numbers below the boxes correspond to the amount of averaged values contained in each ice type of each individual survey. The shading on the background shows the ± one standard deviation range around the A10 mean FYI (light blue) and MYI (dark blue) densities, respectively.

5.3.2 Parametrisation of sea-ice bulk density

We explored the possibility to parametrise sea-ice bulk density using one of the measured sea-ice parameters. Out of the full parameter space, sea-ice freeboard showed the best correlation with the estimated sea-ice bulk density, $r = -0.62$ ($p \ll 0.001$), indicating a significant, linear anti-correlation as expected according to Eq. (5.2) ($\rho_i \propto -h_{fi}$). However, the

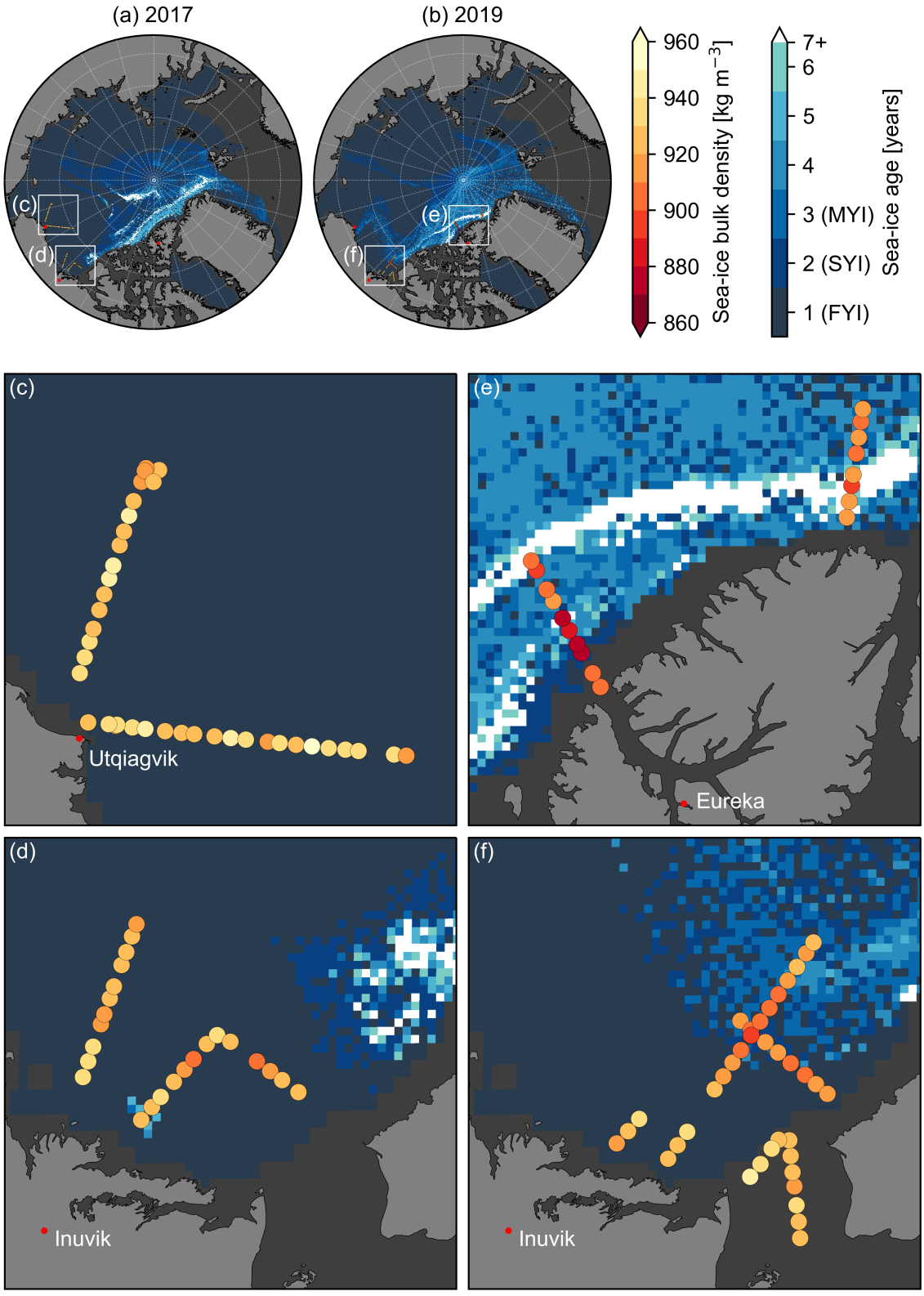

Figure 5.7. Sea-ice bulk density in 25 km along-track segments shown as coloured circles over the weekly NSIDC EASE-Grid Sea Ice Age product (2–8 April; Tschudi et al., 2019b) in bluish colours in 2017 (panels (a) & (c)–(d)) and in 2019 ((b) & (e)–(f)). The close-up panels (c)–(f) are 700×700 km in size and their locations are marked with white squares in the overview panels (a) and (b).

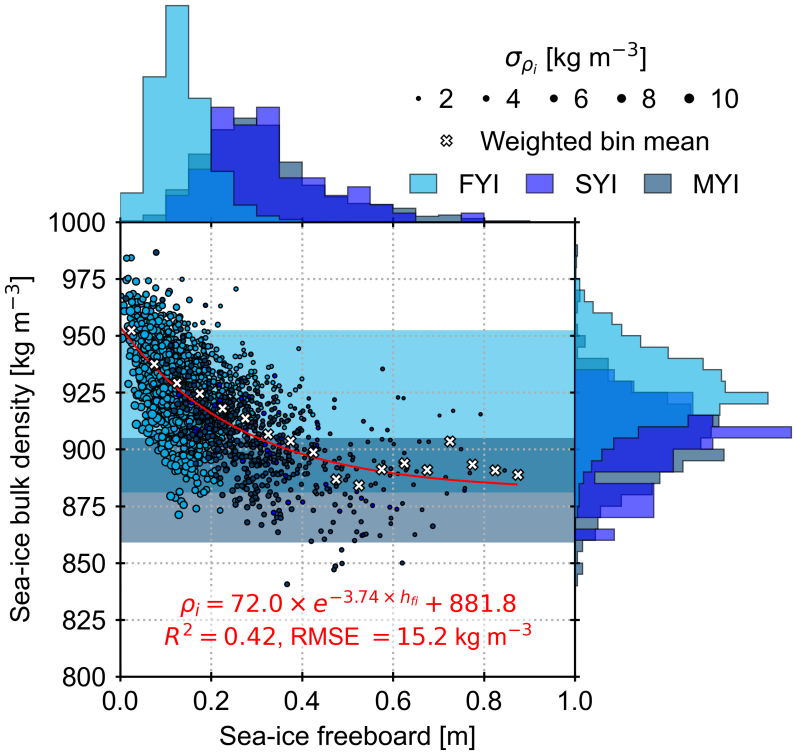

Figure 5.8. Parametrisation of sea-ice bulk density based on sea-ice freeboard. The scatter plot shows all sea-ice bulk density values from 2017 and 2019 in the 800 m length scale ($N = 2246$) against their corresponding sea-ice freeboard values, where the size of the point corresponds to the uncertainty of the density value (σ_{ρ_i}). The red line and text show the non-linear least-squares fit of an exponential function (Eq. (5.7)). R^2 stands for coefficient of determination and RMSE for root-mean-square error of the fitted curve. The crosses are the inverse-variance weighted means using a sea-ice freeboard bin size of 0.05 m. The shading on the background shows the ± one standard deviation range around the A10 mean FYI (light blue) and MYI (dark blue) densities, respectively. The histograms on the top and on the right show the probability density functions of freeboard and density, respectively, split into different sea-ice types indicated by colour. The respective bin sizes are 0.05 m and 5 kg m^{-3}.

dependence on other sea-ice properties and the fact that keels of ridges with high freeboard contain voids filled with sea water introduced non-linearity to this relationship. To avoid underestimating the density values near the lower and upper ends of the observed freeboard range and to increase the goodness of fit, we therefore fitted an exponential function to the full, along-track averaged sea-ice bulk density data set ($N = 2246$, Fig. 5.8). Least-squares fitting yielded a relationship of

$$\rho_i = 72.0 \times e^{-3.74 \times h_{fi}} + 881.8 \tag{5.7}$$

where sea-ice freeboard is in metres and sea-ice bulk density in kilograms per cubic metre. The resulting coefficient of determination (R^2) was 0.42 and RMSE was 15.2 kg m^{-3}. The fitted curve showed excellent agreement also with the inverse-variance weighted average densities of the 0.05 m freeboard bins resulting in $R^2 = 0.89$ and RMSE = 6.2 kg m^{-3}.

5.4 Discussion

We measure sea-ice bulk density indirectly based on (i) the direct measurements of sea-ice thickness, snow depth, and freeboard and (ii) the isostatic balance between the masses of snow, sea ice, and displaced sea water only assuming the densities of the snow layer and sea water. However, we measure the thickness of the sea ice layer and not its mass. Instead, we use sea-ice bulk density to relate sea-ice thickness to the displaced mass of sea water inherently by assuming a constant density of the entire sea-ice layer. However, in reality, the material composition of sea ice is not constant throughout the vertical column which complicates the attribution of bulk sea ice density values to physical properties such as porosity. Above the waterline, the density is lower than that of pure ice due to air incorporated in the pore spaces and to an increasing degree in MYI. Below the waterline, brine and sea water saturate the sea ice and increase the density above the pure ice density. Despite the indirect measurement method, we are able to detect a difference in FYI bulk density between 2017 and 2019 that can be linked to the high sea-ice deformation in 2017. The effect of deformed and unconsolidated sea-ice is often overlooked and needs the attention of the scientific community. Dedicated sea-ice porosity studies and extensive field measurement programs, such as the recent Multidisciplinary drifting Observatory for the Study of Arctic Climate (MOSAiC), will be able to shed more light on their effect and development.

5.4.1 Ice-type averaged sea-ice bulk density

Compared to A10, the average sea-ice bulk density estimates derived in this paper are larger by 11.8 kg m^{-3} ($\approx$ 1.3 %) for FYI and by 20.4 kg m^{-3} ($\approx$ 2.3 %) for MYI but still within the A10 uncertainties, albeit close to the upper limit. In general, our ice-type averaged bulk density estimates fall within the range of previous studies (Timco and Frederking, 1996). Reasons for the comparably high estimates are twofold. First, the A10 FYI density is representative only to level, undeformed ice whereas our estimate includes also deformed FYI. Alexandrov et al. (2010) used drill-hole measurements that were carried out in 3–5 locations, 150–200 m apart around each aircraft landing site on level ice. Sea-water inclusions within deformed and unconsolidated sea ice increase the bulk density. This is a likely reason contributing to the higher FYI bulk density especially in the 2017 data, given the increased deformation caused by the reversal of the Beaufort Gyre. Second, Alexandrov et al. (2010) calculated the MYI density as a weighted average between the layers above and below the waterline based on values from numerous literature sources but used a density of 550 kg m^{-3} for the upper layer which is significantly lower than the majority of the literature indicates (720–910 kg m^{-3} in Timco and Frederking (1996), 863–929 kg m^{-3} in Pustogvar and Kulyakhtin (2016)) and would correspond to an air-volume fraction of up to 40 %. When using the weighted average method in Alexandrov et al. (2010) but the density values from Timco and Frederking (1996) instead, we find a MYI density of 909 $\pm$ 28 kg m^{-3} that is closer to our estimate.

5.4.2 Uncertainties and limitations of the derived sea-ice bulk density

The effect of the uncertainties in the measured parameters and assumed sea-water and snow density values on the sea-ice bulk density was studied using Gaussian error propagation in Eq. (5.4). Single point measurements typically resulted in sea-ice bulk density uncertainties of approximately 70 kg m^{-3} and 35 kg m^{-3} for FYI and MYI, respectively. Other sources of error arise from the different length scales illustrated in Figs. 5.3 and 5.5. We are not able to resolve snow depth fully within the total thickness measurement given the comparably large footprint of the EM-Bird but we calculate it as an average of the snow depth measurements along a chord of the circular EM-Bird footprint. Due to the cross-track movement of the EM-Bird under the aircraft, the ground locations and the number of the snow depth measurements within the total thickness measurement vary slightly along the survey track but generally remain at eight to ten measurements close to the centre line. To ensure representative snow depth estimates, we require at least five valid snow depth measurements for each total thickness measurement, which translates into at least 50 % coverage along the chord. Errors may occur locally, e.g., at cross-track transition from a sea-ice floe to young ice in a newly refrozen lead as in the leftmost measurement points in Fig. 5.3, but we assume them to occur randomly and not cause systematic bias. However, uncertainties are reduced when averaged along-track over a length scale. Using the 800 m length scale, the resulting sea-ice bulk density uncertainty is generally less than 10 kg m^{-3} (Eq. (5.6)) but remain the highest for thin ice and low sea-ice freeboard where the relative uncertainties of the input parameters are the largest (see the size of the scatter points in Fig. 5.8). In turn, averaging over a length scale simplifies the natural variability of sea ice. Figure 5.5 shows how a single 25 km satellite grid cell can contain already several sea-ice types: level, deformed, FYI, SYI, and MYI. However, assigning the sea-ice types is limited by the spatial (12.5 km) and temporal (weekly) resolution of the NSIDC sea-ice age product, which we try to compensate with the additional thickness-based conditions (see Sect. 5.2.5.2). In addition, our measurements are confined to the western Arctic in early April and therefore, more measurements across the Arctic and the seasons are needed to evaluate the spatial and temporal variability of sea-ice bulk density.

5.4.3 Impact on sea-ice thickness retrievals

Assuming all the other parameters for the conversion of freeboard to thickness remain the same, the average sea-ice bulk density estimates derived in this paper would result in 12.4 % and 16.7 % larger sea-ice thickness values for FYI and MYI, respectively, in comparison to A10. The effect is larger for thicker ice, for which snow depth plays a proportionally less important role. Therefore, improving especially the MYI bulk density is important to derive accurate time series of sea-ice thickness and volume, as in the past, thicker MYI represented a larger fraction of the Arctic sea-ice cover. Kwok and Cunningham (2015) recognised the possibility of varying MYI density between the recent younger MYI and older MYI of the previous decades and discussed the impact of MYI density on sea-ice thickness and volume.

Moreover, a potentially increasing degree of deformation may lead to a bias in the time series, as satellites underestimate sea-ice draft of deformed ice as shown by Belter et al. (2020) and further discussed by Khvorostovsky et al. (2020). Deformed and unconsolidated sea-ice has an increased bulk density due to sea-water inclusions and thus, using a typical density of consolidated level sea-ice for deriving sea-ice thickness from satellite data will eventually lead to an underestimation. Given the thinner and younger sea-ice cover together with observed increase in sea-ice drift speed and deformation (Rampal et al., 2009; Spreen et al., 2011), there is a likely premise for systematic underestimation by current parametrisations of sea-ice density in regions where and at times when sea ice is deformed. A full impact assessment of the sea-ice bulk density parametrisation on decadal sea-ice thickness data record is a logical next step but beyond the scope of this paper.

5.4.4 Outlook

To represent sea-ice bulk density range as a functional relationship to a parameter observable from space rather than fixed values based on sea-ice type classification, we parametrised sea-ice bulk density using sea-ice freeboard and obtained a significant correlation. Opting for an exponential function instead of linear was beneficial for ensuring a better fit, capturing the high bulk density values at low freeboard values, and avoiding linear decrease to possibly unrepresentative and unphysical values at high freeboards. Parametrisation in Eq. (5.7) sets the limits of bulk density to 953.8 kg m^{-3} at zero sea-ice freeboard and approaching 881.8 kg m^{-3} at high freeboards.

Figure 5.9 shows the parametrisation in Eq. (5.7) applied to the AWI Level-3 Collocated CryoSat-2 Sea Ice Product (Hendricks and Ricker, 2020) from the winter 2018/2019 converting the monthly gridded sea-ice freeboard to sea-ice density. The resulting sea-ice density distribution had a smoother transition between ice types compared to the current ice-type dependent density classification of the retrieval algorithm. Difference between the density parametrised with Eq. (5.7) and A10 was positive overall during the winter except in the Central Arctic Ocean and locally in the Fram and Bering Straits in spring. The density difference was the largest on MYI in proximity to FYI but decreased toward spring.

Only less than 3 % of the airborne data set has a sea-ice freeboard value larger than 0.5 m with considerable spread in bulk density values and thus, introducing uncertainty to the parametrisation at high freeboard values. Constraining the parametrisation at high freeboards would require more data in deformed and multi-year sea-ice environments. However, that needs to coincide with a sufficient amount of open leads to ensure accurate conversion of surface elevations to freeboard from the ALS. With the limitations of the current method, it is also not feasible to investigate cases of negative sea-ice freeboard due to the possible presence of liquid water and altered dielectric properties affecting the retrieval of snow depth.

Our parametrisation improves upon the previous formulations of sea-ice density given the significantly larger number of data points, larger areal coverage, the variety of ice types

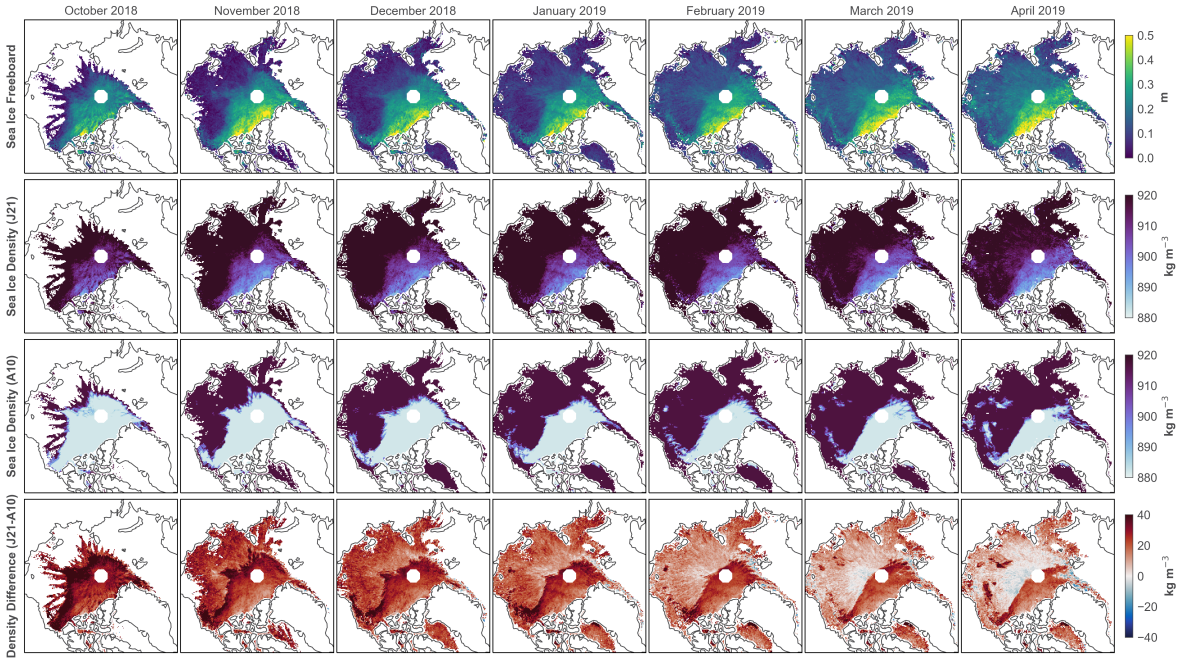

Figure 5.9. Sea-ice density parametrisation applied to the monthly, gridded AWI CryoSat-2 Sea Ice Product (Hendricks and Ricker, 2020) for the winter 2018/2019. The rows show sea-ice freeboard, sea-ice density derived using Eq. (5.7) (J21), sea-ice density currently used in the product (A10), and the difference between the two (J21−A10). The columns from left to right show monthly means from October 2018 to April 2019.

including deformed sea ice, and the choice of predictor variable it is based on. Kovacs (1997) based his analysis on 17 FYI and 4 MYI sea-ice cores from the Beaufort Sea and derived a floe-thickness based non-linear parametrisation of $\rho_i = 936.3 - 18h_i^{0.5}$. Ackley et al. (1976) used drill-hole measurements from 400 m of profile lines in the Beaufort Sea to derive $\rho_i = -194h'_f + 974$ where $h'_f = h_{fi} + \frac{\bar{\rho}_s}{\bar{\rho}_i} h_s \leq 1.05$ m is effective freeboard and the overbar denotes average density on the floe. The parameters needed for those formulations cannot be directly observed from space, or in the case of effective freeboard not even with a single in situ measurement, which makes them difficult to apply. Demonstrated in Fig. 5.9, our freeboard-based parametrisation has potential for future applications in satellite altimetry. While we acknowledge that, due to the variability in snow mass and sea-ice thickness, our parametrisation may not be applicable on sub-kilometre scales as reflected by the scatter in Fig. 5.8, we think that a sea-ice density parametrisation is a significant improvement upon a single value or fixed values based on ice type. In this paper, we decided to adopt a single-predictor parametrisation for the sake of simplicity. However, for future studies it could be worthwhile, e.g., to apply machine learning algorithms to the full parameter space to discover possible multi-variable relationships. Given the effect of sea-ice deformation on bulk density, including sea-ice surface roughness, a multi-variable approach could explain more of the variability.

5.5 Conclusions

The unique, collocated, multi-sensor measurements of the Arctic sea ice from the AWI IceBird campaigns allow us not only to observe sea-ice thickness, freeboard, and snow depth in high-resolution on regional scales, but also for the first time to estimate sea-ice bulk densities of different ice types from airborne measurements. Despite measuring the sea-ice bulk density indirectly by deriving it from other measurements, we are able to capture the effects of deformed ice on FYI bulk density. In the current Arctic, the average FYI and MYI bulk densities are higher than and do not differ as much as earlier studies suggested partly due to including deformed ice in the analysis. Alexandrov et al. (2010) derived a difference of 34.7 kg m^{-3} whereas our measurements show only 26.1 kg m^{-3} providing yet one more indication and consequence that the Arctic sea-ice cover is getting younger. Satellite altimetry sea-ice thickness retrieval algorithms need to adapt to these changes in order to capture the sea-ice thickness and volume accurately, and to account for changes over the satellite radar altimetry record spanning almost three decades. Taking advantage of the abundant measurements collected over different sea-ice types during two late-winter airborne campaigns, we are able to provide a parametrisation of sea-ice bulk density using sea-ice freeboard. The single-variable exponential function presented here yields a smaller RMSE than the uncertainty of density values fixed by sea-ice type currently in use in large extent. With potential applications in sea-ice thickness retrieval from satellite radar altimetry, a density parametrisation alone does not completely solve the uncertainty problem in the freeboard-to-thickness conversion. Together with improved knowledge of snow loading, they provide a path to decrease the uncertainty in observing sea-ice thickness and volume where the recent (CryoSat-2/ICESat-2 orbit resonance) and future (CRISTAL mission) advances in dual-altimetry will play a key role. In situ and airborne multi-sensor observations of various sea-ice parameters across the seasons will remain important to validate new approaches.

Acknowledgements

The authors thank the crews of *Polar5* and *6*, Kenn Borek Air, AWI technicians and logistics, Environment and Climate Change Canada (ECCC), and Canadian Forces Station (CFS) Alert, who helped at various stages of the data collection. Veit Helm is acknowledged for post-processing the surface temperature data.

Data availability

A collocated sea-ice parameter data product, including measured total thickness, snow freeboard, snow depth, and surface temperature and derived parameters such as sea-ice thickness, sea-ice freeboard, and sea-ice bulk density, is submitted to and soon available on PANGAEA (https://www.pangaea.de/). Releasing lower processing-level data is under preparation. Total thickness measurements during the PAMARCMIP2017 campaign are already available at https://doi.org/10.1594/PANGAEA.924848. The EASE-Grid Sea Ice Age, Version 4, is available in the NASA National Snow and Ice Data Center Distributed Active Archive Center: https://doi.org/10.5067/UTAV7490FEPB. The Canadian Ice Service Arctic Regional Sea Ice Charts in SIGRID-3 Format, Version 1, are available in the NSIDC: National Snow and Ice Data Center: https://doi.org/10.7265/N51V5BW9. The AWI Level-3 Collocated CryoSat-2 Sea Ice Product is available here: ftp://ftp.awi.de/sea_ice/product/cryosat2/v2p3/.

Chapter 6

Conclusion and outlook

Snow is tightly coupled to the sea-ice system, even to the extent that for many people the term *sea ice* actually means the combination of the ice and snow layers (Sturm and Massom, 2017). It may have led to the fact that snow on sea ice, the processes it governs, and their importance to the sea-ice and climate systems have long been overlooked. Snow remains as one of the big unknowns in the polar regions introducing a key knowledge gap and increased uncertainty in our current understanding (Webster et al., 2018; Meredith et al., 2019). On the global scale, spatially and temporally representative, year-round, and timely observations of snow depth on sea ice still do not exist today. This complicates various applications, such as modelling but most importantly using satellite altimetry to monitor and evaluate how stable the polar sea-ice covers are. Sea-ice parameters such as extent, thickness, and volume have become iconic indicators of the global climate change (e.g., Druckenmiller et al., 2021), but the unknown characteristics of the snow and sea-ice layers directly translate into uncertainty of the decadal satellite data record (Giles et al., 2007). This dissertation works toward enabling enhanced observations of snow depth on sea ice which is an important piece of the jigsaw puzzle in the polar regions. It allows improving the observations of other sea-ice parameters and even uncovering ones that we have not been able to observe directly so far.

In the beginning of this dissertation, four objectives were set for the path toward the overarching goal of full characterisation of the snow and sea-ice layers. The **first objective** was to test the theory of retrieving snow depth by using radars at two different frequencies and investigating their microwave penetration into the snow cover. The objective is addressed in **Chapter 3** by analysing field experiments using off-the-shelf pulsed radars operating at C (6 GHz) and K (26 GHz) band, also to tackle an additional objective to find out if commercial radars are feasible for the task. While previous studies using ground-based radars at frequencies up to and including the Ku band ($\leq$ 18 GHz) are abundant, reports of field measurements with higher-frequency radars are very scarce in literature. The results showed that the dominant scattering horizon for the K band was the air–snow interface as expected due to the smaller wavelength. Meanwhile, the C band microwaves penetrated closer to the snow–sea-ice interface potentially enabling snow depth retrieval only in 39 % of the cases and only on FYI (Fig. 3.3). The microwave penetration and its analysis was hampered by morphological

features of the snow cover, relatively high temperatures close to the freezing point during the observation period in May, and lacking measurements of snow wetness to confirm the presence of liquid water. The results partly confirm findings from previous studies but remain inconclusive as inconsistent behaviour related to, e.g., snow basal salinity and measurement height was observed and no purpose-built radar was deployed alongside the commercial radars. While off-the-shelf pulsed radars operating at two frequencies may not be practical for snow depth retrieval based on this study, they could prove useful in autonomous monitoring of snow and sea-ice backscatter behaviour in the harsh Arctic environment.

The next step was to upscale the snow depth acquisition to a larger spatial scale and higher resolution using an airborne platform. The **second objective** of this dissertation was to include a high-sensitivity, high-resolution FMCW radar to the airborne AWI IceBird sea-ice sensor configuration. Reaching this objective meant establishing a processing chain for retrieving snow depth from the radar data, evaluating the radar performance at the low altitude, and demonstrating the associated improvements over previous acquisitions — these are described in **Chapter 4**. As the main result, the AWI IceBird surveys are now capable to discriminate between the snow and sea-ice layers with the addition of the ultrawideband 2–18 GHz FMCW radar system. Radar data calibration through coherent noise removal and system response deconvolution successfully and significantly improved the data quality by reducing both the noise level and the side lobes (Fig. 4.5). A new snow depth retrieval algorithm based on signal peakiness was developed to provide precise estimates of snow depth over different ice types and survey altitudes as well as when the air–snow interface is the main scattering horizon. A validation exercise over a two-dimensional TLS-derived snow depth field on level, landfast FYI revealed a mean bias of 0.86 cm that is below the radar sensor resolution and the estimated accuracy of the TLS snow depths (Fig. 4.8). Comparison of long overlapping segments at a high altitude of 1500 ft, comparable to previous acquisitions like NASA Operation IceBridge (OIB), and at a low altitude of 200 ft showed good consistency in the snow depth data and better overall performance than an existing wavelet-based algorithm that suffered from both overestimation and underestimation of snow depth (Figs. 4.9 & 4.10). At the low altitude, the theoretical smooth surface radar footprint is less than 10 % in size compared to previous high-altitude acquisitions, which results in better spatial resolution and decreased effect of off-nadir sea-ice surface features, and the usage of the complete multi-sensor configuration is enabled. The airborne radar-derived snow depth data set of this study is an important, independent contribution to this undersampled parameter related to sea ice. It spans three late-winter seasons in 2017–2019 in the western Arctic Ocean including areas in the Beaufort Sea in 2019 that were not covered by the annual OIB campaign.

In **Chapter 5**, I approach the **third objective**, to take advantage of the unique multi-sensor configuration of the AWI IceBird campaigns. Collocating the snow depth derived in Chapter 4 with coincident total thickness measurements from the EM-Bird and snow freeboard from the ALS allows tracking the locations of the air–snow, snow–sea-ice, and sea-ice–water interfaces along the airborne survey paths. During the campaigns in 2017 and

2019, the required instrument combination was operated nominally on a total of nine survey flights and more than 3000 km over different sea-ice types. Assuming values for snow and sea-water densities and that the sea-ice cover is in isostatic equilibrium, the collocated and high-resolution thickness and freeboard profiles can be used to derive sea-ice bulk density (Fig. 5.5). Such estimates are needed to evaluate the current state of sea ice as there is a lack of temporally and spatially representative sea-ice density measurements and no up-to-date climatology for sea-ice density is available. Sea-ice density also cannot be directly observed by satellites. Ice-type averaged results of 928.5 ± 16.4 kg m^{-3} for FYI and 902.4 ± 19.4 kg m^{-3} for MYI showed bulk density values that are respectively 11.8 kg m^{-3} and 20.4 kg m^{-3} higher than and do not differ as much as the widely used values by Alexandrov et al. (2010) (Table 5.3, Fig. 5.6). This is partly due to the fact that since the 1980s, when the field measurements in Alexandrov et al. (2010) were carried out, the Arctic sea-ice cover has become younger driven by the warming climate. Additionally, the FYI density in Alexandrov et al. (2010) is valid only for level, consolidated, and undeformed ice and the MYI density is based on average values from literature whereas estimates presented in this study also include deformed and unconsolidated FYI and timely measurements of MYI. This kind of simultaneous, multi-instrument observation of the snow and sea-ice layer thicknesses and sea-ice density opens a door for true mass balance measurements of sea ice. The results also suggest that satellite altimetry retrieval algorithms should be adapted to changes in sea-ice density.

Also in **Chapter 5**, the **fourth objective**, parametrising sea-ice bulk density, was met by fitting a negative-exponential model to the unique data set using sea-ice freeboard as the predictor variable: $\rho_i = 72.0 \times e^{-3.74 \times h_{fi}} + 881.8$ (Fig. 5.8). The parametrisation has a coefficient of determination of 0.42 and an RMSE of 15.2 kg m^{-3}, which is smaller than the uncertainty in the density values of Alexandrov et al. (2010). Previous parametrisations by Ackley et al. (1976) and Kovacs (1997) are also single-variable formulations but based on considerably smaller data sets, both in number of observations and in regional coverage, that are also up to half a century old by now. Moreover, the choice of predictor variables, sea-ice thickness and effective freeboard, has made the parametrisations cumbersome to use as neither of the two parameters can be directly observed from space. In contrast, our parametrisation is based on sea-ice freeboard that can be measured by satellite radar altimeters, which gives potential for large impact and widespread use, e.g., upscaling sea-ice bulk density to Arctic-wide and enhancing sea-ice thickness and volume retrievals from satellite altimetry data.

The **ultimate goal** of full characterisation of the snow and sea-ice layers has not been completely reached in this dissertation, but important advancing steps have been taken towards it. Previously, the airborne sea-ice measurements on the AWI IceBird campaigns were unable to discriminate between the snow and sea-ice layers, but by integrating an ultrawideband FMCW radar to the instrument configuration, it is now possible to track the locations of all three interfaces bounding the snow–sea-ice system. With the respective thicknesses of the snow and sea-ice layers, freeboard information, and the assumptions of isostatic equilib-

rium and snow density, it is also possible to derive bulk density estimates for the sea-ice layer along the survey tracks. Previously, sea-ice density measurements have required laborious coring, cutting out pieces of ice, or drilling that quickly limits the number of samples.

The results presented in this dissertation suffer from joint limitations: the observations were constrained to one season only, late-winter, and concentrated on the western Arctic Ocean. In addition to more observations in undersampled seasons and regions to investigate both seasonal-to-interannual and regional variability, more measurements are needed also on the ground across a full variety of surface types for validation purposes. For example, airborne campaigns are often prone to weather constraints, which within the scope of this dissertation led to a realisation of one validation exercise for snow depth retrieval on level and landfast FYI while more opportunities were planned. Validating the approaches described in the studies here in different sea-ice environments would result in decreasing the associated uncertainties.

Outlook

It is common for any kind of remote sensing measurement, as is the case also with the studies presented in this dissertation, that ground truth data is required for validation and correct interpretation. For radar remote sensing of snow on sea ice, the ground measurements should include not only two-dimensional surveys of snow depth and detailed studies on the physical properties of snow, but also coincident measurements with ground-based or near-surface (e.g., on unmanned aerial vehicles or drones) multi-band microwave radars across a variety of surface types, environmental conditions, and seasons. The MOSAiC drift expedition in 2019–2020 included an extensive on-ice remote sensing program with a large number of both passive and active microwave instruments (Fig. 6.1). The associated data sets will be vital in improving our understanding of the radar signal interaction with the snow-covered sea ice. Airborne measurements continue being important to validate data from satellites and therefore, they should be continued but also expanded both in space and in time. Currently the FYI-dominated eastern Arctic Ocean and seasons other than late-winter are undersampled, which limits the validation opportunities (e.g., Rostosky et al., 2018).

Methods and approaches described in this dissertation should be further developed as identifying the air–snow interface correctly from the radar data remains challenging due to the small dielectric contrast (MacGregor et al., 2021). The new snow depth retrieval algorithm described in Chapter 4 could benefit from incorporating and aligning the surface elevation data from the ALS to aid tracking the correct snow surface (e.g., Fig. 7 in Kwok et al., 2011). In conjunction with that, a detailed study about identifying the exact location of off-nadir targets from the approximately 60 m wide ALS swath would be beneficial for further quantifying the improvements of the small radar footprint (e.g., Fig. 5 in Newman et al., 2014). Another option to enhance the detection of the snow surface would be to explore the possibility to assign retracker algorithm parameters and thresholds dynamically according to surface type or depending on the footprint-scale surface roughness characteristics, which

Figure 6.1. (Left) The new, ground-based, fully polarimetric Ku and Ka band radar described in Stroeve et al. (2020) was deployed on the MOSAiC expedition to investigate the influence on snow properties on sea-ice thickness retrievals and the potential for snow depth measurements. (Right) The unique collection of ground-based remote sensing instruments on the MOSAiC expedition even aroused the curiosity of the local wildlife. This particular individual only slightly adjusted the incidence angle of one sensor and politely refrained from tampering the measurement area. Photo credits: Alfred Wegener Institute / Stefan Hendricks (left) and Remote Sensing Camera (right) (CC-BY 4.0).

is already suggested by modelling studies (Kurtz et al., 2014; Landy et al., 2019, 2020). In addition, while the sea-ice density parametrisation suggested in Chapter 5 was intentionally kept simple following the single-predictor approach of Ackley et al. (1976) and Kovacs (1997), it would be worthwhile to explore possible improvements through multivariate regression, machine learning approaches, and dividing the data set into several ice types (FYI, MYI, level, and deformed) instead of a single inclusive formulation.

The radar data collected in the scope of this dissertation are still partly unexplored and offers potential for further studies. So far, the quad-polarisation or fully polarimetric capabilities of the airborne FMCW radar have not been exploited. The four possible channel combinations could reveal more information about snow on sea ice. Furthermore, the radar has been used only as an altimeter but the information about the total backscatter is also available for studying radar backscatter from different snow and sea-ice surfaces.

In this dissertation, the focus has been on the snow-covered sea ice located in the Arctic in late winter. The counterparts of the AWI IceBird winter campaigns are the airborne surveys conducted in summer (July–September) focused on monitoring the sea-ice thickness in the vicinity of the Fram Strait (Belter et al., 2021). In principle, it is possible to apply a simplified version of the methodology introduced in Chapter 5 to the summer data to derive bulk density for the melting summer sea ice with certain assumptions. The ultrawideband FMCW radar is not part of the instrument configuration in the summer campaigns due to the wet sea-ice surface and general lack of snow at the end of the melt season as most of it has melted away. Therefore, the combination of sea-ice thickness measurements from the EM-Bird and freeboard information from the ALS is sufficient for deriving sea-ice density estimates assuming the absence of the snow layer. The summer campaign time series extends back to 2010 and thus, it would enable a study of seasonal and interannual variability of sea-

ice density. Another opportunity for a further IceBird study would be to shift the focus from seasons to location. Throughout the duration of the NASA OIB campaign in 2009–2019, airborne ultrawideband FMCW radars similar to the one now integrated to the AWI IceBird have been annually operated over the Antarctic sea-ice cover (Kwok and Maksym, 2014; Kwok and Kacimi, 2018; MacGregor et al., 2021). The snow–sea-ice system in the Southern Ocean offers different kind of challenges: the snow cover is generally thicker and has more complex structure due to frequent flooding and melt events (Sturm and Massom, 2017) and a layer of platelet ice underneath the consolidated sea ice often exists near ice shelves (Hoppmann et al., 2020; Haas et al., 2021). An instrument configuration comparable to the current capabilities of AWI IceBird has not been flown over Antarctic sea ice thus far. Testing the multi-instrument observation approach of Chapter 5 would be first of its kind there and offer a glimpse to the differences in sea-ice and snow characteristics between the two polar regions.

There are two logical next steps to apply the findings of this dissertation. First, the unique data set created in Chapter 5 enables a detailed assessment of the freeboard-to-thickness conversion and the proposed sea-ice density parametrisation in satellite altimetry retrievals of sea-ice thickness. The campaigns in 2017 and 2019 had several dedicated surveys following the ground tracks of AltiKa, Sentinel-3A, and ICESat-2 satellite altimeters (Table 4.2). The full airborne data set containing all flights can be compared against a collection of CryoSat-2 satellite altimeter orbits from the corresponding campaign period of each year. The second step is to upscale those findings to the Arctic-wide satellite data and finally to the decadal sea-ice thickness data record.

Snow depth and sea-ice density are the biggest unknowns in the freeboard-to-thickness conversion of satellite altimetry data. Getting them right is crucial for improving Arctic-wide sea-ice thickness and volume retrievals and resolving the trends in the satellite altimetry data record that reaches 30 years in 2023. Accurate products of snow depth and sea-ice thickness are needed not only for monitoring the current state of these important climate parameters but also to run various climate models for projecting the future changes in the global climate (Barber et al., 2017; Meredith et al., 2019; SIMIP Community, 2020).

Appendix A

Appendix to Chapter 3

This supporting information lists the figures of detailed snow studies not shown in Chapter 3.

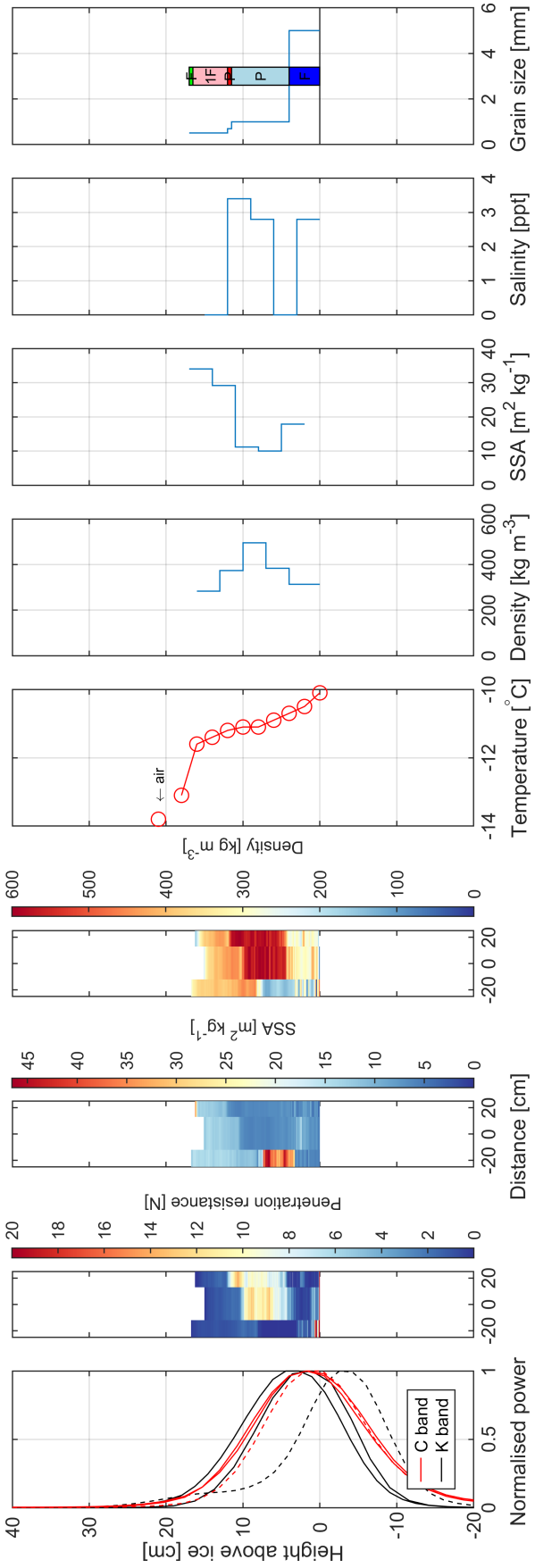

Figure A.1. Snow pit FYI buoy on 12 May 2018. The first panel shows the normalised radar returns for C (red) and K bands (black) and for the lower (solid) and higher (dashed) measurement height. The next three panels show the SnowMicroPen measurements across the radar footprint, where zero distance indicates directly under the radar at the middle of the instrument stand and positive distance is to the right. Remaining panels show the standard snow pit measurements. SSA stands for specific surface area. Letter code for hand hardness: very soft, F (fist); soft, 4F (4 fingers); medium, 1F (1 finger); hard, P (pencil); very hard, K (knife blade); ice, I (ice). Colour code for snow grain type: precipitation particles, lime; decomposing and fragmented precipitation particles, forest green; rounded grains, light pink, faceted crystals, light blue; depth hoar, blue; melt forms, red; ice formations, cyan (Fierz et al., 2009).

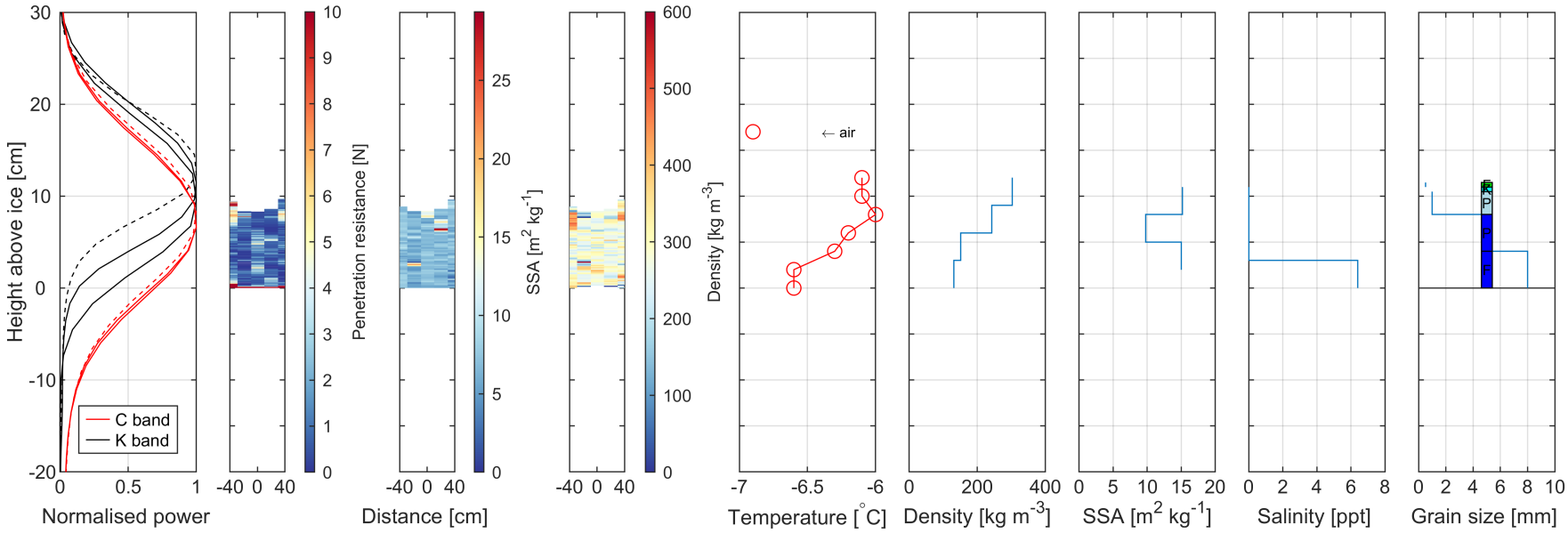

Figure A.2. Snow pit FYI OIB on 16 May 2018. The first panel shows the normalised radar returns for C (red) and K bands (black) and for the lower (solid) and higher (dashed) measurement height. The next three panels show the SnowMicroPen measurements across the radar footprint, where zero distance indicates directly under the radar at the middle of the instrument stand and positive distance is to the right. Remaining panels show the standard snow pit measurements. SSA stands for specific surface area. Letter code for hand hardness: very soft, F (fist); soft, 4F (4 fingers); medium, 1F (1 finger); hard, P (pencil); very hard, K (knife blade); ice, I (ice). Colour code for snow grain type: precipitation particles, lime; decomposing and fragmented precipitation particles, forest green; rounded grains, light pink, faceted crystals, light blue; depth hoar, blue; melt forms, red; ice formations, cyan (Fierz et al., 2009).

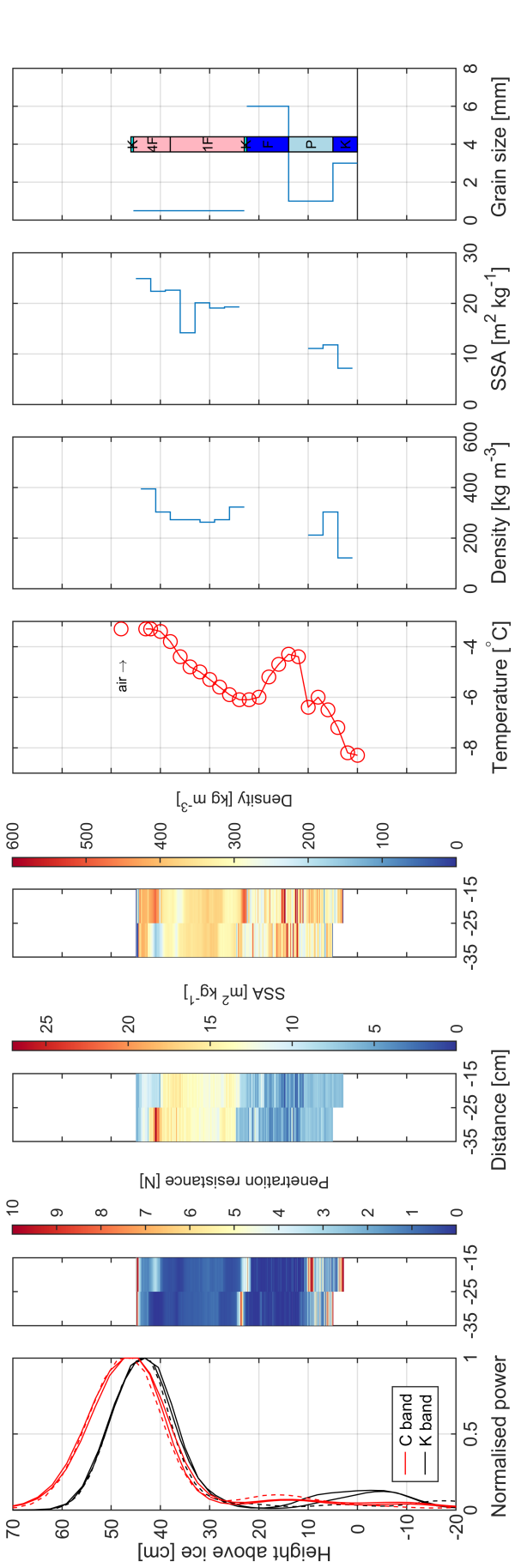

Figure A.3. Snow pit MYI OIB on 18 May 2018. The first panel shows the normalised radar returns for C (red) and K bands (black) and for the lower (solid) and higher (dashed) measurement height. The next three panels show the SnowMicroPen measurements across the radar footprint, where zero distance indicates directly under the radar at the middle of the instrument stand and positive distance is to the right. Due to a data saving failure, only the two leftmost SMP profiles were recorded. Remaining panels show the standard snow pit measurements. SSA stands for specific surface area. Letter code for hand hardness: very soft, F (fist); soft, 4F (4 fingers); medium, 1F (1 finger); hard, P (pencil); very hard, K (knife blade); ice, I (ice). Colour code for snow grain type: precipitation particles, lime; decomposing and fragmented precipitation particles, forest green; rounded grains, light pink; faceted crystals, light blue; depth hoar, blue; melt forms, red; ice formations, cyan (Fierz et al., 2009). The salinity profile is not shown, because all MYI snow pits had zero salinity.

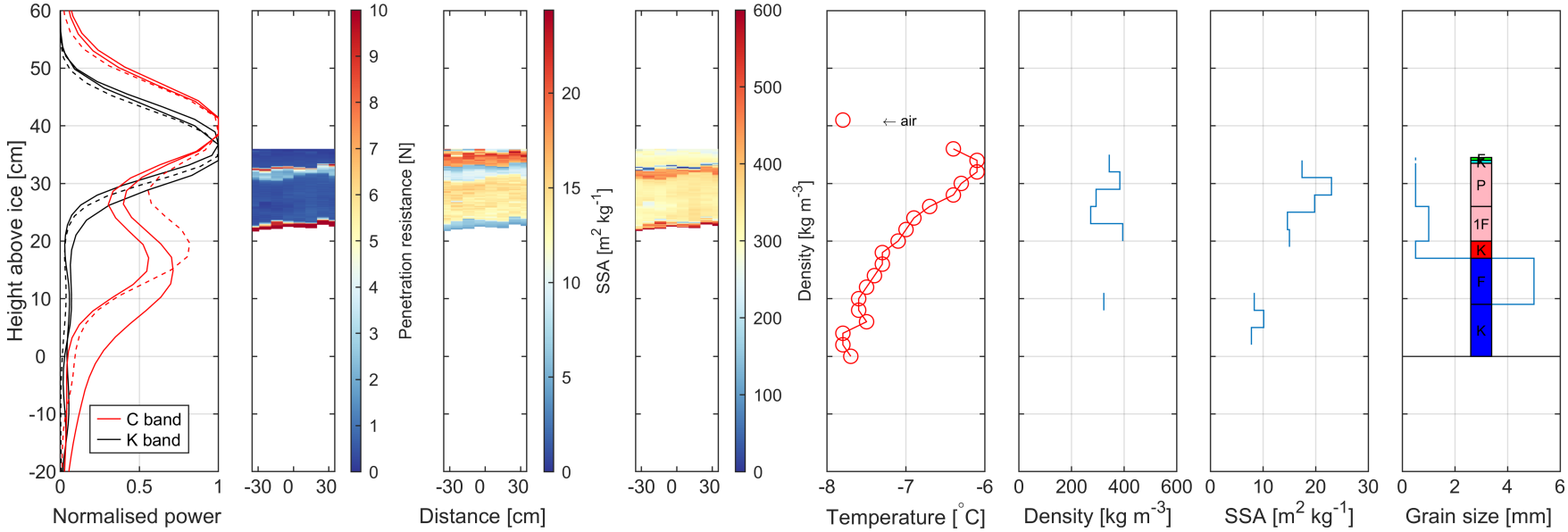

Figure A.4. Snow pit MYI OIB floe N on 21 May 2018. The first panel shows the normalised radar returns for C (red) and K bands (black) and for the lower (solid) and higher (dashed) measurement height. The next three panels show the SnowMicroPen (SMP) measurements across the radar footprint, where zero distance indicates directly under the radar at the middle of the instrument stand and positive distance is to the right. The SMP could not penetrate the melt-freeze layer at approximately 20 cm above the sea-ice surface (maximum power threshold). Remaining panels show the standard snow pit measurements. SSA stands for specific surface area. Letter code for hand hardness: very soft, F (fist); soft, 4F (4 fingers); medium, 1F (1 finger); hard, P (pencil); very hard, K (knife blade); ice, I (ice). Colour code for snow grain type: precipitation particles, lime; decomposing and fragmented precipitation particles, forest green; rounded grains, light pink, faceted crystals, light blue; depth hoar, blue; melt forms, red; ice formations, cyan (Fierz et al., 2009). The salinity profile is not shown, because all MYI snow pits had zero salinity.

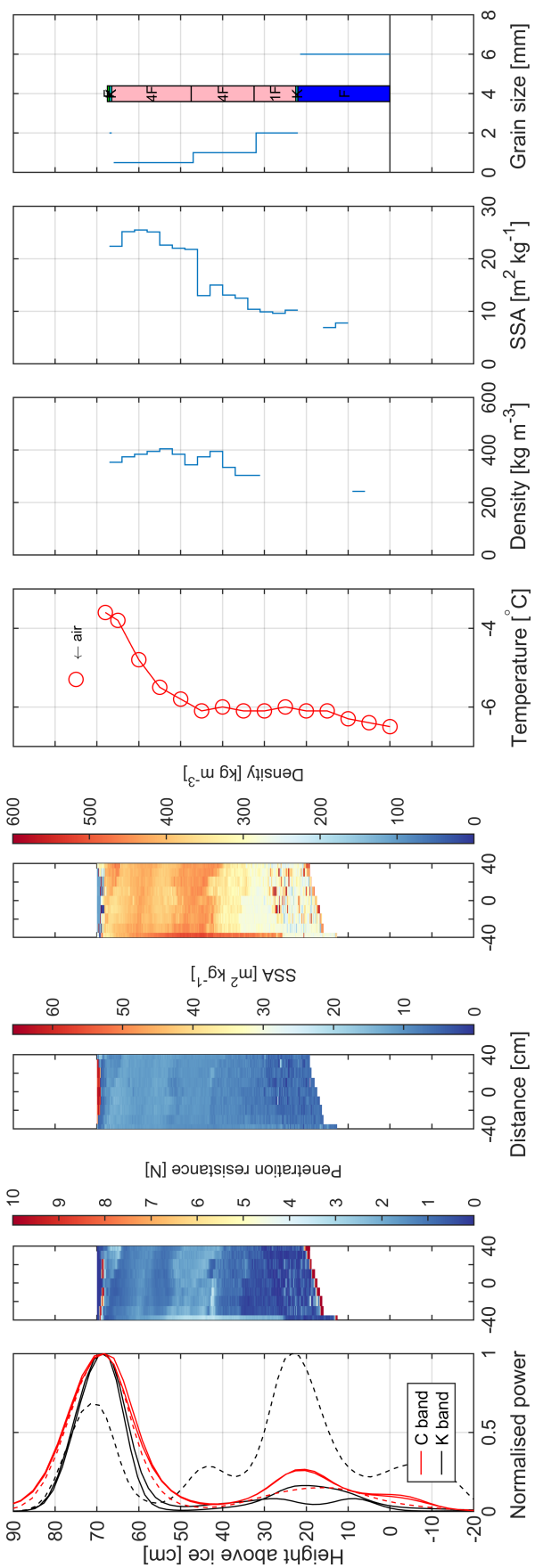

Figure A.5. Snow pit MYI OIB floe S on 21 May 2018. The first panel shows the normalised radar returns for C (red) and K bands (black) and for the lower (solid) and higher (dashed) measurement height. The next three panels show the SnowMicroPen (SMP) measurements across the radar footprint, where zero distance indicates directly under the radar at the middle of the instrument stand and positive distance is to the right. The SMP could not penetrate the ice lens at 15–20 cm above the sea-ice surface (maximum power threshold). Remaining panels show the standard snow pit measurements. SSA stands for specific surface area. Letter code for hand hardness: very soft, F (fist); soft, 4F (4 fingers); medium, 1F (1 finger); hard, P (pencil); very hard, K (knife blade); ice, I (ice). Colour code for snow grain type: precipitation particles, lime; decomposing and fragmented precipitation particles, forest green; rounded grains, light pink, faceted crystals, light blue; depth hoar, blue; melt forms, red; ice formations, cyan (Fierz et al., 2009). The salinity profile is not shown, because all MYI snow pits had zero salinity.

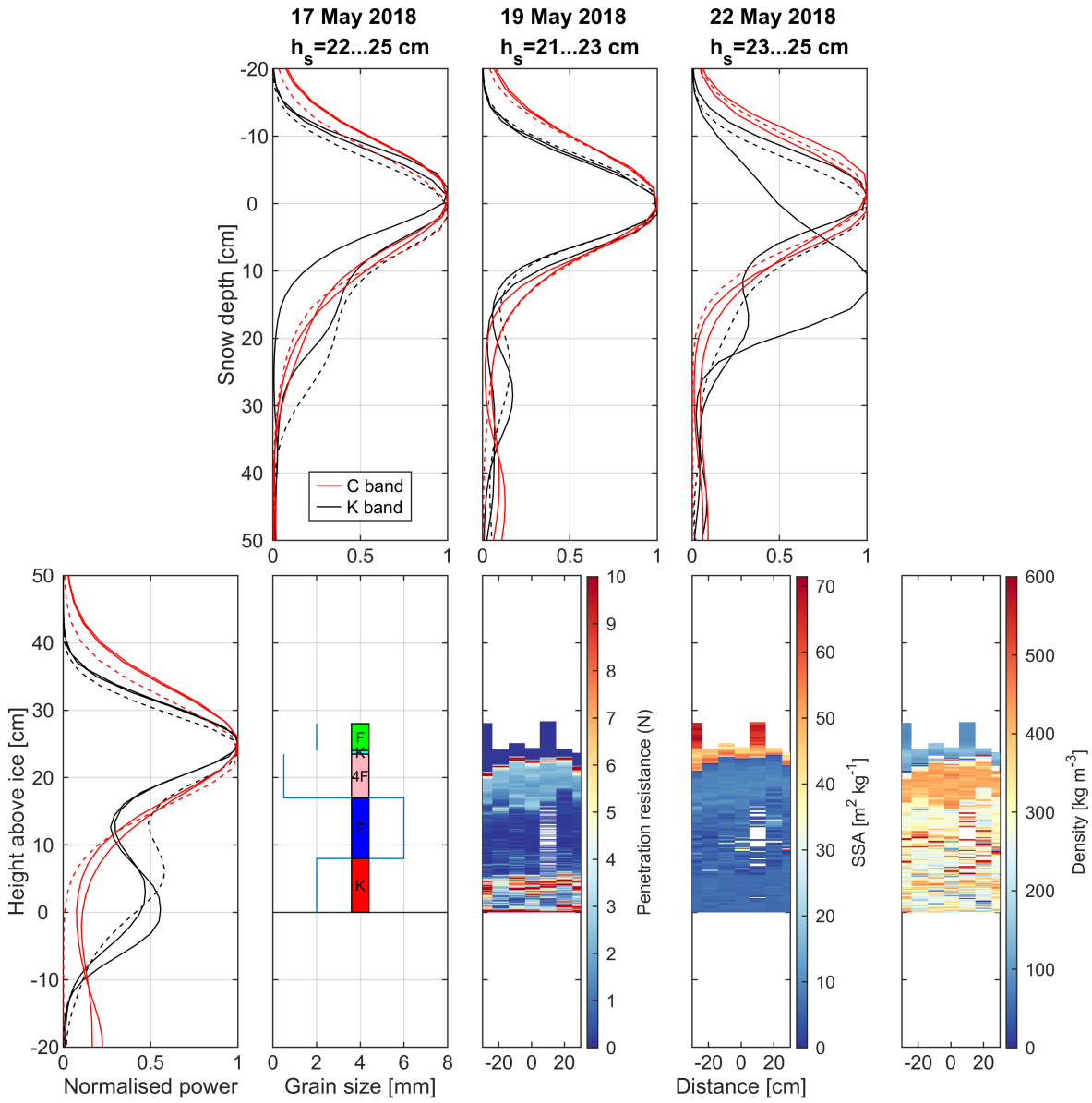

Figure A.6. Measurements at the study location MYI temporal. (Top) Repeated C (red) and K band (black) radar measurements for the lower (solid) and higher (dashed) measurement height between 17 and 22 May 2018 without detailed snow pit measurements. Note that the vertical axis is normalised to the snow surface and converted into snow depth. Range of snow depth values probed under the radar are indicated above each panel. (Bottom) Radar measurements on 24 May 2018 followed by stratigraphy and penetrometer measurements. Note that the vertical axis is now normalised to the ice surface. Letter code for hand hardness: very soft, F (fist); soft, 4F (4 fingers); medium, 1F (1 finger); hard, P (pencil); very hard, K (knife blade); ice, I (ice). Colour code for snow grain type: precipitation particles, lime; decomposing and fragmented precipitation particles, forest green; rounded grains, light pink, faceted crystals, light blue; depth hoar, blue; melt forms, red; ice formations, cyan (Fierz et al., 2009).

Appendix B

Data sets and other publications

Data sets

This dissertation has resulted in publication and submission of several data sets that are listed in the following subsections.

Snow depth related to Chapter 4

- **Jutila, A.**, King, J., Ricker, R., Hendricks, S., Helm, V., Binder, T., Herber, A.: **Airborne snow depth on sea ice during the PAMARCMIP2017 campaign in the Arctic Ocean, Version 1**, *PANGAEA*, https://doi.org/10.1594/PANGAEA.932668, 2021.

- **Jutila, A.**, King, J., Ricker, R., Hendricks, S., Helm, V., Binder, T.: **Airborne high-altitude snow depth on sea ice during aircraft flight P6_211_RESURV79_2018_1804100301, Version 1**, *PANGAEA*, https://doi.org/10.1594/PANGAEA.932702, 2021.

- **Jutila, A.**, King, J., Ricker, R., Hendricks, S., Helm, V., Binder, T., Haas, C.: **Airborne snow depth on sea ice during the IceBird Winter 2019 campaign in the Arctic Ocean, Version 1**, *PANGAEA*, https://doi.org/10.1594/PANGAEA.932790, 2021.

Sea-ice parameters related to Chapter 5

- **Jutila, A.**, Hendricks, S., Ricker, R., von Albedyll, L., Haas, C.: **Airborne sea ice parameters during the PAMARCMIP2017 campaign in the Arctic Ocean, Version 1**, *PANGAEA*, https://doi.pangaea.de/10.1594/PANGAEA.933883, in review, 2021.

- **Jutila, A.**, Hendricks, S., Ricker, R., von Albedyll, L., Haas, C.: **Airborne sea ice parameters during the IceBird Winter 2019 campaign in the Arctic Ocean, Version 1**, *PANGAEA*, https://doi.pangaea.de/10.1594/PANGAEA.933912, in review, 2021.

Other publications

This section presents publications that I co-authored during this dissertation.

- Lange, B. A., Haas, C., Charette, J., Katlein, C., Campbell, K., Duerksen, S., Coupel, P., Anhaus, P., **Jutila, A.**, Tremblay, P. O. G., Carlyle, C. G. and Michel, C.: **Contrasting Ice Algae and Snow-Dependent Irradiance Relationships Between First-Year and Multiyear Sea Ice**, *Geophysical Research Letters*, 46 (19), 10834–10843, https://doi.org/10.1029/2019GL082873, 2019.

- Anhaus, P., Katlein, C., Nicolaus, M., Arndt, S., **Jutila, A.**, and Haas, C.: **Snow Depth Retrieval on Arctic Sea Ice Using Under-Ice Hyperspectral Radiation Measurements**, *under review at Frontiers in Earth Science*, 2021.

These two studies investigated the under-ice light field using a remotely operated underwater vehicle (ROV) and how the transmitted radiation coupled with snow depth and bottom-ice chlorophyll *a* (chl *a*) during the 2018 Multidisciplinary Arctic Program — Last Ice in the Lincoln Sea. I participated in the field campaign in May 2018 by assisting in the ROV surveys and collecting snow depth and sea-ice thickness data used in these studies. I contributed to the writing and editing of the manuscripts.

- Katlein, C., Mohrholz, V., Sheikin, I., Itkin, P., Divine, D. V., Stroeve, J., **Jutila, A.**, Krampe, D., Shimanchuk, E., Raphael, I., Rabe, B., Kuznetsov, I., Mallet, M., Liu, H., Hoppmann, M., Fang, Y., Dumitrascu, A., Arndt, S., Anhaus, P., Nicolaus, M., Matero, I., Oggier, M., Eicken, H. and Haas, C.: **Platelet Ice Under Arctic Pack Ice in Winter**, *Geophysical Research Letters*, 47 (16), https://doi.org/10.1029/2020GL088898, 2020.

This study presents the first comprehensive, long-term in situ observations of a subice platelet layer under free-drifting pack ice of the Central Arctic observed during the ROV surveys of the MOSAiC drift expedition. I participated in the midwinter leg of MOSAiC, when the observations were done, assisted in the ROV surveys, and contributed to the writing and editing of the manuscript.

- Thielke, L., Huntemann, M., Hendricks, S., **Jutila, A.**, Ricker, R., and Spreen, G.: **Sea ice surface temperatures from helicopter-borne thermal infrared imaging during the MOSAiC expedition**, *under review at Scientific Data (Nature), MOSAiC Special Issue*, 2021.

This manuscript describes the sea-ice surface temperature data set derived from thermal infrared imagery captured during airborne surveys. I participated in the midwinter leg of MOSAiC, during which I was the principal investigator of helicopterborne measurements and collected the data, and contributed to the writing and editing of the manuscript.

- Nicolaus, M., Perovich, D. K., Spreen, G., Granskog, M. A., **the MOSAiC ICE team**[1] et al., **Overview of the MOSAiC expedition — Snow and Sea Ice**, *under review at Elementa, MOSAiC Special Feature*, 2021.

This manuscript summarises the year-round observations of the physical snow and sea-ice properties and processes conducted during the MOSAiC expedition. I participated in the midwinter leg of MOSAiC, during which I was the principal investigator of helicopterborne measurements, processed the ALS data onboard Polarstern for quicklook products, and assisted in several on-ice snow and sea-ice measurements. I contributed to the acquisition, analysis, and interpretation of data as well as drafting and revising the manuscript.

[1] The full author list includes over 100 names including the MOSAiC ICE team of which I was a member

Acknowledgements

I want to thank Prof. Dr. Christian Haas for taking me as his doctoral student and for the opportunity to carry out this dissertation by delving into microwave radar remote sensing of snow and into sea ice in general at the Sea Ice Physics section of the Alfred Wegener Institute. Along with him, I thank Stefan Hendricks and Robert Ricker for the supervision and all the invaluable support during the past years. Thank you for introducing me to the fascinating and wonderfully challenging world of airborne observations and particularly microwave radar measurements. I have learnt a lot.

Thanks to Stefanie Arndt for joining my thesis advisory committee. In addition, I am thankful for Prof. Dr. Olaf Eisen for agreeing to act as the second reviewer of this dissertation.

I want to acknowledge two persons in particular for considerable support during this work. First, John Paden from the Center for Remote Sensing of Ice Sheets (CReSIS) at the University of Kansas for patiently and repeatedly explaining the radar data processing for someone who is an absolute beginner with radars and engineering. Second, Josh King from the Environment and Climate Change Canada, many thanks for hosting me for the two-month visit in Toronto (go Raptors, We The North!) and for introducing me to Python and the ways to get meaningful snow depth out of the radar data. Thanks to you, now I know better: Python $\gg$ MATLAB.

I thank the graduate school POLMAR for funding the short-term research visit and offering so many useful courses. Particularly, I want to thank the POLMAR Claudias Hanfland and Sprengel and also Andrea Bleyer of the AWI International Office for answering all the questions a foreign doctoral student in a German research institute might have had.

During this doctoral degree, I have been extremely lucky to have had the opportunity of taking part in a total of three field expeditions on land, in the air, and at sea across the Arctic. Majority of the data presented in this dissertation was collected during those campaigns. I am thankful for all the support, planning, and logistics work that has enabled the realisation of the expeditions. I want to thank Philipp Anhaus, Christian Katlein, Christian Haas, Stefan Hendricks, Robert Ricker, Daniela Krampe, and Marcus Huntemann in particular for sharing the memorable times in the field. I am also grateful to have met so many new friends and colleagues around the world during these trips.

Thank you to all the former and current colleagues at the Sea Ice Physics section, especially my officemates Louisa von Hülsen, Philipp Anhaus, and Daniela Krampe, for the great working environment and the countless number of coffee breaks. Ilkka Matero, thanks for being an integral part of the biggest national minority of the Sea Ice Physics section: chatting

in Finnish was a valuable lifeline for me and I thoroughly enjoyed the numerous board game evenings. Last but by all means and in every imaginable and measurable way not least, Jakob Belter, thanks for being a great colleague at work and an awesome, trustworthy friend outside of it! The list of things I want to thank you for is so long that it would probably require an additional appendix to this thesis.

Part of my enthusiasm for the topic of this dissertation and for geophysics in general comes from the joyous years at my *alma mater*, the University of Helsinki. Thanks to my classmates and dear friends Katriina Juva and Elisa Lindgren, that excitement still carries on. Katriina, thank you for setting me the example and giving me the idea that one can successfully pursue a doctoral degree in Germany. Elisa, thanks for keeping my feet on the ground: you are the one of us with a permanent position. Thank you both for paying a visit to Bremerhaven.

I believe the remaining enthusiasm for snow originates from northern Lapland in Finland. Besides the years I grew up there, from there stems also the endless support and encouragement from my parents echoed by my brother and other relatives. Above all I thank my mum and dad for choosing snow-rich Inari as their place of residence to raise a family. To this day, I call that place home.

Aikanaan graduuni kirjoitin kiitokset jostain kumman syystä vain englanniksi. Nyt ymmärrän, että tämä on piru vie minun kirjani ja minähän kirjoitan siihen aivan mitä lystään! Tärkein viesti siis tässä vielä suomeksi: kiitokset ehtymättömästä tuesta koto-Suomeen, niin sukulaisille kuin ystäville, mutta ennen kaikkea vanhemmille Inariin. Se on paikka, jota edelleen kutsun kodiksi.

Completing a dissertation and a doctoral degree in a foreign country amidst a global pandemic has been a huge, exhausting, and at times overpowering challenge. But I think I survived. And I have all of you to thank for it.

Nomenclature

Acronyms

Acronym	Description
2-D	Two-dimensional
A10	Sea-ice density values in Alexandrov et al. (2010)
ADC	Analog-to-digital converter
AMAP	Arctic Monitoring and Assessment Program
AWI	Alfred Wegener Institute, Helmholtz Centre for Polar and Marine Research
ALS	Airborne laser scanner
AltiKa	Nadir altimeter in Ka band
ATLAS	Advanced Topographic Laser Altimeter System
BMBF	Bundesministerium für Bildung und Forschung
CERSAT	Center for Satellite Exploitation and Research
CIS	Canadian Ice Service
CLS	Collecte Localisation Satellites
CFS	Canadian Forces Station
CReSIS	Center for Remote Sensing of Ice Sheets
CRISTAL	Copernicus Polar Ice and Snow Topography Altimeter
CRYO2ICE	Resonance of the CryoSat-2 and ICESat-2 satellite orbits
CS2	CryoSat-2
CW	Continuous wave
DDS	Direct digital synthesizer
DFT	Discrete Fourier transform
DMS	Digital Mapping System
EASE	Equal Area Scalable Earth
ECCC	Environment and Climate Change Canada
EM	Electromagnetic
ERS	European Remote Sensing satellite

Acronym	Description
ESA	European Space Agency
EW	Extra-wide swath
FFSAR	Fully-focused synthetic aperture radar
FM	Frequency modulated
FMCW	Frequency-modulated continuous-wave
FYI	First-year ice
GPR	Ground-penetrating radar
GPS	Global Positioning System
GRD	Ground range detected
HF	High frequency
ICESat-2	Ice, Cloud, and land Elevation Satellite 2
ID	Identification
IW	Interferometric wide swath
IEEE	Institute of Electrical and Electronics Engineers
IFREMER	Institut français de recherche pour l'exploitation de la mer
IMB	Ice mass-balance buoy
INS	Inertial navigation system
IPCC	Intergovernmental Panel for Climate Change
IQR	Interquartile range
J21	Density parametrisation in Jutila et al. (2021a)
LWC	Liquid water content
MATLAB	Matrix laboratory
MOSAiC	Multidisciplinary drifting Observatory for the Study of Arctic Climate
MP	Magnaprobe
MSS	Mean sea-surface height
MYI	Multi-year ice
MYIf	Multi-year ice fraction
NASA	National Aeronautics and Space Administration
NOAA	National Oceanic and Atmospheric Administration
NSF	National Science Foundation
NSIDC	National Snow and Ice Data Center
OIB	Operation IceBridge
OSISAF	Ocean and Sea Ice Satellite Application Facility
PAMARCMiP	Polar Airborne Measurements and Arctic Regional Climate Model Simulation Project

Acronym	Description
PAR	photosynthetically active radiation
POLMAR	Helmholtz Graduate School for Polar and Marine Research
Pdf	Probability density function
Radar	Radio detection and ranging
RESURV79	Resurvey of the Nioghalvfjerdsbrae (79 N) Glacier
ROV	Remotely operated underwater vehicle
RMSE	Root-mean-square error
SAR	Synthetic-aperture radar
SARAL	Satellite for ARgos and ALtiKa
SIGRID-3	Sea Ice Grid format
SIMIP	Sea-Ice Model Intercomparison Project
SIRAL	SAR Interferometric Radar Altimeter
SMP	SnowMicroPen
SNR	Signal-to-noise ratio
SR	Snow Radar
SSH	Sea-surface height
SWE	Snow water equivalent
SYI	Second-year ice
TFMRA	Threshold first-maximum retracker algorithm
TLS	Terrestrial laser scanner
TWTT	Two-way travel time
UHF	Ultra high frequency
ULS	Upward-looking sonar
UTM	Universal Transverse Mercator
UV	Ultraviolet
VHF	Very high frequency
W99	Snow climatology in Warren et al. (1999)
WGS84	World Geodetic System standard 1984

Symbols

Symbol	Unit	Description
β	°	Half-power beamwidth for the synthetic aperture
δ_p	m	Penetration depth
$\delta_{\mathrm{SR-TLS}}$	m	Mean bias between the Snow Radar and terrestrial laser scanner derived snow depths
ΔR	m	Range resolution
$\varepsilon_{\mathrm{SR}}$	m	Precision of the Snow Radar
$\varepsilon_{\mathrm{TLS}}$	m	Precision of the terrestrial laser scanner
ε^*	F m^{-1}	Complex dielectric constant
ε_0	F m^{-1}	Free-space dielectric constant
ε'		Relative dielectric constant or relative permittivity
$\varepsilon'_{\mathrm{air}}$		Relative permittivity of air
$\varepsilon'_{\mathrm{ds}}$		Relative permittivity of dry snow
$\varepsilon'_{\mathrm{ice}}$		Relative permittivity of ice
ε''		Relative dielectric loss factor
$\varepsilon''_{\mathrm{air}}$		Relative dielectric loss factor of air
$\varepsilon''_{\mathrm{ds}}$		Relative dielectric loss factor of dry snow
$\varepsilon''_{\mathrm{ice}}$		Relative dielectric loss factor of ice
λ	m	Wavelength (at the center frequency)
ρ_{ds}	g cm^{-3}	Dry snow density
ρ_i	kg m^{-3}	Sea-ice density
ρ_s	kg m^{-3}	Snow density
ρ_w	kg m^{-3}	Sea-water density
$\bar{\rho}_i$	kg m^{-3}	Along-track averaged sea-ice density
σ		Radar cross section of the target
σ^0		Backscatter coefficient
σ_{ρ_i}	kg m^{-3}	Uncertainty of sea-ice density
σ_{ρ_s}	kg m^{-3}	Uncertainty of snow density
σ_{ρ_w}	kg m^{-3}	Uncertainty of sea-water density
$\sigma_{\bar{\rho}_i}$	kg m^{-3}	Uncertainty of along-track averaged sea-ice density
$\sigma_{h_{fs}}$	m	Uncertainty of snow freeboard
σ_{h_s}	m	Uncertainty of snow depth
σ_{SR}	m	Uncertainty of the Snow Radar derived snow depth
$\sigma_{h_{tot}}$	m	Uncertainty of total thickness
τ	s	Pulse length

Symbol	Unit	Description
τ_d	s	Time delay
θ_i	°	Angle of incidence
θ_r	°	Angle of refraction
θ_s	°	Angle of specular reflection
A	m^2	Area
B	Hz	Bandwidth
c	$m\ s^{-1}$	Speed of light in vacuum
c_s	$m\ s^{-1}$	Speed of light in snow
E	mm	Snow grain size
f	Hz	Frequency
f_b	Hz	Beat frequency
F		Snow grain shape/form
G	dBi	Antenna gain
h	m	Altitude above ground level
h_{fi}	m	Sea-ice freeboard
h_{fs}	m	Snow freeboard
h_i	m	Sea-ice thickness
h_{rms}	m	Root-mean-square height or the standard deviation of the surface height variance
h_s	m	Snow depth
h_{topo}	m	Nonparametric surface topography estimate
h_{tot}	m	Total (i.e., ice+snow) thickness
h_{05}	m	5th percentile of the surface elevation
h_{95}	m	95th percentile of the surface elevation
h'_f	m	Effective freeboard
i		Imaginary unit, $\sqrt{-1}$
k		Windowing factor
L	m	Unfocused synthetic aperture length
n		Product of presums, number of values
n_s		Refractive index of snow
$\tilde{n}$	dB	Noise
N		Number of range bins, number of values
p		p-value, probability
P^r	W	Received power
P^t	W	Transmitted power
PP_l		Left-hand peakiness

Symbol	Unit	Description
PP_r		Right-hand peakiness
PRF	Hz	Pulse repetition frequency
PSNR	dB	Peak signal-to-noise ratio
r		Pearson correlation coefficient
R	m	Range
R		Snow hardness
R^2		Coefficient of determination
r_{pl}	m	Cross-track resolution, diameter of pulse limited nadir-looking footprint
r_{at}	m	Along-track resolution
s		Waveform
$\tilde{s}$		Normalised waveform
S	ppt	Snow salinity
SSA	$m^2\ kg^{-1}$	Specific surface area
T_{pd}	s	Modulation period
T_s	°C	Snow temperature
TH_{lin}		Power threshold in the linear scale
TH_{log}		Power threshold in the logarithmic scale
v	$m\ s^{-1}$	Velocity of the platform

List of Figures

List of Tables

Bibliography

Ackley, S. F., Hibler, W. D., Kugzruk, F. K., Kovacs, A., and Weeks, W. F.: Thickness and roughness variations of Arctic multiyear sea ice, Tech. rep., Cold Regions Research and Engineering Laboratory, 1976.

Alexandrov, V., Sandven, S., Wahlin, J., and Johannessen, O. M.: The relation between sea ice thickness and freeboard in the Arctic, The Cryosphere, 4, 373–380, https://doi.org/10.5194/tc-4-373-2010, 2010.

Alfred-Wegener-Institut Helmholtz-Zentrum für Polar- und Meeresforschung: Polar aircraft Polar5 and Polar6 operated by the Alfred Wegener Institute, Journal of large-scale research facilities JLSRF, 2, A87, https://doi.org/10.17815/jlsrf-2-153, 2016.

AMAP: Arctic Climate Change Update 2021: Key Trends and Impacts. Summary for Policy-makers., last access: 12 June 2021, URL https://www.amap.no/documents/download/6759/inline, 2021.

Andersen, O. B., Piccioni, G., Stenseng, L., and Knudsen, P.: The DTU15 MSS (Mean Sea Surface) and DTU15LAT (Lowest Astronomical Tide) reference surface, URL https://ftp.space.dtu.dk/pub/DTU15/DOCUMENTS/MSS/DTU15MSS+LAT.pdf, 2016.

Armitage, T. W. K. and Ridout, A. L.: Arctic sea ice freeboard from AltiKa and comparison with CryoSat-2 and Operation IceBridge, Geophysical Research Letters, 42, 6724–6731, https://doi.org/10.1002/2015GL064823, 2015.

Arnold, E., Ewing, M., Hale, R., Keshmiri, S., Leuschen, C., Li, J., Paden, J., Rodriguez-Morales, F., and Berger, V.: RADAR SOUNDER PLATFORMS AND SENSORS AT CRESIS, in: IGARSS 2018 - 2018 IEEE International Geoscience and Remote Sensing Symposium, vol. 2018-July, pp. 7902–7905, IEEE, https://doi.org/10.1109/IGARSS.2018.8519009, 2018.

AWI IceBird program: URL https://www.awi.de/en/science/climate-sciences/sea-ice-physics/projects/ice-bird.html, last access: 10 May 2021, 2020.

Babb, D. G., Landy, J. C., Lukovich, J. V., Haas, C., Hendricks, S., Barber, D. G., and Galley, R. J.: The 2017 Reversal of the Beaufort Gyre: Can Dynamic Thickening of a Seasonal Ice Cover During a Reversal Limit Summer Ice Melt in the Beaufort Sea?, Journal of Geophysical Research: Oceans, 125, e2020JC016 796, https://doi.org/10.1029/2020JC016796, 2020.

Barber, D. G., Reddan, S. P., and LeDrew, E. F.: Statistical characterization of the geophysical and electrical properties of snow on landfast first-year sea ice, Journal of Geophysical Research, 100, 2673–2686, https://doi.org/10.1029/94JC02200, 1995.

Barber, D. G., Meier, W. N., Gerland, S., Mundy, C., Holland, M., Kern, S., Li, Z., Michel, C., Perovich, D. K., and Tamura, T.: Arctic sea ice, in: Snow, Water, Ice and Permafrost in the Arctic (SWIPA) 2017, chap. 5, pp. 103–136, Arctic Monitoring and Assessment Programme (AMAP), Oslo, Norway, URL https://www.amap.no/documents/doc/snow-water-ice-and-permafrost-in-the-arctic-swipa-2017/1610, 2017.

Barrett, A. P., Stroeve, J. C., and Serreze, M. C.: Arctic Ocean Precipitation From Atmospheric Reanalyses and Comparisons With North Pole Drifting Station Records, Journal of Geophysical Research: Oceans, 125, e2019JC015 415, https://doi.org/10.1029/2019JC015415, 2020.

Beaven, S. G., Lockhart, G. L., Gogineni, S. P., Hossetnmostafs, A. R., Jezek, K., Gow, A. J., Perovich, D. K., Fung, A. K., and Tjuatja, S.: Laboratory measurements of radar backscatter from bare and snow-covered saline ice sheets, International Journal of Remote Sensing, 16, 851–876, https://doi.org/10.1080/01431169508954448, 1995.

Belter, H. J., Krumpen, T., Hendricks, S., Hoelemann, J., Janout, M. A., Ricker, R., and Haas, C.: Satellite-based sea ice thickness changes in the Laptev Sea from 2002 to 2017: comparison to mooring observations, The Cryosphere, 14, 2189–2203, https://doi.org/10.5194/tc-14-2189-2020, 2020.

Belter, H. J., Krumpen, T., von Albedyll, L., Alekseeva, T. A., Birnbaum, G., Frolov, S. V., Hendricks, S., Herber, A., Polyakov, I., Raphael, I., Ricker, R., Serovetnikov, S. S., Webster, M., and Haas, C.: Interannual variability in Transpolar Drift summer sea ice thickness and potential impact of Atlantification, The Cryosphere, 15, 2575–2591, https://doi.org/10.5194/tc-15-2575-2021, 2021.

Blanchard-Wrigglesworth, E., Webster, M. A., Farrell, S. L., and Bitz, C. M.: Reconstruction of Snow on Arctic Sea Ice, Journal of Geophysical Research: Oceans, 123, 3588–3602, https://doi.org/10.1002/2017JC013364, 2018.

Braakmann-Folgmann, A. and Donlon, C.: Estimating snow depth on Arctic sea ice using satellite microwave radiometry and a neural network, The Cryosphere, 13, 2421–2438, https://doi.org/10.5194/tc-13-2421-2019, 2019.

Canadian Coast Guard: Navigation in Ice Covered Waters, in: Ice Navigation in Canadian Waters, chap. 4, pp. 81–131, Icebreaking Program, Maritime Services Canadian Coast Guard Fisheries and Oceans Canada, Ottawa, Ontario, URL https://www.ccg-gcc.gc.ca/publications/icebreaking-deglacage/ice-navigation-glaces/page05-eng.html, 2012.

Canadian Ice Service: Canadian Ice Service Arctic Regional Sea Ice Charts in SIGRID-3 Format, [2–8 April 2017 and 2–10 April 2019], Boulder, Colorado USA, NSIDC: National Snow and Ice Data Center [data set], https://doi.org/10.7265/N51V5BW9, 2009.

Comiso, J., Cavalieri, D., and Markus, T.: Sea ice concentration, ice temperature, and snow depth using AMSR-E data, IEEE Transactions on Geoscience and Remote Sensing, 41, 243–252, https://doi.org/10.1109/TGRS.2002.808317, 2003.

Comiso, J. C.: Large Decadal Decline of the Arctic Multiyear Ice Cover, Journal of Climate, 25, 1176–1193, https://doi.org/10.1175/JCLI-D-11-00113.1, 2012.

CReSIS: CReSIS toolbox: Polar radar software toolbox, source code, [code], last access: 3 July 2020, URL https://github.com/CReSIS/cresis-toolbox, 2020a.

CReSIS: CReSIS toolbox: Polar radar software toolbox, documentation, last access: 3 July 2020, URL https://ops.cresis.ku.edu/wiki/index.php/Main{_}Page, 2020b.

Dominguez, R.: IceBridge DMS L1B Geolocated and Orthorectified Images, Version 1, [4 and 16 April 2018], Boulder, Colorado USA. NASA National Snow and Ice Data Center Distributed Active Archive Center [data set], https://doi.org/10.5067/OZ6VNOPMPRJ0, last access: 11 Aug 2021, 2010, updated 2018.

Donlon, C., Berruti, B., Buongiorno, A., Ferreira, M.-H., Féménias, P., Frerick, J., Goryl, P., Klein, U., Laur, H., Mavrocordatos, C., Nieke, J., Rebhan, H., Seitz, B., Stroede, J., and Sciarra, R.: The Global Monitoring for Environment and Security (GMES) Sentinel-3 mission, Remote Sensing of Environment, 120, 37–57, https://doi.org/10.1016/j.rse.2011.07.024, 2012.

Donlon, C. J., Cullen, R., Giulicchi, L., Vuilleumier, P., Francis, C. R., Kuschnerus, M., Simpson, W., Bouridah, A., Caleno, M., Bertoni, R., Rancaño, J., Pourier, E., Hyslop, A., Mulcahy, J., Knockaert, R., Hunter, C., Webb, A., Fornari, M., Vaze, P., Brown, S., Willis, J., Desai, S., Desjonqueres, J.-D., Scharroo, R., Martin-Puig, C., Leuliette, E., Egido, A., Smith, W. H., Bonnefond, P., Le Gac, S., Picot, N., and Tavernier, G.: The Copernicus Sentinel-6 mission: Enhanced continuity of satellite sea level measurements from space, Remote Sensing of Environment, 258, 112 395, https://doi.org/10.1016/j.rse.2021.112395, 2021.

Druckenmiller, M. L., Moon, T. A., and Thoman, R. L.: The Arctic, in: State of the Climate 2020, Bulletin of the American Meteorological Society, 102, S263–S316, https://doi.org/10.1175/BAMS-D-21-0086.1, 2021.

Duchossois, G., Strobl, P., Toumazou, V., Antunes, S., Bartsch, A., Diehl, T., Dinessen, F., Eriksson, P., Garric, G., Houssais, M.-N., Jindrova, M., Muñoz-Sabater, J., Nagler, T., and Nordbeck, O.: User Requirements for a Copernicus Polar Mission - Phase 1 Report, Tech. rep., Publications Office of the European Union, Luxembourg, https://doi.org/10.2760/22832, 2018.

Egido, A. and Smith, W. H. F.: Fully Focused SAR Altimetry: Theory and Applications, IEEE Transactions on Geoscience and Remote Sensing, 55, 392–406, https://doi.org/10.1109/TGRS.2016.2607122, 2017.

Ezraty, R., Girard-Ardhuin, F., Piollé, J.-F., Kaleschke, L., and Heygster, G.: ARCTIC & ANTARCTIC SEA ICE CONCENTRATION AND ARCTIC SEA ICE DRIFT ESTIMATED FROM SPECIAL SENSOR MICROWAVE DATA, Tech. rep., Laboratoire d'Océanographie Spatiale Département d'Océanographie Physique et Spatiale IFREMER, Brest, France and Institute of Environmental Physics University of Bremen, Germany, URL ftp://ftp.ifremer.fr/ifremer/cersat/products/gridded/psi-drift/documentation/ssmi.pdf, 2007.

Farrell, S. L., Kurtz, N., Connor, L. N., Elder, B. C., Leuschen, C., Markus, T., McAdoo, D. C., Panzer, B., Richter-Menge, J., and Sonntag, J. G.: A First Assessment of IceBridge Snow and Ice Thickness Data Over Arctic Sea Ice, IEEE Transactions on Geoscience and Remote Sensing, 50, 2098–2111, https://doi.org/10.1109/TGRS.2011.2170843, 2012.

Fierz, C., Armstrong, R., Durand, Y., Etchevers, P., Greene, E., McClung, D. M., Nishimura, K., Satyawali, P. K., and Sokratov, S. A.: The International Classification for Seasonal Snow on the Ground, Tech. rep., UNESCO-IHP, Paris, IHP-VII Technical Documents in Hydrology N°83, IACS Contribution N°1, 2009.

Gallet, J.-C., Domine, F., Zender, C. S., and Picard, G.: Measurement of the specific surface area of snow using infrared reflectance in an integrating sphere at 1310 and 1550 nm, The Cryosphere, 3, 167–182, URL www.the-cryosphere.net/3/167/2009/, 2009.

Giles, K., Laxon, S., Wingham, D., Wallis, D., Krabill, W., Leuschen, C., McAdoo, D., Manizade, S., and Raney, R.: Combined airborne laser and radar altimeter measurements over the Fram Strait in May 2002, Remote Sensing of Environment, 111, 182–194, https://doi.org/10.1016/j.rse.2007.02.037, 2007.

GISTEMP Team: GISS Surface Temperature Analysis (GISTEMP), version 4, NASA Goddard Institute for Space Studies, last access: 13 May 2021, [data set], URL https://data.giss.nasa.gov/gistemp/, 2021.

Granskog, M. A., Rösel, A., Dodd, P. A., Divine, D., Gerland, S., Martma, T., and Leng, M. J.: Snow contribution to first-year and second-year Arctic sea ice mass balance north of Svalbard, Journal of Geophysical Research: Oceans, 122, 2539–2549, https://doi.org/10.1002/2016JC012398, 2017.

Grosfeld, K., Treffeisen, R., Asseng, J., Bartsch, A., Bräuer, B., Fritzsch, B., Gerdes, R., Hendricks, S., Hiller, W., Heygster, G., Krumpen, T., Lemke, P., Melsheimer, C., Nicolaus, M., Ricker, R., and Weigelt, M.: Online Sea-Ice Knowledge and Data Platform <www.meereisportal.de>, Polarforschung, 85, 143–155, https://doi.org/10.2312/polfor.2016.011, 2015.

Guerreiro, K., Fleury, S., Zakharova, E., Rémy, F., and Kouraev, A.: Potential for estimation of snow depth on Arctic sea ice from CryoSat-2 and SARAL/AltiKa missions, Remote Sensing of Environment, 186, 339–349, https://doi.org/10.1016/j.rse.2016.07.013, 2016.

Haas, C., Gerland, S., Eicken, H., and Miller, H.: Comparison of sea-ice thickness measurements under summer and winter conditions in the Arctic using a small electromagnetic induction device, GEOPHYSICS, 62, 749–757, https://doi.org/10.1190/1.1444184, 1997.

Haas, C., Lobach, J., Hendricks, S., Rabenstein, L., and Pfaffling, A.: Helicopter-borne measurements of sea ice thickness, using a small and lightweight, digital EM system, Journal of Applied Geophysics, 67, 234–241, https://doi.org/10.1016/j.jappgeo.2008.05.005, 2009.

Haas, C., Hendricks, S., Eicken, H., and Herber, A.: Synoptic airborne thickness surveys reveal state of Arctic sea ice cover, Geophysical Research Letters, 37, L09 501, https://doi.org/10.1029/2010GL042652, 2010.

Haas, C., Beckers, J., King, J., Silis, A., Stroeve, J., Wilkinson, J., Notenboom, B., Schweiger, A., and Hendricks, S.: Ice and Snow Thickness Variability and Change in the High Arctic Ocean Observed by In Situ Measurements, Geophysical Research Letters, 44, 10 462–10 469, https://doi.org/10.1002/2017GL075434, 2017.

Haas, C., Langhorne, P. J., Rack, W., Leonard, G. H., Brett, G. M., Price, D., Beckers, J. F., and Gough, A. J.: Airborne mapping of the sub-ice platelet layer under fast ice in McMurdo Sound, Antarctica, The Cryosphere, 15, 247–264, https://doi.org/10.5194/tc-15-247-2021, 2021.

Helm, V.: Airborne SAR/Interferometric Radar Altimeter System (ASIRAS) - Kalibrierung, Validierung und Interpretation der Messergebnisse, Ph.D. thesis, Universität Bremen, URL http://nbn-resolving.de/urn:nbn:de:gbv:46-diss000111668, 2008.

Hendricks, S. and Ricker, R.: Product User Guide & Algorithm Specification AWI CryoSat-2 Sea Ice Thickness (version 2.3), Tech. rep., Alfred Wegener Institute Helmholtz Centre for Polar and Marine Research, URL https://hdl.handle.net/10013/epic.ecd56b5d-3e7d-4a65-9019-588b1c3b0d26, 2020.

Hendricks, S., Ricker, R., and Jutila, A.: IceBird 2019 Winter: ICESat-2 Validation Data Acquisition Report, Tech. rep., Alfred Wegener Institute, URL https://hdl.handle.net/10013/epic.c5dfe9f3-a928-4706-addc-b5b8f3af723a, 2019.

Herber, A. B., Haas, C., Stone, R. S., Bottenheim, J. W., Liu, P., Li, S.-M., Staebler, R. M., Strapp, J. W., and Dethloff, K.: Regular airborne surveys of Arctic sea ice and atmosphere, Eos, Transactions American Geophysical Union, 93, 41–42, https://doi.org/10.1029/2012EO040001, 2012.

Hoppmann, M., Richter, M. E., Smith, I. J., Jendersie, S., Langhorne, P. J., Thomas, D. N., and Dieckmann, G. S.: Platelet ice, the Southern Ocean's hidden ice: a review, Annals of Glaciology, 61, 341–368, https://doi.org/10.1017/aog.2020.54, 2020.

Hunke, E. C., Notz, D., Turner, A. K., and Vancoppenolle, M.: The multiphase physics of sea ice: a review for model developers, The Cryosphere, 5, 989–1009, https://doi.org/10.5194/tc-5-989-2011, 2011.

Hutchings, J. K.: Shipborne visual observations of Arctic sea ice, [data set], https://doi.org/10.1594/PANGAEA.889209, 2018.

IEEE: IEEE Standard for Ultrawideband Radar Definitions, https://doi.org/10.1109/IEEESTD.2007.359972, 2007.

IEEE: IEEE Standard Letter Designations for Radar-Frequency Bands, https://doi.org/10.1109/IEEESTD.2020.8999849, 2020.

Jackson, K., Wilkinson, J., Maksym, T., Meldrum, D., Beckers, J., Haas, C., and Mackenzie, D.: A novel and low-cost sea ice mass balance buoy, Journal of Atmospheric and Oceanic Technology, 30, 2676–2688, https://doi.org/10.1175/JTECH-D-13-00058.1, 2013.

Jutila, A., Hendricks, S., Ricker, R., von Albedyll, L., Krumpen, T., and Haas, C.: Retrieval and parametrisation of sea-ice bulk density from airborne multi-sensor measurements, The Cryosphere Discuss., pp. 1–25, https://doi.org/10.5194/tc-2021-149, 2021a.

Jutila, A., King, J., Paden, J., Ricker, R., Hendricks, S., Polashenski, C., Helm, V., Binder, T., and Haas, C.: High-Resolution Snow Depth on Arctic Sea Ice From Low-Altitude Airborne Microwave Radar Data, IEEE Transactions on Geoscience and Remote Sensing, pp. 1–16, https://doi.org/10.1109/TGRS.2021.3063756, 2021b.

Kanagaratnam, P., Markus, T., Lytle, V., Heavey, B., Jansen, P., Prescott, G., and Gogineni, S.: Ultrawideband Radar Measurements of Thickness of Snow Over Sea Ice, IEEE Transactions on Geoscience and Remote Sensing, 45, 2715–2724, https://doi.org/10.1109/TGRS.2007.900673, 2007.

Katlein, C. and Nicolaus, M.: Snow height on sea ice and sea ice drift from autonomous measurements from buoy 2018S65, deployed during LIA 2018, PANGAEA, https://doi.org/10.1594/PANGAEA.905719, in: Nicolaus, Marcel; Hoppmann, Mario; Arndt, Stefanie; Hendricks, Stefan; Katlein, Christian; König-Langlo, Gert; Nicolaus, Anja; Rossmann, Leonard; Schiller, Martin; Schwegmann, Sandra; Langevin, Danielle; Bartsch, Annekathrin (2017): Snow height and air temperature on sea ice from Snow Buoy measurements. Alfred Wegener Institute, Helmholtz Centre for Polar and Marine Research, Bremerhaven, PANGAEA, https://doi.org/10.1594/PANGAEA.875638, 2019.

Kern, M., Cullen, R., Berruti, B., Bouffard, J., Casal, T., Drinkwater, M. R., Gabriele, A., Lecuyot, A., Ludwig, M., Midthassel, R., Navas Traver, I., Parrinello, T., Ressler, G., Andersson, E., Martin-Puig, C., Andersen, O., Bartsch, A., Farrell, S., Fleury, S., Gascoin, S., Guillot, A., Humbert, A., Rinne, E., Shepherd, A., van den Broeke, M. R., and Yackel, J.: The Copernicus Polar Ice and Snow Topography Altimeter (CRISTAL) high-priority candidate mission, The Cryosphere, 14, 2235–2251, https://doi.org/10.5194/tc-14-2235-2020, 2020.

Khvorostovsky, K., Hendricks, S., and Rinne, E.: Surface Properties Linked to Retrieval Uncertainty of Satellite Sea-Ice Thickness with Upward-Looking Sonar Measurements, Remote Sensing, 12, 3094, https://doi.org/10.3390/rs12183094, 2020.

Kilic, L., Tonboe, R. T., Prigent, C., and Heygster, G.: Estimating the snow depth, the snow–ice interface temperature, and the effective temperature of Arctic sea ice using Advanced Microwave Scanning Radiometer 2 and ice mass balance buoy data, The Cryosphere, 13, 1283–1296, https://doi.org/10.5194/tc-13-1283-2019, 2019.

King, J., Howell, S., Derksen, C., Rutter, N., Toose, P., Beckers, J. F., Haas, C., Kurtz, N., and Richter-Menge, J.: Evaluation of Operation IceBridge quick-look snow depth estimates on sea ice, Geophysical Research Letters, 42, 9302–9310, https://doi.org/10.1002/2015GL066389, 2015.

King, J., Brady, M., and Newman, T.: kingjml/pySnowRadar: IEEE TGRS Submission, Zenodo [code], https://doi.org/10.5281/ZENODO.4071801, 2020a.

King, J., Howell, S., Brady, M., Toose, P., Derksen, C., Haas, C., and Beckers, J.: Local-scale variability of snow density on Arctic sea ice, The Cryosphere, 14, 4323–4339, https://doi.org/10.5194/tc-14-4323-2020, 2020b.

Koenig, L., Martin, S., Studinger, M., and Sonntag, J.: Polar Airborne Observations Fill Gap in Satellite Data, Eos, Transactions American Geophysical Union, 91, 333–334, https://doi.org/10.1029/2010EO380002, 2010.

Koenig, L. S., Ivanoff, A., Alexander, P. M., Macgregor, J. A., Fettweis, X., Panzer, B., Paden, J. D., Forster, R. R., Das, I., Mcconnell, J. R., Tedesco, M., Leuschen, C., and Gogineni, P.: Annual Greenland accumulation rates (2009-2012) from airborne snow radar, The Cryosphere, 10, 1739–1752, https://doi.org/10.5194/tc-10-1739-2016, 2016.

Koh, G., Yankielun, N. E., and Baptista, A. I.: SNOW COVER CHARACTERIZATION USING MULTIBAND FMCW RADARS, HYDROLOGICAL PROCESSES, 10, 1609–1617, https://doi.org/10.1002/(SICI)1099-1085(199612)10:12, 1996.

Kovacs, A.: Estimating the full-scale flexural and compressive strength of first-year sea ice, Journal of Geophysical Research: Oceans, 102, 8681–8689, https://doi.org/10.1029/96JC02738, 1997.

Kovacs, A. and Morey, R. M.: Sounding sea ice thickness using a portable electromagnetic induction instrument, Geophysics, 56, 1992–1998, https://doi.org/10.1190/1.1443011, 1991.

Krumpen, T.: AWI ICETrack: Antarctic and Arctic Sea Ice Monitoring and Tracking Tool, Vers. 1.3, URL https://hdl.handle.net/10013/epic.9ee550b6-5966-4db6-a042-f4256810ec3f, 2018.

Krumpen, T., Belter, H. J., Boetius, A., Damm, E., Haas, C., Hendricks, S., Nicolaus, M., Nöthig, E. M., Paul, S., Peeken, I., Ricker, R., and Stein, R.: Arctic warming interrupts the Transpolar Drift and affects long-range transport of sea ice and ice-rafted matter, Scientific Reports, 9, 1–9, https://doi.org/10.1038/s41598-019-41456-y, 2019.

Krumpen, T., Birrien, F., Kauker, F., Rackow, T., von Albedyll, L., Angelopoulos, M., Belter, H. J., Bessonov, V., Damm, E., Dethloff, K., Haapala, J., Haas, C., Harris, C., Hendricks, S., Hoelemann, J., Hoppmann, M., Kaleschke, L., Karcher, M., Kolabutin, N., Lei, R., Lenz, J., Morgenstern, A., Nicolaus, M., Nixdorf, U., Petrovsky, T., Rabe, B., Rabenstein, L., Rex, M., Ricker, R., Rohde, J., Shimanchuk, E., Singha, S., Smolyanitsky, V., Sokolov, V., Stanton, T., Timofeeva, A., Tsamados, M., and Watkins, D.: The MOSAiC ice floe: sediment-laden survivor from the Siberian shelf, The Cryosphere, 14, 2173–2187, https://doi.org/10.5194/tc-14-2173-2020, 2020.

Kurtz, N., Studinger, M., Harbeck, J., Onana, V., and Yi, D.: IceBridge L4 Sea Ice Freeboard, Snow Depth, and Thickness, Version 1, Boulder, Colorado USA. NASA National Snow and Ice Data Center Distributed Active Archive Center [data set], https://doi.org/10.5067/G519SHCKWQV6, 2015.

Kurtz, N. T. and Farrell, S. L.: Large-scale surveys of snow depth on Arctic sea ice from Operation IceBridge, Geophysical Research Letters, 38, L20 505, https://doi.org/10.1029/2011GL049216, 2011.

Kurtz, N. T., Farrell, S. L., Studinger, M., Galin, N., Harbeck, J. P., Lindsay, R., Onana, V. D., Panzer, B., and Sonntag, J. G.: Sea ice thickness, freeboard, and snow depth products from Operation IceBridge airborne data, The Cryosphere, 7, 1035–1056, https://doi.org/10.5194/tc-7-1035-2013, 2013.

Kurtz, N. T., Galin, N., and Studinger, M.: An improved CryoSat-2 sea ice freeboard retrieval algorithm through the use of waveform fitting, The Cryosphere, 8, 1217–1237, https://doi.org/10.5194/tc-8-1217-2014, 2014.

Kwok, R.: Satellite remote sensing of sea-ice thickness and kinematics: a review, Journal of Glaciology, 56, 1129–1140, https://doi.org/10.3189/002214311796406167, 2010.

Kwok, R. and Cunningham, G. F.: Variability of Arctic sea ice thickness and volume from CryoSat-2, Philosophical Transactions of the Royal Society A: Mathematical, Physical and Engineering Sciences, 373, 20140 157, https://doi.org/10.1098/rsta.2014.0157, 2015.

Kwok, R. and Haas, C.: Effects of radar side-lobes on snow depth retrievals from Operation IceBridge, Journal of Glaciology, 61, 576–584, https://doi.org/10.3189/2015JoG14J229, 2015.

Kwok, R. and Kacimi, S.: Three years of sea ice freeboard, snow depth, and ice thickness of the Weddell Sea from Operation IceBridge and CryoSat-2, The Cryosphere, 12, 2789–2801, https://doi.org/10.5194/tc-12-2789-2018, 2018.

Kwok, R. and Maksym, T.: Snow depth of the Weddell and Bellingshausen sea ice covers from IceBridge surveys in 2010 and 2011: An examination, Journal of Geophysical Research: Oceans, 119, 4141–4167, https://doi.org/10.1002/2014JC009943, 2014.

Kwok, R. and Markus, T.: Potential basin-scale estimates of Arctic snow depth with sea ice freeboards from CryoSat-2 and ICESat-2: An exploratory analysis, Advances in Space Research, 62, 1243–1250, https://doi.org/10.1016/j.asr.2017.09.007, 2018.

Kwok, R., Panzer, B., Leuschen, C., Pang, S., Markus, T., Holt, B., and Gogineni, S.: Airborne surveys of snow depth over Arctic sea ice, Journal of Geophysical Research, 116, C11 018, https://doi.org/10.1029/2011JC007371, 2011.

Kwok, R., Kurtz, N. T., Brucker, L., Ivanoff, A., Newman, T., Farrell, S. L., King, J., Howell, S., Webster, M. A., Paden, J., Leuschen, C., MacGregor, J. A., Richter-Menge, J., Harbeck, J., and Tschudi, M.: Intercomparison of snow depth retrievals over Arctic sea ice from radar data acquired by Operation IceBridge, The Cryosphere, 11, 2571–2593, https://doi.org/10.5194/tc-11-2571-2017, 2017.

Kwok, R., Kacimi, S., Webster, M. A., Kurtz, N. T., and Petty, A. A.: Arctic Snow Depth and Sea Ice Thickness From ICESat-2 and CryoSat-2 Freeboards: A First Examination, Journal of Geophysical Research: Oceans, 125, e2019JC016 008, https://doi.org/10.1029/2019JC016008, 2020.

Laidre, K. L. and Regehr, E. V.: Arctic marine mammals and sea ice, in: Sea Ice, edited by Thomas, D. N., chap. 21, pp. 516–533, John Wiley & Sons, Ltd, Chichester, UK, third edn., https://doi.org/10.1002/9781118778371.ch21, 2017.

Landy, J. C., Tsamados, M., and Scharien, R. K.: A Facet-Based Numerical Model for Simulating SAR Altimeter Echoes From Heterogeneous Sea Ice Surfaces, IEEE Transactions on Geoscience and Remote Sensing, 57, 4164–4180, https://doi.org/10.1109/TGRS.2018.2889763, 2019.

Landy, J. C., Petty, A. A., Tsamados, M., and Stroeve, J. C.: Sea Ice Roughness Overlooked as a Key Source of Uncertainty in CryoSat-2 Ice Freeboard Retrievals, Journal of Geophysical Research: Oceans, 125, e2019JC015 820, https://doi.org/10.1029/2019JC015820, 2020.

Lange, B., Haas, C., Charette, J., Katlein, C., Campbell, K., Duerksen, S., Coupel, P., Anhaus, P., Jutila, A., Tremblay, P., Carlyle, C., and Michel, C.: Contrasting Ice Algae and Snow-Dependent Irradiance Relationships Between First-Year and Multiyear Sea Ice, Geophysical Research Letters, 46, 10 834–10 843, https://doi.org/10.1029/2019GL082873, 2019.

Lavergne, T., Eastwood, S., Teffah, Z., Schyberg, H., and Breivik, L.-A.: Sea ice motion from low-resolution satellite sensors: An alternative method and its validation in the Arctic, Journal of Geophysical Research, 115, C10 032, https://doi.org/10.1029/2009JC005958, 2010.

Lawrence, I. R., Tsamados, M. C., Stroeve, J. C., Armitage, T. W. K., and Ridout, A. L.: Estimating snow depth over Arctic sea ice from calibrated dual-frequency radar freeboards, The Cryosphere, 12, 3551–3564, https://doi.org/10.5194/tc-12-3551-2018, 2018.

Laxon, S., Peacock, N., and Smith, D.: High interannual variability of sea ice thickness in the Arctic region, Nature, 425, 947–950, https://doi.org/10.1038/nature02050, 2003.

Lenssen, N. J. L., Schmidt, G. A., Hansen, J. E., Menne, M. J., Persin, A., Ruedy, R., and Zyss, D.: Improvements in the GISTEMP Uncertainty Model, Journal of Geophysical Research: Atmospheres, 124, 6307–6326, https://doi.org/10.1029/2018JD029522, 2019.

Liston, G. E., Itkin, P., Stroeve, J., Tschudi, M., Stewart, J. S., Pedersen, S. H., Reinking, A. K., and Elder, K.: A Lagrangian Snow-Evolution System for Sea-Ice Applications (SnowModel-LG): Part I—Model Description, Journal of Geophysical Research: Oceans, 125, e2019JC015 913, https://doi.org/10.1029/2019JC015913, 2020.

Lubin, D. and Massom, R.: Sea ice, in: Polar Remote Sensing, Volume I: Atmosphere and Oceans, chap. 5, pp. 309–728, Springer Berlin Heidelberg, https://doi.org/10.1007/3-540-30785-0_5, 2006.

Lundberg, A., Granlund, N., and Gustafsson, D.: Towards automated 'ground truth' snow measurements — a review of operational and new measurement methods for Sweden, Norway, and Finland, Hydrological Processes, 24, 1955–1970, https://doi.org/10.1002/HYP.7658, 2010.

Maaß, N., Kaleschke, L., Tian-Kunze, X., and Drusch, M.: Snow thickness retrieval over thick Arctic sea ice using SMOS satellite data, The Cryosphere, 7, 1971–1989, https://doi.org/10.5194/tc-7-1971-2013, 2013.

MacGregor, J. A., Boisvert, L. N., Medley, B., Petty, A. A., Harbeck, J. P., Bell, R. E., Blair, J. B., Blanchard-Wrigglesworth, E., Buckley, E. M., Christoffersen, M. S., Cochran, J. R., Csathó, B. M., Marco, E. L., Dominguez, R. T., Fahnestock, M. A., Farrell, S. L., Gogineni, S. P., Greenbaum, J. S., Hansen, C. M., Hofton, M. A., Holt, J. W., Jezek, K. C., Koenig, L. S., Kurtz, N. T., Kwok, R., Larsen, C. F., Leuschen, C. J., Locke, C. D., Manizade, S. S., Martin, S.,

Neumann, T. A., Nowicki, S. M., Paden, J. D., Richter-Menge, J. A., Rignot, E. J., Rodríguez-Morales, F., Siegfried, M. R., Smith, B. E., Sonntag, J. G., Studinger, M., Tinto, K. J., Truffer, M., Wagner, T. P., Woods, J. E., Young, D. A., and Yungel, J. K.: The Scientific Legacy of NASA's Operation IceBridge, Reviews of Geophysics, 59, e2020RG000 712, https://doi.org/10.1029/2020RG000712, 2021.

Markus, T. and Cavalieri, D. J.: Snow Depth Distribution Over Sea Ice in the Southern Ocean from Satellite Passive Microwave Data, in: Antarctic Sea Ice: Physical Processes, Interactions and Variability, edited by Jeffries, M. O., pp. 19–39, American Geophysical Union (AGU), https://doi.org/10.1029/AR074p0019, 1998.

Markus, T., Neumann, T., Martino, A., Abdalati, W., Brunt, K., Csatho, B., Farrell, S., Fricker, H., Gardner, A., Harding, D., Jasinski, M., Kwok, R., Magruder, L., Lubin, D., Luthcke, S., Morison, J., Nelson, R., Neuenschwander, A., Palm, S., Popescu, S., Shum, C., Schutz, B. E., Smith, B., Yang, Y., and Zwally, J.: The Ice, Cloud, and land Elevation Satellite-2 (ICESat-2): Science requirements, concept, and implementation, Remote Sensing of Environment, 190, 260–273, https://doi.org/10.1016/j.rse.2016.12.029, 2017.

Marshall, H.-P. and Koh, G.: FMCW radars for snow research, Cold Regions Science and Technology, 52, 118–131, https://doi.org/10.1016/j.coldregions.2007.04.008, 2008.

Marshall, H.-P., Schneebeli, M., and Koh, G.: Snow stratigraphy measurements with high-frequency FMCW radar: Comparison with snow micro-penetrometer, Cold Regions Science and Technology, 47, 108–117, https://doi.org/10.1016/j.coldregions.2006.08.008, 2007.

Maslanik, J., Stroeve, J., Fowler, C., and Emery, W.: Distribution and trends in Arctic sea ice age through spring 2011, Geophysical Research Letters, 38, L13 502, https://doi.org/10.1029/2011GL047735, 2011.

Massom, R. A., Eicken, H., Haas, C., Jeffries, M. O., Drinkwater, M. R., Sturm, M., Worby, A. P., Wu, X., Lytle, V. I., Ushio, S., Morris, K., Reid, P. A., Warren, S. G., and Allison, I.: Snow on Antarctic sea ice, Reviews of Geophysics, 39, 413–445, https://doi.org/10.1029/2000RG000085, 2001.

Maykut, G. A. and Untersteiner, N.: Some results from a time-dependent thermodynamic model of sea ice, Journal of Geophysical Research, 76, 1550–1575, https://doi.org/10.1029/JC076i006p01550, 1971.

Meier, W. N., Hovelsrud, G. K., van Oort, B. E., Key, J. R., Kovacs, K. M., Michel, C., Haas, C., Granskog, M. A., Gerland, S., Perovich, D. K., Makshtas, A., and Reist, J. D.: Arctic sea ice in transformation: A review of recent observed changes and impacts on biology and human activity, Reviews of Geophysics, 52, 185–217, https://doi.org/10.1002/2013RG000431, 2014.

Meier, W. N., Fetterer, F., Windnagel, A. K., and Stewart, J. S.: NOAA/NSIDC Climate Data Record of Passive Microwave Sea Ice Concentration, Version 4, [May 2018], Boulder, Colorado USA. NSIDC: National Snow and Ice Data Center [data set], https://doi.org/10.7265/efmz-2t65, last access: 19 Aug 2021, 2021.

Meredith, M., Sommerkorn, M., Cassotta, S., Derksen, C., Ekaykin, A., Hollowed, A., Kofinas, G., Mackintosh, A., Melbourne-Thomas, J., Muelbert, M., Ottersen, G., Pritchard, H., and Schuur, E.: Polar Regions, in: IPCC Special Report on the Ocean and Cryosphere in a Changing Climate, edited by Pörtner, H.-O., Roberts, D., Masson-Delmotte, V., Zhai, P., Tignor, M., Poloczanska, E., Mintenbeck, K., Alegría, A., Nicolai, M., Okem, A., Petzold, J., Rama, B., and Weyer, N., Intergovernmental Panel on Climate Change, Geneva, Switzerland, URL https://www.ipcc.ch/srocc/chapter/chapter-3-2/, 2019.

Merkouriadi, I., Cheng, B., Graham, R. M., Rösel, A., and Granskog, M. A.: Critical Role of Snow on Sea Ice Growth in the Atlantic Sector of the Arctic Ocean, Geophysical Research Letters, 44, 10 479–10 485, https://doi.org/10.1002/2017GL075494, 2017.

Moore, G. W. K., Schweiger, A., Zhang, J., and Steele, M.: Spatiotemporal Variability of Sea Ice in the Arctic's Last Ice Area, Geophysical Research Letters, 46, 11 237–11 243, https://doi.org/10.1029/2019GL083722, 2019.

Nandan, V., Geldsetzer, T., Yackel, J., Mahmud, M., Scharien, R., Howell, S., King, J., Ricker, R., and Else, B.: Effect of Snow Salinity on CryoSat-2 Arctic First-Year Sea Ice Freeboard Measurements, Geophysical Research Letters, 44, 10 419–10 426, https://doi.org/10.1002/2017GL074506, 2017.

Nandan, V., Scharien, R. K., Geldsetzer, T., Kwok, R., Yackel, J. J., Mahmud, M. S., Rosel, A., Tonboe, R., Granskog, M., Willatt, R., Stroeve, J., Nomura, D., and Frey, M.: Snow Property Controls on Modeled Ku-Band Altimeter Estimates of First-Year Sea Ice Thickness: Case Studies from the Canadian and Norwegian Arctic, IEEE Journal of Selected Topics in Applied Earth Observations and Remote Sensing, 13, 1082–1096, https://doi.org/10.1109/JSTARS.2020.2966432, 2020.

NASA: IceBridge L1B Thinned Flight Lines, Version 1, [4 and 16 April 2018], Boulder, Colorado USA. NASA National Snow and Ice Data Center Distributed Active Archive Center [data set], https://doi.org/10.5067/C3HEIVPUW8FW, last access: 11 Aug 2021, 2018.

Navarro, F. and Eisen, O.: Ground-penetrating radar in glaciological applications, in: Remote Sensing of Glaciers: Techniques for Topographic, Spatial and Thematic Mapping of Glaciers, edited by Pellikka, P. and Rees, W. G., chap. 11, pp. 195–230, CRC Press, London, 1st edn., https://doi.org/10.1201/b10155, 2009.

Newman, T., Farrell, S. L., Richter-Menge, J., Connor, L. N., Kurtz, N. T., Elder, B. C., and McAdoo, D.: Assessment of radar-derived snow depth over Arctic sea ice, Journal of Geophysical Research: Oceans, 119, 8578–8602, https://doi.org/10.1002/2014JC010284, 2014.

Nicolaus, M., Hoppmann, M., Arndt, S., Hendricks, S., Katlein, C., Nicolaus, A., Rossmann, L., Schiller, M., and Schwegmann, S.: Snow Depth and Air Temperature Seasonality on Sea Ice Derived From Snow Buoy Measurements, Frontiers in Marine Science, 8, 655 446, https://doi.org/10.3389/fmars.2021.655446, 2021.

NSIDC: IceBridge Sea Ice Freeboard, Snow Depth, and Thickness Quick Look, Version 1, [data set], https://doi.org/10.5067/GRIXZ91DE0L9, 2016.

Onstott, R. G. and Shuchman, R. A.: SAR Measurements of Sea Ice, in: Synthetic Aperture Radar Marine User's Manual, edited by Jackson, C. R. and Apel, J. R., chap. 3, pp. 81–116, National Oceanic and Atmospheric Administration, Washington, D.C., URL https://www.sarusersmanual.com/ManualPDF/NOAASARManual{_}CH03{_}pg081{_}116.pdf, 2004.

Panzer, B., Gomez-Garcia, D., Leuschen, C., Paden, J., Rodriguez-Morales, F., Patel, A., Markus, T., Holt, B., and Gogineni, P.: An ultra-wideband, microwave radar for measuring snow thickness on sea ice and mapping near-surface internal layers in polar firn, Journal of Glaciology, 59, 244–254, https://doi.org/10.3189/2013JoG12J128, 2013.

Parkinson, C. L. and Comiso, J. C.: On the 2012 record low Arctic sea ice cover: Combined impact of preconditioning and an August storm, Geophysical Research Letters, 40, 1356–1361, https://doi.org/10.1002/grl.50349, 2013.

Perovich, D. K.: The interaction of ultraviolet light with Arctic sea ice during SHEBA, Annals of Glaciology, 44, 47–52, https://doi.org/10.3189/172756406781811330, 2006.

Perovich, D. K.: Sea ice and sunlight, in: Sea Ice, edited by Thomas, D. N., pp. 110–137, John Wiley & Sons, Ltd, Chichester, UK, third edn., https://doi.org/10.1002/9781118778371.ch4, 2017.

Perovich, D. K. and Polashenski, C.: Albedo evolution of seasonal Arctic sea ice, Geophysical Research Letters, 39, L08 501, https://doi.org/10.1029/2012GL051432, 2012.

Perovich, D. K., Light, B., Eicken, H., Jones, K. F., Runciman, K., and Nghiem, S. V.: Increasing solar heating of the Arctic Ocean and adjacent seas, 1979–2005: Attribution and role in the ice-albedo feedback, Geophysical Research Letters, 34, L19 505, https://doi.org/10.1029/2007GL031480, 2007.

Petrich, C. and Eicken, H.: Overview of sea ice growth and properties, in: Sea Ice, edited by Thomas, D. N., chap. 1, pp. 1–41, John Wiley & Sons, Ltd, Chichester, UK, third edn., https://doi.org/10.1002/9781118778371.ch1, 2017.

Petty, A. A., Webster, M., Boisvert, L., and Markus, T.: The NASA Eulerian Snow on Sea Ice Model (NESOSIM) v1.0: initial model development and analysis, Geoscientific Model Development, 11, 4577–4602, https://doi.org/10.5194/gmd-11-4577-2018, 2018.

Pfaffhuber, A. A., Lieser, J. L., and Haas, C.: Snow thickness profiling on Antarctic sea ice with GPR-Rapid and accurate measurements with the potential to upscale needles to a haystack, Geophysical Research Letters, 44, 7836–7844, https://doi.org/10.1002/2017GL074202, 2017.

Pfaffling, A., Haas, C., and Reid, J. E.: Direct helicopter EM - Sea-ice thickness inversion assessed with synthetic and field data, Geophysics, 72, F127–F137, https://doi.org/10.1190/1.2732551, 2007.

Planck, C. J., Whitlock, J., Polashenski, C., and Perovich, D.: The evolution of the seasonal ice mass balance buoy, Cold Regions Science and Technology, 165, 102 792, https://doi.org/10.1016/j.coldregions.2019.102792, 2019.

Polashenski, C., Perovich, D., Richter-Menge, J., and Elder, B.: Seasonal ice mass-balance buoys: adapting tools to the changing Arctic, Annals of Glaciology, 52, 18–26, https://doi.org/10.3189/172756411795931516, 2011.

Pomerleau, P., Royer, A., Langlois, A., Cliche, P., Courtemanche, B., Madore, J.-B., Picard, G., and Lefebvre, É.: Low Cost and Compact FMCW 24 GHz Radar Applications for Snowpack and Ice Thickness Measurements, Sensors, 20, 3909, https://doi.org/10.3390/s20143909, 2020.

Pounder, E. R.: The Physics of Ice, Pergamon Press, Oxford, first edn., https://doi.org/10.1016/C2013-0-08278-3, 1965.

Proksch, M., Löwe, H., and Schneebeli, M.: Density, specific surface area, and correlation length of snow measured by high-resolution penetrometry, Journal of Geophysical Research: Earth Surface, 120, 346–362, https://doi.org/10.1002/2014JF003266, 2015.

Pustogvar, A. and Kulyakhtin, A.: Sea ice density measurements. Methods and uncertainties, Cold Regions Science and Technology, 131, 46–52, https://doi.org/10.1016/j.coldregions.2016.09.001, 2016.

Quartly, G. D., Rinne, E., Passaro, M., Andersen, O. B., Dinardo, S., Fleury, S., Guillot, A., Hendricks, S., Kurekin, A. A., Müller, F. L., Ricker, R., Skourup, H., and Tsamados, M.: Retrieving Sea Level and Freeboard in the Arctic: A Review of Current Radar Altimetry Methodologies and Future Perspectives, Remote Sensing, 11, 881, https://doi.org/10.3390/rs11070881, 2019.

Rabenstein, L., Hendricks, S., Martin, T., Pfaffhuber, A., and Haas, C.: Thickness and surface-properties of different sea-ice regimes within the Arctic Trans Polar Drift: Data from summers 2001, 2004 and 2007, Journal of Geophysical Research, 115, C12 059, https://doi.org/10.1029/2009JC005846, 2010.

Rampal, P., Weiss, J., and Marsan, D.: Positive trend in the mean speed and deformation rate of Arctic sea ice, 1979–2007, Journal of Geophysical Research, 114, C05 013, https://doi.org/10.1029/2008JC005066, 2009.

Raney, R.: The Delay/Doppler Radar Altimeter, IEEE Transactions on Geoscience and Remote Sensing, 36, 1578–1588, https://doi.org/10.1109/36.718861, 1998.

Richter-Menge, J. A., Perovich, D. K., Elder, B. C., Claffey, K., Rigor, I., and Ortmeyer, M.: Ice mass-balance buoys: a tool for measuring and attributing changes in the thickness of the Arctic sea-ice cover, Annals of Glaciology, 44, 205–210, https://doi.org/10.3189/172756406781811727, 2006.

Ricker, R., Hendricks, S., Helm, V., Skourup, H., and Davidson, M.: Sensitivity of CryoSat-2 Arctic sea-ice freeboard and thickness on radar-waveform interpretation, The Cryosphere, 8, 1607–1622, https://doi.org/10.5194/tc-8-1607-2014, 2014.

Ricker, R., Hendricks, S., Perovich, D. K., Helm, V., and Gerdes, R.: Impact of snow accumulation on CryoSat-2 range retrievals over Arctic sea ice: An observational approach with buoy data, Geophysical Research Letters, 42, 4447–4455, https://doi.org/10.1002/2015GL064081, 2015.

Ricker, R., Hendricks, S., and Beckers, J. F.: The Impact of Geophysical Corrections on Sea-Ice Freeboard Retrieved from Satellite Altimetry, Remote Sensing, 8, 317, https://doi.org/10.3390/rs8040317, 2016.

Ringeisen, D.: The Arctic Stripes, last access: 13 May 2021, URL https://arctrain.de/arctic-stripes/, 2021.

Rösel, A., Itkin, P., King, J., Divine, D., Wang, C., Granskog, M. A., Krumpen, T., and Gerland, S.: Thin Sea Ice, Thick Snow, and Widespread Negative Freeboard Observed During N-ICE2015 North of Svalbard, Journal of Geophysical Research: Oceans, 123, 1156–1176, https://doi.org/10.1002/2017JC012865, 2018.

Rostosky, P., Spreen, G., Farrell, S. L., Frost, T., Heygster, G., and Melsheimer, C.: Snow Depth Retrieval on Arctic Sea Ice From Passive Microwave Radiometers—Improvements and Extensions to Multiyear Ice Using Lower Frequencies, Journal of Geophysical Research: Oceans, 123, 7120–7138, https://doi.org/10.1029/2018JC014028, 2018.

Sallila, H., Farrell, S. L., McCurry, J., and Rinne, E.: Assessment of contemporary satellite sea ice thickness products for Arctic sea ice, The Cryosphere, 13, 1187–1213, https://doi.org/10.5194/tc-13-1187-2019, 2019.

Scharroo, R., Bonekamp, H., Ponsard, C., Parisot, F., von Engeln, A., Tahtadjiev, M., de Vriendt, K., and Montagner, F.: Jason continuity of services: continuing the Jason altimeter data records as Copernicus Sentinel-6, Ocean Science, 12, 471–479, https://doi.org/10.5194/os-12-471-2016, 2016.

Schneebeli, M., Pielmeier, C., and Johnson, J. B.: Measuring snow microstructure and hardness using a high resolution penetrometer, Cold Regions Science and Technology, 30, 101–114, https://doi.org/10.1016/S0165-232X(99)00030-0, 1999.

Shalina, E. V. and Sandven, S.: Snow depth on Arctic sea ice from historical in situ data, The Cryosphere, 12, 1867–1886, https://doi.org/10.5194/tc-12-1867-2018, 2018.

Shokr, M. and Sinha, N.: Sea Ice: Physics and Remote Sensing, Geophysical Monograph Series, John Wiley & Sons, Inc, Hoboken, NJ, https://doi.org/10.1002/9781119028000, 2015.

SIMIP Community: Arctic Sea Ice in CMIP6, Geophysical Research Letters, 47, e2019GL086 749, https://doi.org/10.1029/2019GL086749, 2020.

Spreen, G., Kaleschke, L., and Heygster, G.: Sea ice remote sensing using AMSR-E 89-GHz channels, Journal of Geophysical Research, 113, C02S03, https://doi.org/10.1029/2005JC003384, 2008.

Spreen, G., Kwok, R., and Menemenlis, D.: Trends in Arctic sea ice drift and role of wind forcing: 1992-2009, Geophysical Research Letters, 38, L19 501, https://doi.org/10.1029/2011GL048970, 2011.

Stroeve, J. and Notz, D.: Changing state of Arctic sea ice across all seasons, Environmental Research Letters, 13, 103 001, https://doi.org/10.1088/1748-9326/aade56, 2018.

Stroeve, J., Nandan, V., Willatt, R., Tonboe, R., Hendricks, S., Ricker, R., Mead, J., Mallett, R., Huntemann, M., Itkin, P., Schneebeli, M., Krampe, D., Spreen, G., Wilkinson, J., Matero, I., Hoppmann, M., and Tsamados, M.: Surface-based Ku- and Ka-band polarimetric radar for sea ice studies, The Cryosphere, 14, 4405–4426, https://doi.org/10.5194/tc-14-4405-2020, 2020.

Studinger, M., Young, D., and Larsen, C.: IceBridge Mission Flight Reports, Version 1, [4 and 16 April 2018], Boulder, Colorado USA. NASA National Snow and Ice Data Center Distributed Active Archive Center [data set], https://doi.org/10.5067/3WISVI2F8EGF, last access: 19 Aug 2021, 2011.

Sturm, M.: Thermal conductivity and heat transfer through the snow on the ice of the Beaufort Sea, Journal of Geophysical Research, 107, 8043, https://doi.org/10.1029/2000JC000409, 2002.

Sturm, M. and Holmgren, J.: An Automatic Snow Depth Probe for Field Validation Campaigns, Water Resources Research, 54, 9695–9701, https://doi.org/10.1029/2018WR023559, 2018.

Sturm, M. and Massom, R. A.: Snow in the sea ice system: friend or foe?, in: Sea Ice, edited by Thomas, D. N., chap. 3, pp. 65–109, John Wiley & Sons, Ltd, Chichester, UK, third edn., https://doi.org/10.1002/9781118778371.ch3, 2017.

Sturm, M., Holmgren, J., König, M., and Morris, K.: The thermal conductivity of seasonal snow, Journal of Glaciology, 43, 26–41, https://doi.org/10.3189/S0022143000002781, 1997.

Tedesco, M., Derksen, C., Deems, J. S., and Foster, J. L.: Remote sensing of snow depth and snow water equivalent, in: Remote Sensing of the Cryosphere, edited by Tedesco, M., chap. 5, pp. 73–98, John Wiley & Sons, Ltd, Chichester, UK, https://doi.org/10.1002/9781118368909.ch5, 2015.

Timco, G. W. and Frederking, R. M.: A review of sea ice density, Cold Regions Science and Technology, 24, 1–6, https://doi.org/10.1016/0165-232X(95)00007-X, 1996.

Timco, G. W. and Weeks, W. F.: A review of the engineering properties of sea ice, https://doi.org/10.1016/j.coldregions.2009.10.003, 2010.

Tschudi, M., Meier, W. N., Stewart, J. S., Fowler, C., and Maslanik, J.: Polar Pathfinder Daily 25 km EASE-Grid Sea Ice Motion Vectors, Version 4, [2 and 10 April 2019], Boulder, Colorado USA, NASA National Snow and Ice Data Center Distributed Active Archive Center [data set], https://doi.org/10.5067/INAWUWO7QH7B, 2019a.

Tschudi, M., Meier, W. N., Stewart, J. S., Fowler, C., and Maslanik, J.: EASE-Grid Sea Ice Age, Version 4, [2–8 April 2017 and 2019], Boulder, Colorado USA, NASA National Snow and Ice Data Center Distributed Active Archive Center [data set], https://doi.org/10.5067/UTAV7490FEPB, 2019b.

Ulaby, F. T. and Long, D. G.: Microwave Radar and Radiometric Remote Sensing, University of Michigan Press, Ann Arbor, 2014.

Ulaby, F. T., Moore, R. K., and Fung, A. K.: Microwave Remote Sensing: Active and Passive Volume 2: Radar Remote Sensing and Surface Scattering and Emission Theory, Remote sensing, Artech House, Norwood, Mass., 1982.

Ulaby, F. T., Moore, R. K., and Fung, A. K.: Microwave Remote Sensing: Active and Passive Volume 3: From Theory to Applications, Remote sensing, Artech House, Norwood, Mass., 1986.

Wadhams, P., Tucker, W. B., Krabill, W. B., Swift, R. N., Comiso, J. C., and Davis, N. R.: Relationship between sea ice freeboard and draft in the Arctic Basin, and implications for ice thickness monitoring, Journal of Geophysical Research, 97, 20 325–20 334, https://doi.org/10.1029/92JC02014, 1992.

Warren, S. G., Rigor, I. G., Untersteiner, N., Radionov, V. F., Bryazgin, N. N., Aleksandrov, Y. I., and Colony, R.: Snow Depth on Arctic Sea Ice, Journal of Climate, 12, 1814–1829, https://doi.org/10.1175/1520-0442(1999)012<1814:SDOASI>2.0.CO;2, 1999.

Webster, M., Gerland, S., Holland, M., Hunke, E., Kwok, R., Lecomte, O., Massom, R., Perovich, D., and Sturm, M.: Snow in the changing sea-ice systems, Nature Climate Change, 8, 946–953, https://doi.org/10.1038/s41558-018-0286-7, 2018.

Webster, M. A., Rigor, I. G., Nghiem, S. V., Kurtz, N. T., Farrell, S. L., Perovich, D. K., and Sturm, M.: Interdecadal changes in snow depth on Arctic sea ice, Journal of Geophysical Research: Oceans, 119, 5395–5406, https://doi.org/10.1002/2014JC009985, 2014.

Wendisch, M., Brückner, M., Burrows, J., Crewell, S., Dethloff, K., Ebell, K., Lüpkes, C., Macke, A., Notholt, J., Quaas, J., Rinke, A., and Tegen, I.: Understanding Causes and Effects of Rapid Warming in the Arctic, Eos, 98, 22–26, https://doi.org/10.1029/2017EO064803, 2017.

Willatt, R., Giles, K., Laxon, S., Stone-Drake, L., and Worby, A.: Field Investigations of Ku-Band Radar Penetration Into Snow Cover on Antarctic Sea Ice, IEEE Transactions on Geoscience and Remote Sensing, 48, 365–372, https://doi.org/10.1109/TGRS.2009.2028237, 2010.

Willatt, R., Laxon, S., Giles, K., Cullen, R., Haas, C., and Helm, V.: Ku-band radar penetration into snow cover on Arctic sea ice using airborne data, Annals of Glaciology, 52, 197–205, https://doi.org/10.3189/172756411795931589, 2011.

Wingham, D., Francis, C., Baker, S., Bouzinac, C., Brockley, D., Cullen, R., de Chateau-Thierry, P., Laxon, S., Mallow, U., Mavrocordatos, C., Phalippou, L., Ratier, G., Rey, L., Rostan, F., Viau, P., and Wallis, D.: CryoSat: A mission to determine the fluctuations in Earth's land and marine ice fields, Advances in Space Research, 37, 841–871, https://doi.org/10.1016/j.asr.2005.07.027, 2006.

Yan, J.-B., Gogineni, S., Rodriguez-Morales, F., Gomez-Garcia, D., Paden, J., Li, J., Leuschen, C. J., Braaten, D. A., Richter-Menge, J. A., Farrell, S. L., Brozena, J., and Hale, R. D.: Airborne Measurements of Snow Thickness: Using ultrawide-band frequency-modulated-continuous-wave radars, IEEE Geoscience and Remote Sensing Magazine, 5, 57–76, https://doi.org/10.1109/MGRS.2017.2663325, 2017a.

Yan, J.-B., Gomez-Garcia Alvestegui, D., McDaniel, J. W., Li, Y., Gogineni, S., Rodriguez-Morales, F., Brozena, J., and Leuschen, C. J.: Ultrawideband FMCW Radar for Airborne Measurements of Snow Over Sea Ice and Land, IEEE Transactions on Geoscience and Remote Sensing, 55, 834–843, https://doi.org/10.1109/TGRS.2016.2616134, 2017b.

Ye, Y., Heygster, G., and Shokr, M.: Improving Multiyear Ice Concentration Estimates with Reanalysis Air Temperatures, IEEE Transactions on Geoscience and Remote Sensing, 54, 2602–2614, https://doi.org/10.1109/TGRS.2015.2503884, 2016a.

Ye, Y., Shokr, M., Heygster, G., and Spreen, G.: Improving Multiyear Sea Ice Concentration Estimates with Sea Ice Drift, Remote Sensing, 8, 397, https://doi.org/10.3390/rs8050397, 2016b.

Zhou, L., Stroeve, J., Xu, S., Petty, A., Tilling, R., Winstrup, M., Rostosky, P., Lawrence, I. R., Liston, G. E., Ridout, A., Tsamados, M., and Nandan, V.: Inter-comparison of snow depth over Arctic sea ice from reanalysis reconstructions and satellite retrieval, The Cryosphere, 15, 345–367, https://doi.org/10.5194/tc-15-345-2021, 2021.

Zygmuntowska, M., Rampal, P., Ivanova, N., and Smedsrud, L. H.: Uncertainties in Arctic sea ice thickness and volume: new estimates and implications for trends, The Cryosphere, 8, 705–720, https://doi.org/10.5194/tc-8-705-2014, 2014.

Declaration — Erklärung

I herewith declare, that I

1. have formulated the thesis myself and without the help of others,
2. have not used sources and tools other than those indicated nor aids other than those permissible,
3. have marked the literal or textual taken part of the used works.

I hereby declare that I have not qualified or applied for a doctorate procedure in the past.

I agree to the reviewing of the doctoral thesis with qualified software during the investigation of the pretence of plagiarism.

Hiermit versichere ich, dass ich

1. die Arbeit ohne unerlaubte fremde Hilfe angefertigt habe,
2. keine anderen als die von mir angegebenen Quellen und Hilfsmittel benutzt habe,
3. die, den benutzten Werken wörtlich oder inhaltlich entnommenen Stellen als solche kenntlich gemacht habe.

Hiermit versichere ich, dass ich mich bisher keinem Promotionsverfahren unterzogen bzw. ein solches beantragt habe.

Ich bin damit einverstanden, dass eine Überprüfung der Dissertation mit qualifizierter Software im Rahmen der Untersuchung von Plagiatsvorwürfen gestattet ist.

Bremerhaven, 21 September 2021 Arttu Jutila